SOLUTION-PROCESSABLE SOLAR CELL TECHNOLOGIES

A Dissertation

Presented to the Faculty of the Graduate School

of Cornell University

In Partial Fulfillment of the Requirements for the Degree of

Doctor of Philosophy

by

Yeefun Lim

May 2011

SOLUTION-PROCESSABLE SOLAR CELL TECHNOLOGIES

Yeefun Lim, Ph. D.

Cornell University 2011

The high cost of production of solar panels has prevented the widespread adoption of solar energy. A possible solution is to pursue solution-based solar cell technologies, since they can enable a low-cost and high-throughput manufacturing process. Both organic semiconductors and inorganic nanocrystals have emerged as promising solution-processable materials for solar cells. In this dissertation, I present my work on the investigation of both classes of materials for solar cell applications.

Organic photovoltaics consist of donor and acceptor organic semiconductors. The mechanism of charge transfer between the donor poly(3-hexylthiophene) (P3HT) and acceptor C_{60} was studied by incorporating an inter-layer into the bilayer solar cell. Charge transfer was shown to take place in a two-step process whereby energy transfer of the photo-generated excitons in P3HT to C_{60} is followed by a backward charge transfer step to P3HT.

Novel ways to process these materials are also investigated. Solar cells from P3HT and a fullerene derivative, phenyl C_{61}-butyric acid methyl ester (PCBM) were fabricated by spray-deposition. Good power conversion efficiencies above 2 % were demonstrated, indicating the viability of spray deposition as a fabrication method. In a separate effort, a novel fluorinated resorcinarene photoresist was used to photo-lithographically pattern solar cells based on a blend of P3HT and PCBM for high-voltage applications. A 15 mm array of 300 solar cells connected in series achieved an open circuit voltage (V_{OC}) of 90 volts.

Three new classes of materials for organic solar cell acceptors are presented, namely pentacenes, hexacenes, and anthradithiophenes. Solar cells based on P3HT and pentacenes gave efficiencies as high as 1.2 %. The hexacenes have the lowest band-gap, enabling hexacene-based solar cells to have photocurrent response up to 800 nm. The anthradithiophene-based solar cells achieved the highest V_{OC} approaching 1.1 Volts, and decent efficiencies of around 0.8 %.

Finally, a facile alcothermal method for the synthesis of dispersible CuO and Cu_2O nanocrystals is presented. A bilayer CuO / PCBM solar cell demonstrated an efficiency of 0.04 %, indicating the potential of these materials for light harvesting applications.

BIOGRAPHICAL SKETCH

Yee-Fun Lim was born in Singapore, Singapore in 1980. As a child, he has been fascinated with the cosmos, nature, and figuring out how things work. This interest led him to study Physics as an undergraduate at the California Institute of Technology, where he received his B. S. in 2003. He then returned to Singapore to serve 2 years in the military, before joining Singapore's Agency for Science, Technology and Research (A*STAR) as a junior researcher. During this time, he became deeply interested in clean energy research, thus he decided to take up an A*STAR fellowship to pursue a Ph. D. at Cornell University. He entered the Applied Physics program at Cornell in 2006. Under the supervision of Prof. George Malliaras and Prof. Tobias Hanrath, he worked on organic as well as nanocrystal solar cell technologies with the goal of achieving low-cost photovoltaics. Upon graduation in 2011, Yee-Fun will return to Singapore and continue his research in solar energy at A*STAR.

Dedicated to my father, Lim Kian Hong,

my mother, Chua Soh Kiau,

and my sister, Lim Yee Siang.

ACKNOWLEDGMENTS

First and foremost, I would like to thank my family for their emotional support, giving me strength to keep on persevering whenever the going gets tough. I acknowledge financial support from A*STAR, Singapore, and I am grateful to my scholarship officer Rinawati Rahmat for her assistance with administrative matters. Thanks are due to my undergraduate professors, Axel Scherer, Dimitry Psaltis, and Kip Thorne, who inspired me to pursue my graduate degree. My research work would not have been possible without the kind assistance of the tool managers at the Cornell NanoScale Science & Technology Facility (CNF), Cornell Center for Materials Research (CCMR), and the KAUST-Cornell Center for Energy and Sustainability (KAUST-CU). I am particularly indebted to Maura Weathers, John Hunt, John Grazul, Christopher Umbach, Garry Bordonaro, Rob Ilic, Dan Woodie, Jerry Drumheller, and David Jung. John Anthony at the University of Kentucky, together with his dedicated team of chemists Ying Shu, Zhong Li, and Balaji Purushothaman, synthesized the wide range of organic small molecules studied in this work. I am grateful for the assistance of various Cornell undergraduates, Sung Soo Lee, Daniel Riffe and Jo Eun Kim, who helped to fabricate and test countless solar cell devices. I am very fortunate to have enjoyed much fruitful collaboration with my talented colleagues at Cornell, Matthew Lloyd, Jason Slinker, Daniel Bernards, John DeFranco, Chung-Han Wu, Vladimir Pozdin, Alexander Zakhidov, Hon Hang Fong, Jin-Kyun Lee, Christopher Ober, Joshua Choi, William Baumgardner, Kwan Wee Tan and Yeon Sook Chung. My committee members, Frank Wise, Jack Blakely, and especially Tobias Hanrath have given me much valuable guidance and advice. Finally, I owe much to George Malliaras for his unwavering support and belief in me, and for giving me such an invaluable graduate school learning experience.

TABLE OF CONTENTS

LIST OF FIGURES

LIST OF TABLES

LIST OF ABBREVIATIONS

ADT	anthradithiophene
ADTA	amide-functionalized anthradithiophene
AFM	atomic force microscopy
CuPc	copper(II) phthalocyanine
DCB	1,2-dichlorobenzene
diF-TESADT	2,8-difluoro-5,11-bis(triethylsilylethynyl) anthradithiophene
DMSO	dimethylsulfoxide
EDT	1,2-ethanedithiol
ethyl-TES-ADT	2,8-diethyl-5,11-bis(triethylsilylethynyl) anthradithiophene
EQE	external quantum efficiency
F4-TCHS-Hn	tetrafluoro-7,14-tricyclohexylsilylethynyl-hexacene
F4-TCPS-Hn	tetrafluoro-7,14-tricyclopentylsilylethynyl-hexacene
F8BT	poly(9,9-dioctylfluorene-*alt*-benzothiadiazole)
Fc/Fc^+	ferrocene/ferrocenium
HOMO	highest occupied molecular orbital
ITO	indium tin oxide
J	current density
J_{MAX}	current density at maximum power point
J_{SC}	short-circuit current density
LBL	layer-by-layer
LUMO	lowest unoccupied molecular orbital
MEH-PPV	poly[2-methoxy-5-(2'-ethyl-hexyloxy)-1,4-phenylene vinylene]

MEMS	microelectromechanical systems
MDMO-PPV	poly[2-methoxy-5-(3’,7’-dimethyloctyloxy)-1,4-phenylenevinylene]
NC	nanocrystal
OLED	organic light-emitting diode
OPV	organic photovoltaic
OSC	organic solar cell
OTFT	organic thin film transistor
P3HT	poly(3-hexylthiophene)
P3OT	poly(3-octylthiophene)
PCE	power conversion efficiency
PCBM	phenyl C_{61}-butyric acid methyl ester
$PC_{71}BM$	phenyl C_{71}-butyric acid methyl ester
PCPDTBT	poly[2,6-(4,4-bis-(2-ethylhexyl)-4*H*-cyclopenta[2,1-b;3,4-b’]dithiophene)-*alt*-4,7-(2,1,3-benzothiadiazole)]
PDTPQx	poly(2,3-didecyl-quinoxaline-5,8-diyl-*alt*-*N*-octyldithieno[3,2-*b:*2′,3′-*d*]pyrrole)
PEDOT:PSS	poly(3,4-ethylenedioxythiophene)-poly(styrenesulfonate)
PGMEA	propylene glycol methyl ether acetate
P_{INC}	power intensity of incident radiation
P_{MAX}	maximum power output
$[Ru(bpy)_3]^{2+}(PF_6^-)_2$	tris-(2,2’-bipyridyl)ruthenium (II) hexafluorophosphate
TCHS	tri-cyclohexylsilyl
TCPS	tri-cyclopentylsilyl
TIBS	tri-isobutylsilyl
TIPS	tri-isopropylsilyl

TNPS	tri-n-propylsilyl
TPD	N,N′-bis (3-methylphenyl)-N,N′-bis(phenyl)-benzidine
V	voltage
V_{MAX}	voltage at maximum power point
V_{OC}	open-circuit voltage

CHAPTER 1

INTRODUCTION AND BACKGROUND

The energy landscape

Due to world population and economic growth, the global energy consumption is projected to increase from 13.5 TW in 2001 to 27.6 TW in 2050 and then to 43.0 TW in 2100.[1] In the "business as usual" scenario, with no changes to the way we utilize energy, CO_2 emissions are projected to rise by over 20 % in the year 2020 with respect to 2004 levels.[2] This is an extremely undesirable situation, for rising CO_2 emissions have been linked to global warming and climate change.[3] Urgent measures therefore need to be taken in order to reduce emissions. In an "advanced scenario", in which non-polluting renewable energy sources are used to supply a large fraction of our energy needs, CO_2 emissions in 2020 can be reduced by as much as 30 %.[2] Clearly, renewable energy should be aggressively pursued in order to prevent the worst effects of climate change.

Among the various sources of renewable energy, solar energy has by far the greatest resource base, for more energy from sunlight strikes the earth in 1 hour (4.3×10^{20} J) than all the energy consumed on the planet in 1 year (4.1×10^{20} J).[1] However, the high costs of electricity generated from current solar cell technologies, which are several times that of electricity produced from coal,[4] have prevented the widespread adoption of solar energy. Extrapolated using standard technology learning curves, it may take 10 years or longer for solar energy to be cost competitive with coal-produced electricity,[5] although new "disruptive" technologies may be able to significantly reduce the timeline.[5]

A roll-to-roll manufacturing process based on solution-processable solar cell materials can be such a disruptive technology.[6] Solution processing allows the deposition of materials by methods such as screen printing,[7] inkjet printing,[8] and spraying,[9, 10] which are not only cheap but also high-throughput processes.[6] The last point is particularly important since solar radiation is rather diffuse, and a very large area of solar panels will be needed to satisfy the world's demand for electricity.[4] For instance, a land area about the size of the state of Arkansas is needed for solar panels to provide the United States with all its electricity needs.[4] A high-throughput manufacturing process is therefore crucial in order to supply the large areas of solar panels that are required in a realistic time frame.

With regards to the available solution-processable solar cell technologies, organic photovoltaics based on soluble semiconducting polymers and small molecules are already a fairly mature technology,[6] and companies such as Konarka have been established with the goal of commercialization.[6] Solar cells based on colloidal inorganic nanocrystals are also starting to attract attention, and progress in this area has been rapid in recent years.[11] In this dissertation, I will investigate both organic semiconductors and inorganic nanocrystals as materials for solution-processable solar cell technologies, with the goal of enabling a low-cost and high-throughput manufacturing process.

To facilitate the discussion that will follow, standard solar cell terminologies will first be defined. This will be followed by a review of the progress in organic and nanocrystal solar cell technologies. Finally, an outline of the dissertation will be presented.

Solar cell terminologies

Figure 1.1 shows the current-density (J) vs. voltage (V) curves for a solar cell tested in the dark as well as in the light. In this case, "light" refers to 100 mW/cm^2 radiation from a solar simulator designed to approximate the air mass 1.5 (AM 1.5) solar spectrum as closely as possible. AM 1.5 refers to the solar radiation that has passed through 1.5 times of the Earth's atmospheric mass. The various solar cell figures of merit, some of which are illustrated in the figure, are defined as follows:

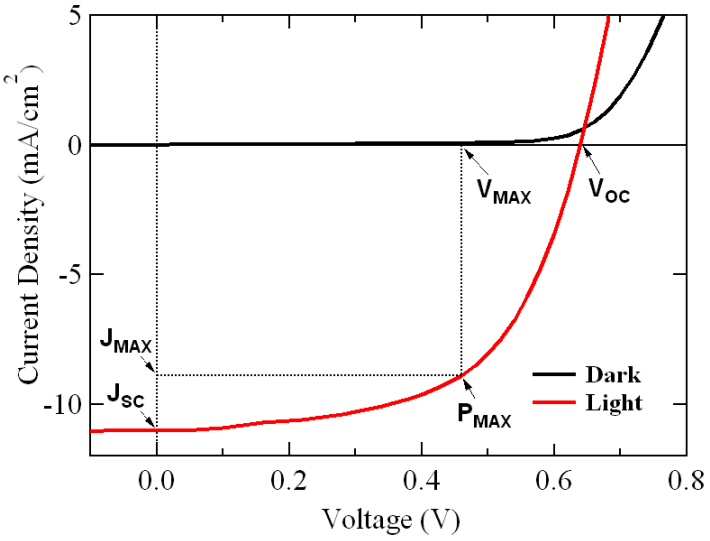

Figure 1.1 Solar cell J-V curves.

V_{OC}, the open-circuit voltage, is the voltage at which the solar cell current is zero (hence open-circuit).

J_{SC}, the short-circuit current density, is the current density at which the solar cell voltage is zero (hence short-circuit).

P_{MAX} is the maximum power output (current density multiplied by voltage) of the solar cell. **V_{MAX}** and **J_{MAX}** are the voltage and current density corresponding to this point of maximum power on the J-V curve.

FF, the fill factor, is a measure of the shape of the J-V curve, and is defined as

follows:

$$FF = \frac{V_{MAX} \times J_{MAX}}{V_{OC} \times J_{SC}} \quad \text{(Equation 1.1)}$$

If $\mathbf{P_{INC}}$ is the power intensity of the incident solar radiation, then the solar cell power conversion efficiency (**PCE**) is defined as follows:

$$PCE = \frac{P_{MAX}}{P_{INC}} = \frac{V_{MAX} \times J_{MAX}}{P_{INC}} = \frac{FF \times V_{OC} \times J_{SC}}{P_{INC}} \quad \text{(Equation 1.2)}$$

Organic solar cells

The common feature of all organic semiconductors is that they possess a carbon backbone that alternate between single and double bonds, a property termed conjugation.[12] The p_z orbitals on adjacent carbon atoms can overlap to form π orbitals, which are able to delocalize across the small molecule or polymer backbone.[12] Charge transport takes place primarily through these orbitals, and good transport properties are possible if adjacent molecular π orbitals possess good overlap with each other.[12] The extent of π orbital delocalization determines the quantum confinement of the electron wave-function, hence electrons in organic semiconductors can be modeled as particles in a box.[13] It is well known in quantum mechanics that the spacing between the quantum energy levels of such particles vary inversely with the square of the length of the box,[14] hence a larger degree of delocalization ("larger" box) results in smaller band-gaps. The band-gap of an organic semiconductor may be defined as the energy difference between the highest occupied molecular orbital (HOMO) and the lowest unoccupied molecular orbital (LUMO).[12] **Figure 1.2** shows a representative gallery of organic semiconductors commonly used in photovoltaic applications.

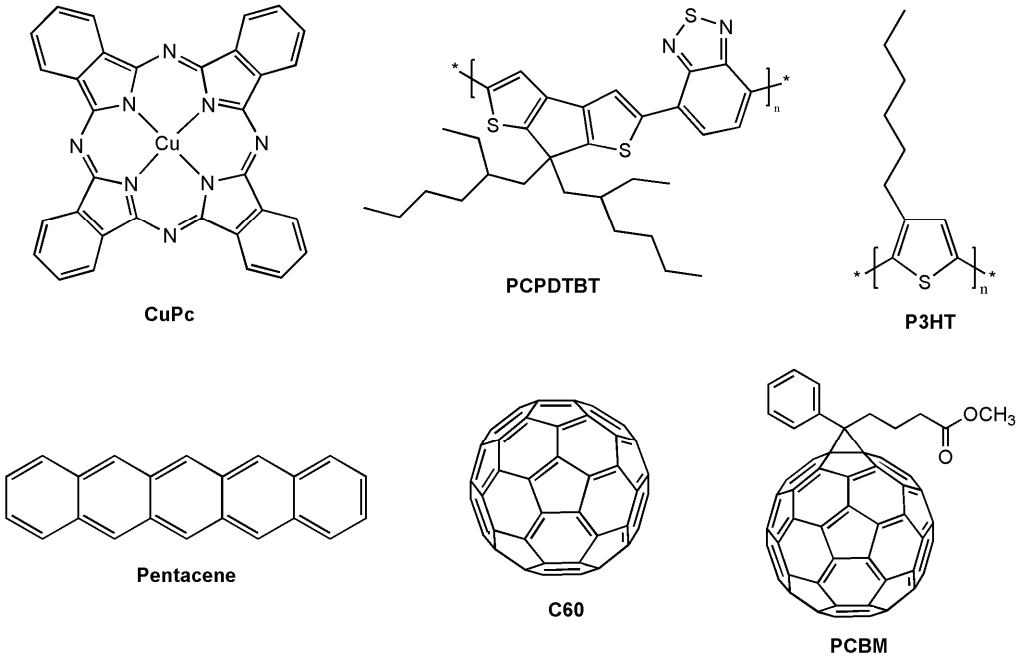

Figure 1.2 A gallery of organic semiconductors.

The first efficient solar cell fabricated from organic semiconductors was reported by Tang in 1986.[15] The active material was a bi-layer comprised of copper(II) phthalocyanine (CuPc) and a perylene tetracarboxylic derivative, and the solar cell achieved an efficiency of almost 1 % under AM 2 irradiation.[15] Although there were prior reports of organic solar cells,[16] the device architectures were mostly based on a single organic layer with the built-in potential generated from the Schottky-barrier at one of the organic-metal interfaces, and low efficiencies of 0.1 % or below were typically reported.[16]. The key to the breakthrough of the Tang cell was the incorporation of the hetero-junction between two different organic semiconductors. It was understood later that this hetero-junction needs to be a type II semiconductor junction between two dissimilar organic materials with different HOMO and LUMO energy levels.[17] Upon photo-excitation in organic semiconductors, photo-generated electron and hole pairs remain tightly bound in the form of excitons, due to low

dielectric constants (typically around 3) and the localized nature of the electronic wave functions.[12] The role of the hetero-junction, then, is to allow for the dissociation of the photo-generated excitons into free electrons and holes via the transfer of an electron from the donor to acceptor or the transfer of a hole from the acceptor to the donor.[17] This dissociation process will be further elaborated upon in chapter 2.

The success of the Tang cell inspired much subsequent work based on the bi-layer donor-acceptor organic solar cell structure.[18] C_{60} became the acceptor of choice after the 1992 discovery of ultra-fast (picosecond time-scale) electron transfer from a semi-conducting polymer to the fullerene.[19] The field has progressed rapidly since the Tang cell, and some of the most successful donor/acceptor systems in terms of power conversion efficiencies are the CuPc/C_{60} (4.2 %),[20] pentacene/C_{60} (2.7 %),[21] and squaraine/C_{60} (3.2 %)[22] solar cells. Recently, a solar cell based on a dicyanovinyl (DCV)-substituted oligothiophene as the donor and C_{60} as the acceptor achieved an efficiency of 5.2 %,[23] representing the state-of-the-art in small molecule bi-layer solar cells.

All of the above-mentioned solar cells made use of vacuum-deposited small molecules as the active layer, while a high-throughput manufacturing process should ideally be based on materials processed from solution. The breakthrough in solution-processable organic photovoltaic technology came in 1995 with the synthesis of a soluble fullerene derivative, phenyl C_{61}-butyric acid methyl ester (PCBM).[24] PCBM was blended with a donor semiconducting polymer, poly(2-methoxy-5-(2'-ethyl-hexyloxy)-1,4-phenylene vinylene) (MEH-PPV), and the mixture was spin-casted from solution to form the solar cell active layer.[25] The solar cell achieved a quantum efficiency of nearly 3 %, which was two orders of magnitude better than previous polymer cells processed from solution.[25] This solar cell also introduced another innovation, namely the organic "bulk-heterojunction". Since the donor and acceptor

phases were intimately mixed, the organic heterojunction was present everywhere in the film and not just at the bi-layer interface, thus giving rise to the term "bulk-heterojunction".

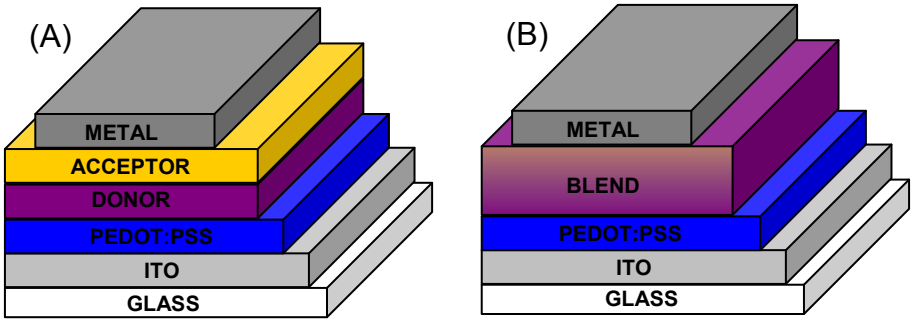

Figure 1.3 Common organic solar cell device architectures: (a) bilayer cell (b) bulk-heterojunction blend cell.

It is appropriate at this juncture to review the two most common organic solar cell device architectures: the donor/acceptor bi-layer (**Figure 1.3(a)**) and the bulk-heterojunction blend (**Figure 1.3(b)**) structures. In the bi-layer structure, the interface is in the middle of the film, and dissociated electrons and holes have well-defined pathways to the collection electrodes. For efficient exciton dissociation, the donor and acceptor layer thicknesses need to be on the order of the exciton diffusion length, typically 5-10 nm for organic semiconductors.[18] However, the films need to be about 100 nm or thicker in order to absorb most of the incident solar radiation.[17] Such conflicting requirements represent the main disadvantage of bi-layer cells. The bulk-heterojunction blend cell, on the other hand, has no such problem since the exciton dissociation interface occurs everywhere in the film, thus it can possess both the desirable properties of efficient exciton dissociation and light absorption. However, since the donor and acceptor phases are intimately mixed together, there are no well-defined charge collection pathways, hence charge collection tends to be inefficient.

Typically, the active layers are sandwich between a low work-function metal cathode (such as Al) and a transparent conductor such as indium tin oxide (ITO) as the anode. A layer of poly(3,4-ethylenedioxythiophene)-poly(styrenesulfonate) (PEDOT:PSS) is usually inserted between the ITO and the active layer. PEDOT:PSS, a transparent conducting polymer, ensures that the anode has a high and well-defined work-function of around 5.0-5.1 eV, and also serves as the hole-transport layer.[17]

Not surprisingly, morphology control is critical in bulk-heterojunction cells, since it is important to achieve the donor/acceptor domain sizes that provide the optimum compromise between exciton dissociation and charge collection. A significant advance was made in 2001, when Shaheen *et al.* demonstrated a 2.5 % efficient bulk-heterojunction cell based on poly[2-methoxy-5-(3',7'-dimethyloctyloxy)-1,4-phenylenevinylene] (MDMO-PPV) as the polymer donor and PCBM as the acceptor.[26] They found that the choice of solvent for spin-coating was critical, and films spin-casted from chlorobenzene exhibited much more intimate mixing of the donor and acceptor phases than films spin-casted from toluene. The dramatic result was an increase in efficiency from 0.9 % for the toluene-casted films to 2.5 % for the chlorobenzene-casted films.[26] This result highlighted the importance of film morphology for bulk-heterojunction cells.

Another important breakthrough came from the debut of poly(3-hexylthiophene) (P3HT) as a solar cell donor material in 2003.[27] P3HT has a lower band-gap (~ 1.9 eV) than MDMO-PPV (~ 2.2 eV)[17], and a hole charge-carrier mobility of 0.1 cm^2/Vs which was an outstanding value for semiconducting polymers at that time.[28] The remarkable discovery of Padinger *et al.* was that a brief post-fabrication thermal annealing was able to boost the efficiency of P3HT:PCBM bulk-heterojunction solar cells from 0.4 % to as high as 3.5 %.[27] It was later understood that the effect of the thermal annealing treatment was to produce a nanoscale

interpenetrating network with crystalline order for both components, thus dramatically improving charge collection in the cell.[29] Further optimization to the P3HT:PCBM system led to significant increase in the power conversion efficiency in a relatively short time-frame of 2-3 years, with several groups reporting efficiencies ranging from 4.4 % to 5.2 %.[30-33] Of particular interest was the paper by Li *et al*.,[30] in which he reported that "solvent-annealing" of P3HT:PCBM films can achieve efficiencies as good as or better than thermal annealing. Essentially, solvent annealing involved using a high boiling point solvent like 1,2-dichlorobenzene for processing, in order to facilitate slow-drying of the films in saturated solvent vapor which resulted in the evolution of favorable film morphologies.[30]

One more notable method in the toolbox for morphology control is the processing of films with alkane dithiols.[34] In the debut solar cell paper for the low band-gap polymer, poly[2,6-(4,4-bis-(2-ethylhexyl)-4*H*-cyclopenta[2,1-b;3,4-b']dithiophene)-*alt*-4,7-(2,1,3-benzothiadiazole)] (PCPDTBT), it was reported that a PCPDTBT:$PC_{71}BM$ cell achieved an efficiency of 3.2 %.[35] PCPDTBT has a solid-state band-gap of 1.5 eV,[35] which is lower than that of P3HT (1.9 eV) and hence allowing it to absorb a greater fraction of the solar radiation (see **Figure 1.4**). While 3.2 % was a decent efficiency, it was found that PCPDTBT did not respond well to thermal or solvent annealing,[35] thus the regular methods for improving P3HT morphology did not work for this polymer. Subsequently, Peet *et al.* showed that the addition of a small amount (2 volume percent) of 1,8-octanedithiol to the solution prior to spin-coating boosted the efficiency of PCPDTBT:$PC_{71}BM$ cells from 2.8 % to 5.5 %.[34] It was later found that the effect of the 1,8-octanedithiol was to allow the $PC_{71}BM$ to remain in solution for a longer time during the spin-coating process, thus facilitating the formation of a well-connected PCPDTBT network.[36] Other additives such as 1,8-diiodooctane were also found to have a similar effect, and it was

established that such additives need to have selective (differential) solubility of the fullerene component and possess higher boiling points than the host solvent.[36]

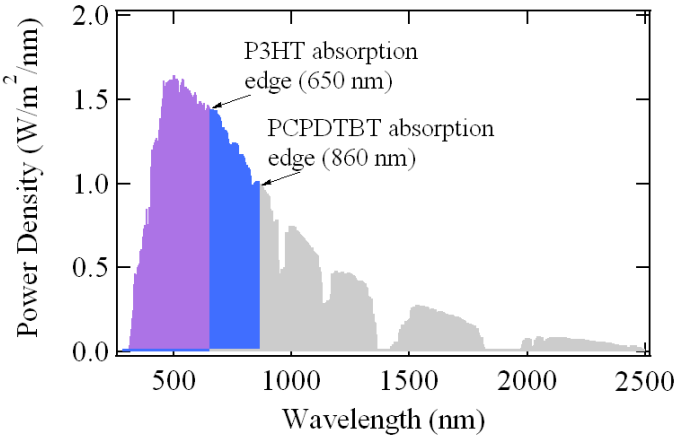

Figure 1.4 AM 1.5 solar spectrum[37] showing P3HT[30] and PCPDTBT[34] absorption.

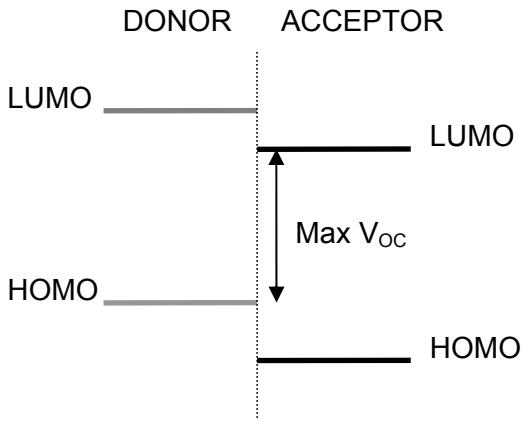

Figure 1.5 V_{OC} limit in organic solar cells.

In 2006, Scharber *et al.* published a set of important design rules for organic solar cells.[38] Through an investigation of a set of donor polymers with different HOMO/LUMO energy levels, they found that the solar cell V_{OC} followed roughly this relationship:

$$e \cdot V_{OC} = (\left|E^{Donor}\,HOMO\right| - \left|E^{Acceptor}\,LUMO\right|) - 0.3eV \qquad \text{(Equation 1.3)}$$

Thus, the V_{OC} is limited by the difference between the HOMO energy level of the donor and the LUMO energy level of the acceptor, as shown schematically in **Figure 1.5**. The "loss" of 0.3 eV was an empirical factor and had not been fully understood,[38] although it had been attributed to the binding energy of the exciton in the organic semiconductor.[39] Based on this relationship, Scharber *et al.* calculated the maximum realistically achievable efficiencies as a function of polymer band-gaps and energy levels. They found that a band-gap of around 1.5 eV is ideal, with a maximum efficiency just over 10 %.[38] Incidentally, 1.5 eV is the band-gap of PCPDTBT. From **Figure 1.4**, it is clear that PCPDTBT absorbs a significantly higher fraction of the solar spectrum than a higher band-gap polymer like P3HT, but a large part of the solar spectrum remains un-utilized. Further reduction of the band-gap will allow more of the solar spectrum to be absorbed, but this comes with a sacrifice in V_{OC} (Equation 1.3). The band-gap value of 1.5 eV thus represents the optimum compromise between light absorption and V_{OC}.

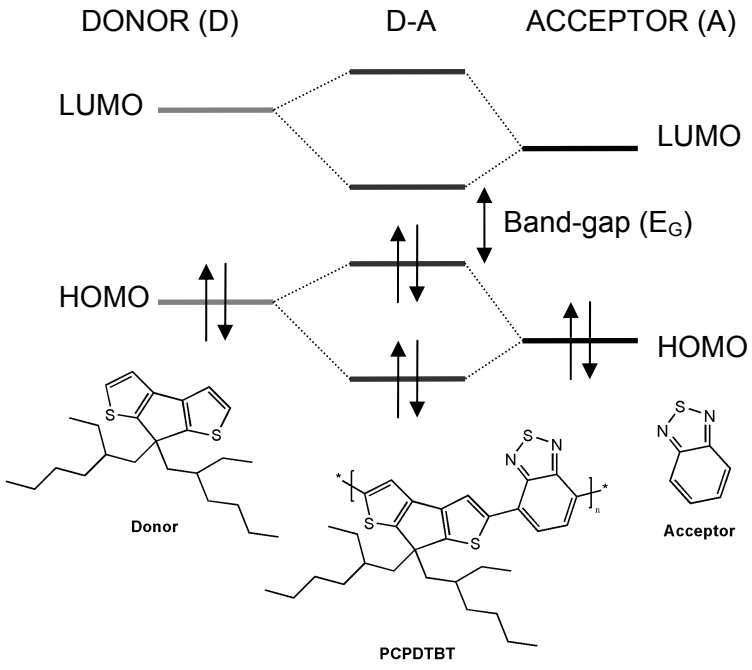

Figure 1.6 Orbital hybridization in donor-acceptor polymers.

These design rules motivated intense research efforts into low band-gap polymers with tunable energy levels. A favorite method for designing such polymers was via the donor-acceptor system, in which the polymers comprise of repeating donor-acceptor units.[40] This concept is illustrated in **Figure 1.6**, which shows that the low band-gap is a result of orbital hybridization between the LUMO and HOMO of the donor and acceptor units.[40] PCPDTBT is an example of a donor-acceptor polymer,[35] as illustrated in **Figure 1.6** for clarity. A survey of high-performance donor-acceptor polymers is shown in **Table 1.1**. Such polymers represent the state-of-the-art in organic solar cell efficiencies, with reported PCEs as high as 7.4 %.[41]

Table 1.1 A survey of high-performance donor-acceptor polymers

Polymer	Acceptor	E_G [eV]	V_{OC} [V]	J_{SC} [mA/cm^2]	FF	PCE [%]	Ref
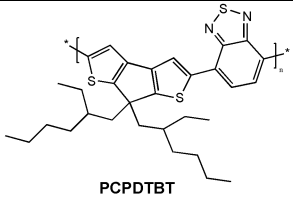 PCPDTBT	$PC_{71}BM$	1.5	0.62	16.2	0.55	5.5	[36]
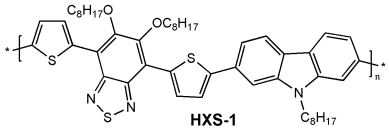 HXS-1	$PC_{71}BM$	1.9	0.81	9.6	0.69	5.4	[42]
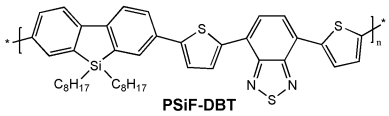 PSiF-DBT	PCBM	1.8	0.90	9.5	0.51	5.4	[43]
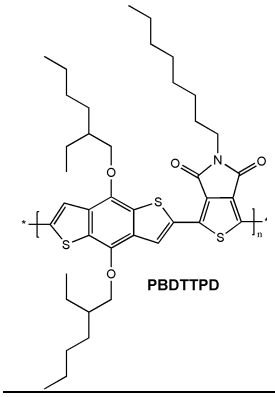 PBDTTPD	$PC_{71}BM$	1.8	0.85	9.8	0.66	5.5	[44]

Table 1.1 (Continued)

Polymer	Acceptor	E_G [eV]	V_{OC} [V]	J_{SC} [mA/cm^2]	FF	PCE [%]	Ref
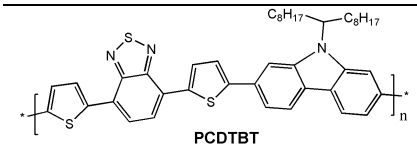 PCDTBT	$PC_{71}BM$	1.9	0.88	10.6	0.66	6.1	[45]
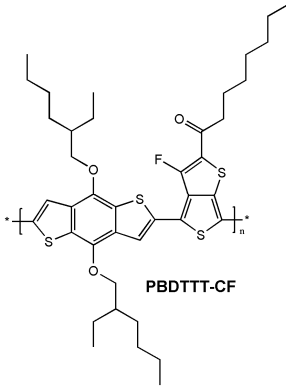 PBDTTT-CF	PCBM	1.8	0.76	13.4	0.66	6.8	[46]
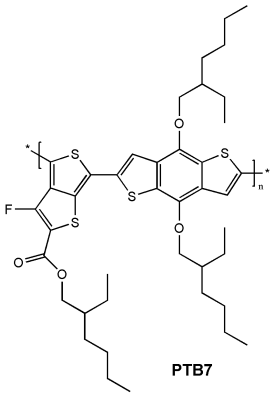 PTB7	$PC_{71}BM$	1.6	0.74	14.5	0.69	7.4	[41]

Finally, it is worthwhile to mention that while single-layer organic solar cells are projected to have a maximum achievable efficiency of just over 11 %, tandem cells can have PCEs as high as 14 %.[47] The structure of a tandem cell is illustrated in **Figure 1.7**, which is essentially a front and back cell stacked on top of each other, with an inter-layer in between that serves as a recombination layer. The front and back cells are usually made from polymers with different band-gaps so that they absorb different portions of the solar spectrum (for instance, P3HT and PCPDTBT as shown

in **Figure 1.4**). In principle, the V_{OC} of the tandem cell should be the addition of that of the front and back cells.[48] Such a structure is able to have a response over a greater portion of the solar spectrum (the addition of both polymers' absorption spectrum) and still maintain a high V_{OC}, thus it can overcome the limitations of a single-layer cell. Important design criteria for a tandem cell include an efficient recombination inter-layer as well as current matching between the front and back cells.[48] A tandem cell consisting of PCPDTBT:PCBM as the front cell, P3HT:$PC_{71}BM$ as the back cell, and an inter-layer of TiO_x and PEDOT:PSS achieved a power conversion efficiency of 6.5 %.[48] In another notable work, a tandem cell was constructed with P3HT:$PC_{71}BM$ as the front cell, a blend of the low band-gap (1.5 eV) polymer poly[4,4'-bis(2-ethylhexyl)dithieno[3,2-*b*:2',3'-d]silole]-2,6-diyl-*alt*-(2,1,3-benzothiadiazole)-4,7-diyl] (PSBTBT) and $PC_{71}BM$ as the back cell, and TiO_2/Al/PEDOT:PSS as the inter-layer gave an efficiency of 5.8 %.[49] Further optimization of tandem cells, perhaps with the incorporation of some of the champion polymers shown in **Table 1.1**, is expected to be the best approach for achieving organic solar cells that are above 10 % in efficiency,[47] a performance benchmark considered important for viable commercialization and large-scale solar cell manufacturing.[6]

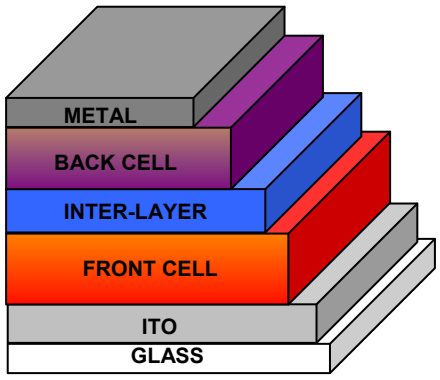

Figure 1.7 Tandem solar cell structure.

Inorganic nanocrystal solar cells

The field of nanocrystal (NC) science took off with the pioneering work of Louis Brus and his co-workers.[50-52] In 1983, his group was the first to investigate quantum size effects in an inorganic (CdS) NC,[50] while in the following year Brus presented a model for NC electron-electron and electron-hole interactions.[51] In 1988, Brus, Steigerwald and co-workers presented a synthesis of CdSe NCs via arrested precipitation in inverse micellar solution.[52] They further demonstrated that molecular modification of the NC surface enables isolation of the product with a variety of organic surface ligands that also enabled the solubility of the NCs in organic solvents,[52] which was of great importance for the size-stability and solution processing of these NCs.[52] In 1993, Murray, Norris and Bawendi pioneered the "hot-injection" NC synthesis method, which was based on the pyrolysis of organometallic reagents by injection into a hot coordinating solvent.[53] In such a process, the reaction mixture becomes highly supersaturated instantaneously upon the injection of the reactive precursors, thus there is a well-defined and well-controlled nucleation step which leads to nearly monodisperse crystallites with small size-distribution.[53, 54] The high sample quality facilitated the further study and characterization of NC properties.[53] This "hot-injection" synthesis method thus became highly popular, not just for the synthesis of chalcogenide but also of metal and oxide NCs.[54]

The most interesting property of semiconductor NCs is that their band-gaps can be tuned by changing the NC size. Brus showed that as the NC diameter approaches the exciton Bohr radius, quantum confinement becomes a significant effect. This is clearly illustrated in **Table 1.2**, which shows that semiconductor band-gaps at nano-scales are much larger than the bulk band-gaps. This effect is especially dramatic in PbSe, which has one of the largest exciton Bohr radius at 460 Å.[55] The band-gap of PbSe increases from the bulk value of 0.26 eV to 1.1 eV for a 31 Å

diameter NC,[56] which is almost a 5-fold jump. The variable band-gap makes NCs very versatile as solar cell materials, since NC band-gap affects both the light absorption and V_{OC} of solar cells.[56]

Table 1.2 Quantum-size effects of common NC semiconducting materials.

Compound	Bulk E_G[57] [eV]	Bohr radius [Å]	NC E_G[a] [eV]	References
Si	1.11	49	1.68 (38 Å)	[58]
InP	1.35	150	1.9 (35 Å)	[59]
CdS	2.53	30	3.23 (39 Å)	[60, 61]
CdSe	1.74	56	2.16 (37 Å)	[60, 62]
CdTe	1.50	75	2.3 (33 Å)	[60, 63]
ZnS	3.6	22	4.5 (61 Å)	[60, 64]
PbS	0.37	200	1.0 (45 Å)	[55]
PbSe	0.26	460	1.1 (31 Å)	[55, 56]

[a] The NC band-gap is listed for a particular NC size (in brackets)

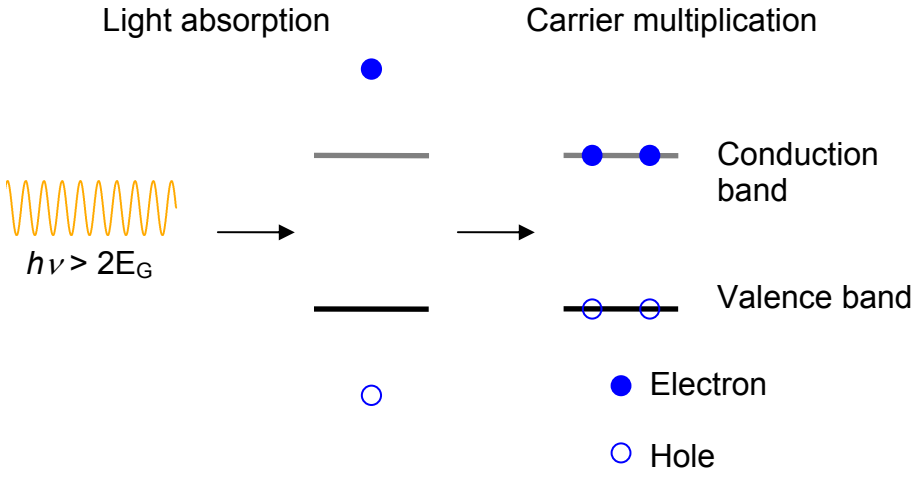

Figure 1.8 Multi-exciton generation.

An interesting development in the NC field was the discovery of multi-exciton generation (MEG) in PbSe NCs in 2004.[65] MEG is schematically illustrated in

Figure 1.8; essentially it is a process whereby the absorption of a high-energy photon (more than twice the band-gap) gives rise to two or more electron-hole pairs. Early reports show MEG occurring in several types of NCs including PbSe,[65-68] PbS,[66] CdSe,[67] and Si,[58] with reports of as many as seven excitons generated per absorbed photon for PbSe NCs at energies that are 7.8 times the band-gap.[68] It was believed that MEG will be more efficient in NC as compared to bulk semiconductors, since in the bulk crystal momentum must be conserved in addition to energy conservation thus imposing an additional constraint.[58, 66] Furthermore, the rate of electron relaxation through electron-phonon interactions should be significantly reduced due to the discrete nature of the electron-hole spectra in NCs.[66] Clearly, it would be advantageous for solar cells to exploit MEG, and it was shown using a detailed balance analysis that the maximum PCE is 42 % for a material with a carrier multiplication threshold at 2 E_G, as compared to 31 % if MEG is not present.[69] The initial optimism, however, was dampened with the publication of a report that MEG was not observed in CdSe NCs,[70] thus contradicting earlier reports.[67] Later studies of MEG carried out with more careful data analysis confirmed that MEG was present in PbSe NCs, albeit at a much lower efficiency.[71, 72] For instance, Trinh *et al.* reported a carrier multiplication of just 1.7 at a photon energy that was 4.8 times the band-gap.[71] Despite these setbacks, MEG had already been demonstrated in practical devices,[73, 74] and it may yet lead to more efficient solar cells.

The combination of several attractive NC properties, namely solution processability, band-gap tunability, potential for MEG, and availability of materials to absorb at all parts of the solar spectrum (see **Table 1.2**) led to much research interest in NC solar cells.[11] Three main device architectures for solid-state NC solar cells have emerged (see **Figure 1.9**), namely polymer/NC blend organic-inorganic hybrid cell (**Figure 1.9(a)**), NC/metal Schottky junction cell (**Figure 1.9(b)**), and

NC/acceptor bilayer cell (**Figure 1.9(c)**).[11] A survey of NC-based solar cell performance is presented in **Table 1.3**.

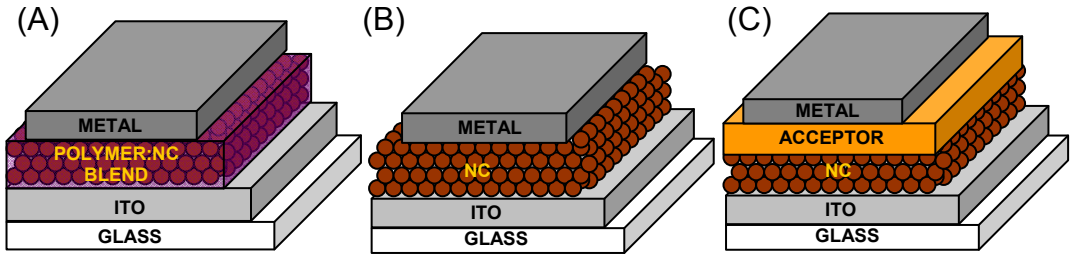

Figure 1.9 Common NC solar cell architectures: (a) polymer:NC bulk-heterojunction blend cell (b) NC/metal Schottky cell (c) NC/acceptor bilayer cell.

The polymer:NC organic-inorganic hybrid cell combines the advantages of good film forming properties of the polymer with the superior charge transport of inorganic semiconductors.[75] Typically, the polymer is the donor material while the NC is the acceptor, and exciton dissociation takes place at the polymer:NC bulk-heterojunction. Huynh *et al.* published in 2002 the first report of notable efficiency from a NC based solar cell; they reported an efficiency of 1.7 % from a cell comprising of a blend of P3HT and CdSe nanorods.[75] Nanorods were found to be better than nanoparticles since charge transport in the former was better.[75] Optimization of the P3HT component led to an efficiency of 2.6 %,[76] while the replacement of P3HT with PCPDTBT gave an efficiency of 3.2 %.[77] In a separate effort, a blend of CdTe nanorods and the polymer poly(3-octylthiophene) (P3OT) achieve a PCE of 1.06 %.[78] PbS and PbSe NCs were also utilized in hybrid cells, although their performances were somewhat inferior.[79, 80] An optimized P3HT:PbSe cell gave 0.26 %,[79] while Noone *et al.* reported an efficiency of 0.55 % from a cell based on a blend of PbS NCs and the polymer poly(2,3-didecyl-quinoxaline-5,8-diyl-*alt*-*N*-octyldithieno[3,2-*b*:2′,3′-*d*]pyrrole) (PDTPQx).[80] Noone *et al.* showed that the

poor performance of PbS and PbSe hybrid cells was due to the inefficient exciton dissociation from most polymers to these NCs.[80] They found a polymer PDTPQx that demonstrated superior exciton dissociation which subsequently gave the best performance when blended with PbS NCs, although they offered no explanation as to why this polymer worked better than others.[80]

Table 1.3 A survey of NC-based solar cell performance

Active material	V_{OC} [V]	J_{SC} [mA/cm^2]	FF	PCE [%]	Ref.
Polymer:NC blend hybrid cells					
P3HT:CdSe	0.45	5.70	0.4	1.7	[75]
P3HT:CdSe	0.62	8.79	0.50	2.9	[76]
PCPDTBT:CdSe	0.67	9.02	0.51	3.2	[77]
P3OT:CdTe	0.71	3.12	0.48	1.1	[78]
P3HT:PbSe	0.38	1.73	0.40	0.26	[79]
PDTPQx:PbS	0.38	4.20	0.34	0.55	[80]
Schottky cells					
PbSe	0.24	24.5	0.41	2.1	[81]
PbS	0.47	7.8	0.55	2.0	[82]
PbS	0.51	14.0	0.51	3.6	[83]
PbS_xSe_{1-x}	0.45	14.8	0.50	3.3	[84]
Bilayer cells					
CdSe/CdTe	0.45	13.2	0.49	2.9	[85]
$CuInSe_2$/ZnO	0.28	25.8	0.39	2.8	[86]
CuZnSnSSe/ZnO	0.43	31.2	0.54	7.2	[87]
PbSe/ZnO	0.44	24	0.32	3.4	[56]
SnS/PbS	0.35	4.2	0.27	0.5	[88]
PbS/a-Si	0.2	9.0	0.39	0.7	[89]
PbS/PCBM	0.59	10.0	0.63	3.7	[90]
PbS/ZnO	0.59	8.9	0.56	2.9	[91]
PbS/TiO_2	0.46	20.7	0.33	3.1	[92]
PbS/TiO_2	0.51	10.5	0.60	3.4	[93]
PbS/TiO_2	0.51	16.2	0.58	5.1	[94]

In a Schottky solar cell, band-bending occurs at the interface between the NC and metal electrode.[81] In this carrier-depleted region, an electric field is generated that drives exciton dissociation and the separation of electrons and holes.[81] Fabrication of NC Schottky cells can be a challenge since NC films have a tendency to possess cracks which will lead to a device short-circuit upon deposition of the top metal electrode, but Luther *et al.* overcame the problem by using a layer-by-layer (LBL) process to form their NC film.[81, 95] Their LBL method proceeds as follows: first a PbSe NC layer was deposited by dip-coating, after which it was treated with 1,2-ethanedithiol (EDT). The EDT was effective at displacing the original solubilizing oleic acid ligands, thus making the film insoluble and allowing another layer of PbSe NCs to be deposited. This process of dip-coating and EDT treatment was repeated several times, producing a robust crack-free film.[95] Furthermore, since EDT is a much shorter ligand than oleic acid, the coupling between adjacent NCs was much improved in the EDT treated film and resulted in a 30-60 fold improvement in conductivity.[95] PbSe NC Schottky cells were successfully fabricated using this LBL method, achieving a large J_{SC} of 24.5 mA/cm^2 and a PCE of 2.1 %.[81] The LBL method was further utilized in the fabrication of PbS[82, 83] and PbS_xSe_{1-x}[84] NC Schottky cells. A PCE of 3.6 % was reported for PbS,[83] while the ternary PbS_xSe_{1-x} system achieved an efficiency of 3.3 %.[84]

Schottky solar cells, however, suffer from the inherent disadvantage that the V_{OC} in practical devices is limited to about half the band-gap due to the details of the band-bending at the semiconductor-metal interface.[96] This problem is avoided in a bilayer NC/acceptor structure (**Figure 1.9(c)**) in which exciton dissociation and charge separation takes place at the semiconductor heterojunction rather than at the NC/metal interface. Clearly, the acceptor should be chosen so that it forms a type II heterojunction with the NC for efficient charge transfer to take place. In some cases,

both layers in the cell are NCs, such as the CdSe/CdTe[85] and the SnS/PbS[88] systems. In most bilayer cells, however, the acceptor is an n-type semiconductor such as ZnO,[56, 86, 87] TiO_2,[93, 94], PCBM,[90] or amorphous Si.[89] Details of the solar cell performances are listed in **Table 1.3**, where it can be seen that the best bilayer cells out-perform the best Schottky cells. Notable performances include a PbS/TiO2 system that gave 5.1 %,[94], and a CuZnSnSSe/ZnO cell that achieved 7.2 % efficiency.[87]

Although the development of NC solar cells started much later than organic solar cells, the field really took off in the last few years and reported PCEs are already comparable to or better than the best organic cells (**Table 1.1**). The future of NC solar cells looks very bright indeed.

Outline of the dissertation

In this first chapter, a background on the world's energy landscape and motivation for work on solution-processable solar cell technologies were given. Standard solar cell terminologies were defined and then progress in organic solar cells as well as inorganic nanocrystal solar cells was reviewed.

Chapter 2 goes into greater detail on the exciton dissociation process in organic solar cells. It is shown that a two-step exciton dissociation process is present, in which there is initially an energy-transfer of the exciton from the donor to the acceptor, followed by a back-ward charge transfer step from the acceptor to the donor. This work had been published in *Applied Physics Letters*.[97]

Chapter 3 describes a spray-deposition process for the deposition of both the active layer as well as the top electrode for polymer solar cells. This work was also published in *Applied Physics Letters*.[10]

In chapter 4, it is shown how a novel fluorinated photo-resist was utilized for the patterning of polymer solar cells to achieve a high-voltage solar cell array. This

work was published in the *Journal of Materials Chemistry*.[98]

Chapter 5 introduces a new family of electron-deficient pentacene-based acceptors to replace PCBM in organic solar cells. It is shown that these acceptors have good light absorption properties as well as good band alignment with P3HT thus producing high V_{OC}. Two papers were published from this work, one in *Journal of Materials Chemistry*[99] and the other in *Chemical Science*.[100]

Chapter 6 presents work on two more families of electron-deficient acene-based acceptors. Hexacenes absorb even further into the longer wavelengths of the solar spectrum, while anthradithiophenes have larger band-gaps that led to higher solar cell V_{OC}. Manuscripts of this work are in preparation.

Finally, chapter 7 presents a novel synthesis of copper oxide nanocrystals, as well as their optical and NC properties. Copper oxide is an earth-abundant material, and both CuO and Cu_2O possess attractive optical properties for light-harvesting applications. A CuO NC based solar cell is also demonstrated. A manuscript of this work is in preparation.

CHAPTER 2

ORGANIC PHOTOVOLTAIC CHARGE DISSOCIATION MECHANISM

Abstract

Charge and energy transfer are competing processes in many photo-excited organic donor/acceptor systems. Both processes can be the basis of the exciton dissociation mechanism occurring in organic solar cells. Deposition of a thin interlayer of a wide band-gap organic semiconductor between a P3HT/C_{60} heterojunction selectively suppressed electron transfer at the interface. External quantum efficiency measurements showed that device performance was unaffected by the presence of the electron blocking layer. These results can be explained by two-step exciton dissociation where energy transfer of excitons from the donor to the acceptor is followed by backward hole transfer to the donor. The same interlayer was shown to decrease the photocurrent in CuPc/C_{60} heterojunctions, a system where this energy transfer pathway is forbidden. Hence, both energy and charge transfer were shown to contribute to exciton dissociation.

Introduction

In 1992, the dissociation of photo-generated excitons in the semiconducting polymer MEH-PPV by means of electron transfer to C_{60} was reported.[19] This process was found to occur at a sub-picosecond time scale and to be very efficient.[19] As a result, this mode of exciton dissociation has been widely accepted as the primary mechanism underlying free carrier generation in polymer-based solar sells. A schematic of this exciton dissociation process by means of electron transfer is shown in **Figure 2.1**. Briefly, a photo-generated exciton diffuses to the organic hetero-junction, where

electron transfer from the donor to acceptor takes place, and then the charges are collected at the electrodes.

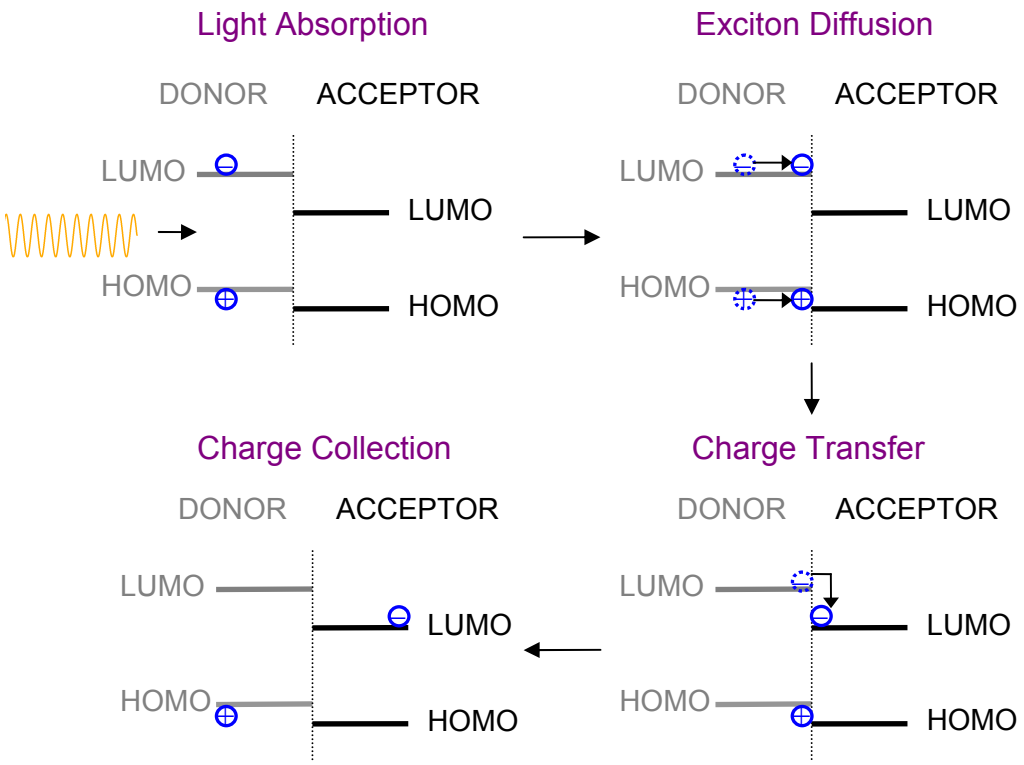

Figure 2.1 Charge transfer mechanism of exciton dissociation.

However, charge transfer and energy transfer have been known to be competing processes in many donor/acceptor (D/A) dyad systems.[101-104] Here "energy transfer" refers to Förster resonant energy transfer (FRET).[105] FRET takes place as a result of an oscillating dipole-dipole interaction between the donor and acceptor,[105], and its rate is given by[105]

$$k_{FRET} = \frac{1}{\tau_D}\frac{R_0^{\,6}}{R^6} \qquad \text{(Equation 2.1)}$$

where τ_D is the natural lifetime of the exciton in the donor in the absence of the

acceptor, R is the donor-acceptor separation distance, and R_0 is a length scale that depends on the donor-acceptor orientation as well as the amount of spectral overlap between the donor luminescence and acceptor absorption.[105] It is clear from **Equation 2.1** that these are all factors affecting FRET efficiency. In many conjugated oligomer–fullerene dyads, FRET from D to A was found to take place approximately two orders of magnitude faster than charge transfer, and was therefore a much more efficient process.[102, 103]

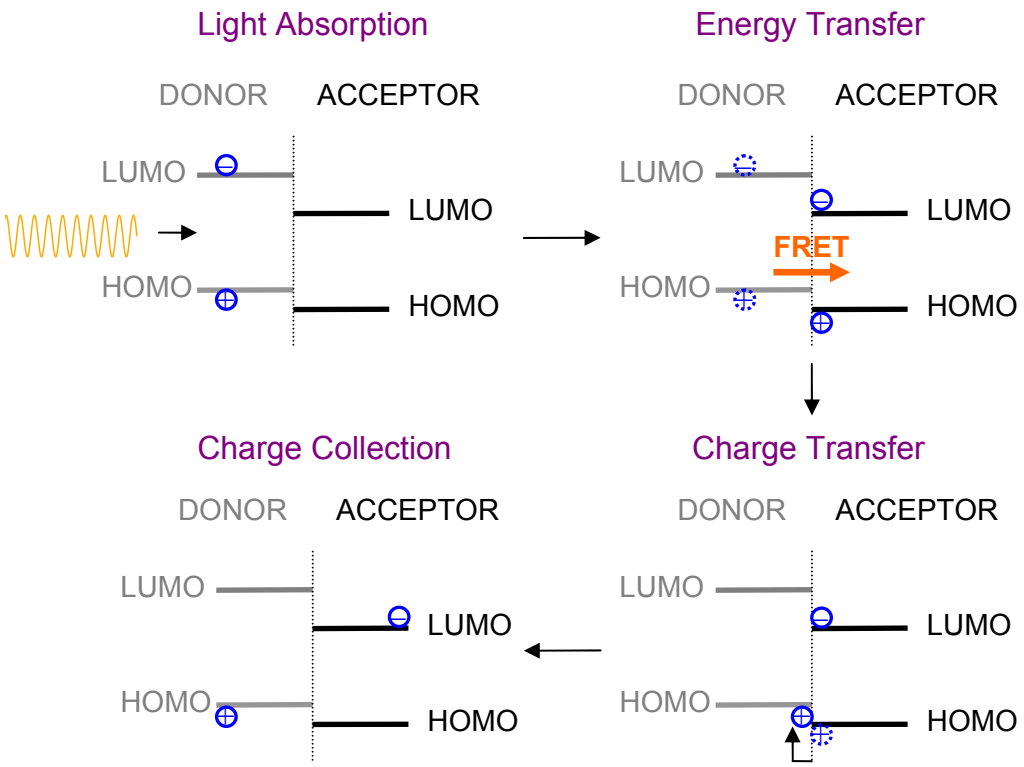

Figure 2.2 Two-step energy/charge transfer mechanism of exciton dissociation.

Given the prevalence of energy transfer in D/A dyads, it is possible that the same process takes place in polymer/fullerene hetero-junction solar cells. It is thus reasonable to expect that some fraction of excitons generated in the polymer may transfer directly to the fullerene via energy transfer. Exciton dissociation could then

occur as a two-step process whereby hole "back-transfer" to the polymer would follow FRET of excitons to C_{60}, as shown schematically in **Figure 2.2**. Such two-step processes have been measured in dyads in solution,[101-103] and there is indirect evidence for the two-step process between discrete D/A thin film.[106] However, direct observation is complicated by the ultra-fast nature of the energy transfer step; for instance, an attempt to observe the two-step process in a MDMO-PPV:PCBM blend using pump-probe spectroscopy was inconclusive due to the limited temporal resolution of the instrument.[104]

Vacuum deposited inter-layers provide a useful way to selectively interfere with charge and energy transfer pathways.[18, 107, 108] Inter-layers with a large energy gap have been employed as spacers between D and A layers to study energy transfer processes.[18] Moreover, inter-layers with appropriate HOMO and LUMO levels have been used extensively in vacuum deposited multilayer light emitting diodes to block holes or excitons at a particular layer within the device.[107, 108] By incorporating the appropriate vacuum deposited interlayer between the polymer and C_{60} hetero-junction, it should be possible to suppress electron transfer from the polymer to C_{60}, while sustaining energy transfer and allowing hole transfer back to the polymer.

In this work, the presence of FRET from P3HT to C_{60} was investigated. As mentioned in Chapter 1, P3HT is a popular donor material for polymer solar cells, with reported PCEs up to 5.2 %.[30-33] Since the P3HT band-gap of 1.9 eV[48] is higher than the C_{60} band-gap of 1.7 eV,[109] FRET should be energetically favorable. N,N′-bis (3-methylphenyl)-N,N′-bis(phenyl)-benzidine (TPD) was utilized as a vacuum deposited interlayer between solution deposited P3HT and vacuum deposited C_{60}. The low electron affinity of TPD (LUMO at ~2 eV) is expected to disrupt electron transfer from P3HT and C_{60}. On the other hand, energy transfer between P3HT and C_{60} should remain largely uninhibited for thin TPD films. Moreover, hole transfer from C_{60} to

P3HT remains energetically favorable. As a comparison, the low band-gap (1.6 eV[109]) material CuPc was also investigated. With a lower band-gap then C_{60}, FRET from CuPc to C_{60} is energetically unfavorable and should not take place. The molecular structures of the above materials are shown in **Figure 2.3**, while their HOMO-LUMO energy levels (taken from literature[48, 109, 110]) are given in **Figure 2.4**.

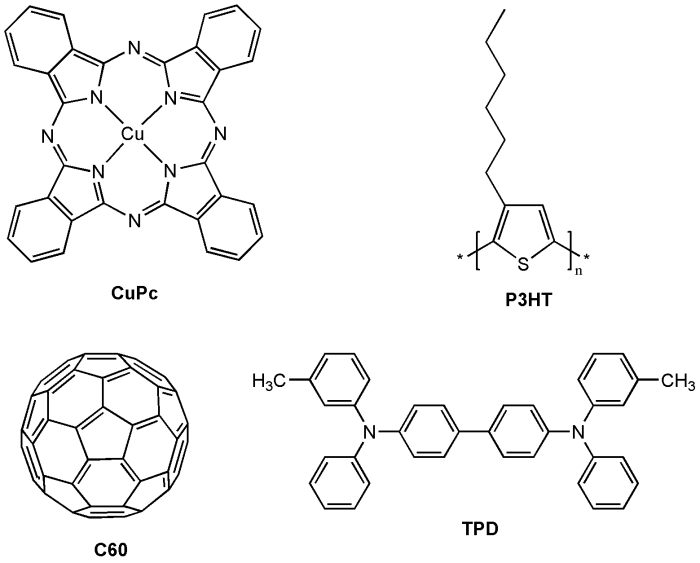

Figure 2.3 Molecular structures of materials used in this study.

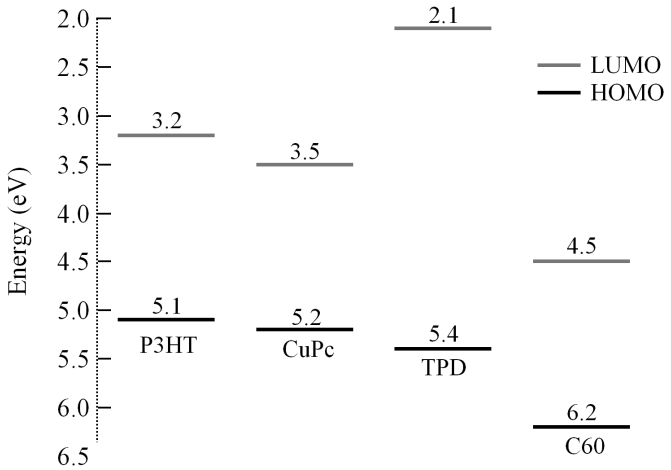

Figure 2.4 Energy levels of P3HT,[48] CuPc,[109] TPD,[110] and C_{60}.[109]

Experimental

All organic films were deposited on pre-patterned ITO electrodes, which were cleaned by sonication in a mild detergent, rinsed in deionized water, dried under a nitrogen stream, and followed by a 10 minute UV-ozone treatment. P3HT (Plextronics Inc.) was deposited from a chlorobenzene solution by spin coating. CuPc, TPD (Aldrich) and C_{60} (Term USA) were deposited under high vacuum ($<10^{-6}$ Torr) at rates of 0.2-0.5 Å/s. Reference films of the same thickness were deposited on quartz slides during device fabrication to obtain accurate UV-Vis absorption spectra. A shadow mask was used to deposit TPD inter-layers on part of the substrate. This allows data for devices with and without an interlayer to be compared on the same substrate. TPD deposition was carried out on all substrates simultaneously to ensure inter-layers of identical thickness. For the cathode, a 1000 Å thick Ag film was deposited at a rate of 1-5 Å/s.

Deposition rates were monitored by a quartz crystal monitor, and film thicknesses were verified by an ADE Phase Shift MicroXAM non-contact optical profilometer. A Digital Instruments DI3000 atomic force microscope (AFM) was used in tapping mode to characterize the surface roughness of the donor layers. External quantum efficiency measurements were performed with a 1000 Watt research lamp coupled to an Oriel Cornerstone ¼ m monochromator. Long-pass optical filters were introduced at 450 nm and 600 nm to eliminate spurious λ/2 illumination. The short-circuit current was monitored with a Keithley 236 source-measure unit. Intensity of the monochromatic light source was monitored with a Newport 1935-C power meter with a calibrated 918D low power detector.

Results and Discussion

The external quantum efficiency (EQE) is a measure of the number of charge carriers collected in the external circuit for every photon that is incident onto the solar cell at a

particular wavelength. It is calculated according to the formula:[111]

$$EQE(\%) = \frac{100 \times 1240 \times J_{SC}}{\lambda \times P_{INC}} \qquad \text{(Equation 2.2)}$$

where J_{SC} is the short-circuit current (mA/cm^2), λ is the wavelength of light (nm) and P_{INC} is the incident power intensity (mW/cm^2).

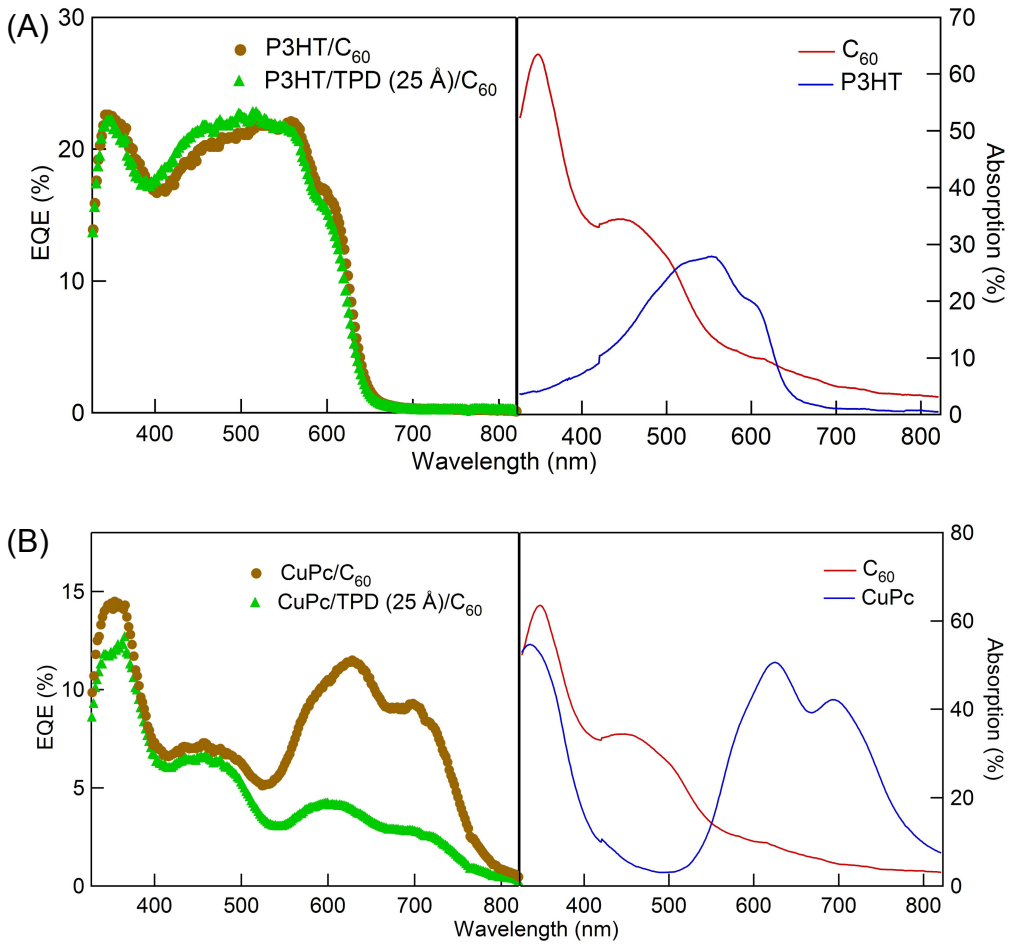

Figure 2.5 EQE of (a) P3HT/C_{60} and (b) CuPc/C_{60} hetero-junctions with and without a TPD inter-layer. UV-Vis absorption spectra of the layers are also indicated.

Figure 2.5(a) shows that the EQE of P3HT/C_{60} devices with and without a 25 Å thick TPD interlayer are approximately the same. In the region below 400 nm,

where light absorption predominately takes place in the C_{60} layer, the photocurrent is due to the dissociation of excitons formed within the C_{60} side of heterojunction. These excitons dissociate via hole transfer to P3HT, and the addition of the TPD layer is not expected to dramatically alter this process. This is consistent with the fact that the same EQE is measured in devices with and without the TPD layer. On the other hand, in the region between 500 and 600 nm, it is P3HT that dominates light absorption. The fact that the EQE remains largely unaffected by the introduction of the TPD interlayer indicates that energy transfer from P3HT to C_{60}, succeeded by exciton dissociation by hole-transfer back to P3HT, plays a major role in these hetero-junctions.

To better illustrate this point, the results above are contrasted to data from heterojunctions where energy transfer from the donor to the acceptor is not expected to take place. **Figure 2.5(b)** shows the EQE of CuPc/C_{60} devices with and without a TPD interlayer. As expected, the presence of the interlayer does not affect photocurrent generation in regions of the spectrum where C_{60} is absorbing the incident light. On the other hand, and in sharp contrast to the P3HT heterojunctions, there is an appreciable decrease in EQE in the region where CuPc is absorbing (above 600 nm). Since energy transfer from CuPc to C_{60} is forbidden due to the smaller band gap of CuPc, electron transfer from CuPc to C_{60} is the only mechanism for exciton dissociation in this region. The decrease in the EQE observed by the introduction of the TPD layer shows that the latter is effective in blocking electron transfer.

The above discussion is summarized schematically in **Figure 2.6**. The P3HT/C_{60} heterojunction corresponds to the left half of the figure where the two-step energy and charge transfer process takes place and photo-current is unaffected. On the other hand, the CuPc/C_{60} heterojunction is described by the right half where energy transfer is forbidden, thus photo-current is greatly reduced.

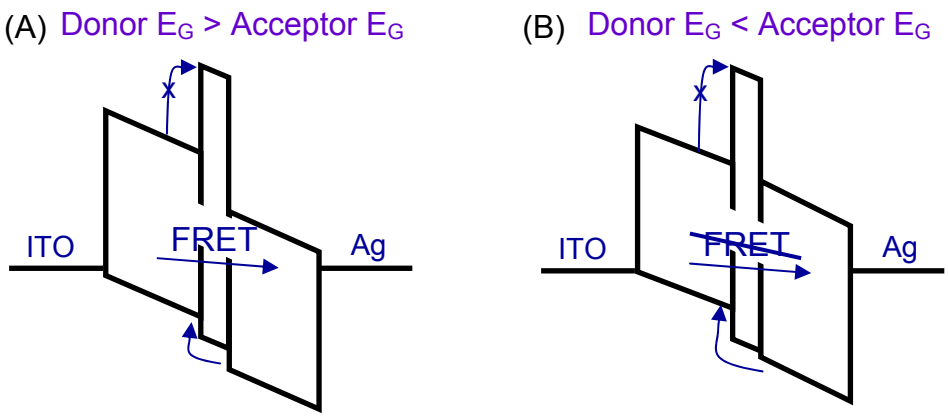

Figure 2.6 FRET outcomes for two different band-gap scenarios: (a) donor E_G is larger (b) acceptor E_G is larger.

The fact that the EQE of the CuPc/TPD/C_{60} device above 600 nm is not completely extinguished indicates that the TPD interlayer might not be continuous at this thickness. Indeed, for thicker interlayer films we see further suppression of the photocurrent in this regime (thicker inter-layers, however, also decrease energy transfer). The implication here is that some degree of electron transfer is still likely to take place in the P3HT/TPD/C_{60} devices. This makes it difficult to quantify the fraction of excitons in P3HT/C_{60} heterojunctions which dissociate directly via electron transfer versus via a two-step process involving energy transfer. Still, the difference in the behavior between P3HT and CuPc shows that two-step processes are important in heterojunctions utilizing the former as the donor.

High film roughness of the donor layers may contribute to an imperfectly formed TPD interlayer. A rough P3HT layer, for example, may result in a TPD layer with a high density of pin-holes. With sufficient contact between P3HT and C_{60}, normal charge transfer takes place which circumvents the electron blocking capacity of the interlayer. Atomic force microscopy (AFM) characterization of the films (**Figure 2.7**) effectively rules out surface roughness as a cause for incomplete

interlayer formation. The RMS surface roughness for P3HT is 1.32 nm. In contrast, the RMS roughness of vacuum deposited CuPc is 5.70 nm which is much higher than that of P3HT.

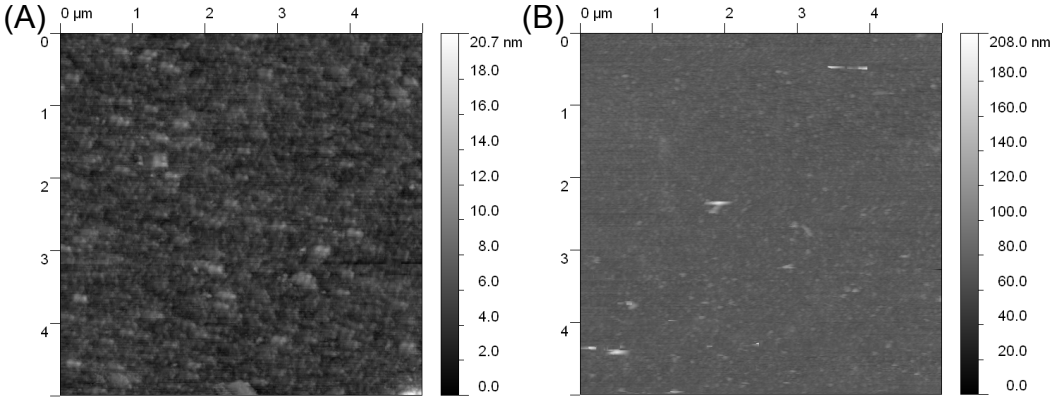

Figure 2.7 AFM images of (a) P3HT film (b) CuPc film.

Conclusion

In summary, the introduction of a thin TPD interlayer between P3HT and C_{60} did not affect the photocurrent in hetero-junction devices. The same interlayer caused a large decrease in the photocurrent in CuPc/C_{60} hetero-junctions in the region where light was absorbed by CuPc. These results are consistent with the presence of an energy transfer channel from P3HT to C_{60}. Therefore, exciton dissociation in P3HT/C_{60} heterojunctions can take place as a two-step process, where energy transfer from P3HT to C_{60} is followed by exciton dissociation via hole transfer to P3HT.

These findings can have substantial implications for the choice of active materials for organic solar cells. For instance, a recent paper building up on this work not only confirmed the findings presented here, but also demonstrated a more efficient solar cell by taking advantage of FRET.[112]

CHAPTER 3

SPRAY DEPOSITED ORGANIC SOLAR CELLS

Abstract

Spray deposition is emerging as an attractive low-cost, high throughput method for organic solar cell fabrication. In this work, it is demonstrated that a highly conductive formulation of poly(3,4-ethylenedioxythiophene)-poly(styrenesulfonate) (PEDOT:PSS) can be spray deposited to form the top electrode for an organic solar cell. An inverted solar cell fabricated in this way with a blend of P3HT and PCBM as the active layer achieved a power conversion efficiency of 2.0 % under AM 1.5 100 mW/cm^2 illumination.

Introduction

Organic solar cells have attracted much attention due to their potential for low-cost, high-throughput roll-to-roll manufacturing on flexible substrates.[6] Solution processing of the active material is the key for such a process.[6] There are many methods to deposit the active material by solution, such as doctor blading,[113] screen printing[7] and inkjet-printing.[8]

Recently, spray deposition has emerged as another attractive coating technique for organic solar cell fabrication.[9, 114] Vak *et al.*[9] reported a solar cell with an active layer that was spray-deposited from a blend of P3HT and PCBM, which achieved a power conversion efficiency (PCE) of 2.8 %. This is comparable to the performance obtained from spin-coated active layers, thus proving the viability of the spray approach. Spray deposition has the obvious advantage of being compatible with a high-throughput roll-to-roll process. It also results in less material wastage when

compared to spin-coating, and does not require careful optimization of the solvent formulation that is needed for inkjet printing.[8] Furthermore, unlike spin-coating, spray deposition tends to leave sequentially deposited layers intact and enables the fabrication of multi-layered devices.

All the above reported work,[7-9, 113, 114] however, utilized a vacuum step in which metal is thermally evaporated to form the top electrode for the cell, which is undesirable for a high-throughput process. In this work, it is shown that the metal electrode can be replaced by a spray-deposited highly conducting layer of poly(3,4-ethylenedioxythiophene)-poly(styrenesulfonate) (PEDOT:PSS). Ahlswede *et al.*[115] achieved conductivities as high as 300 S/cm by modifying Clevios PH 500, a highly conducting PEDOT:PSS formulation available commercially from H. C. Starck, with additives such as dimethylsulfoxide (DMSO) and Sorbitol. While it is still not absolutely certain as to the reasons for the increase in conductivity, it has been speculated that DMSO leads to a dielectric screening between the charge carriers and counter-ions in PEDOT:PSS, thus improving charge mobility.[115] There is also evidence that the additives lead to conformational changes in the PEDOT polymer chains, thus improving inter-chain interactions.[115] Such formulations have been utilized to replace indium tin oxide (ITO) as the anode in organic solar cells[115] as well as in organic light emitting diodes (OLEDs),[116] with performances comparable to the ITO-based anode devices. These successful demonstrations provided the inspiration in this work to use modified PH 500 as a replacement for the top metal electrode. Its rather high work function of ~5.0 eV,[116] however, implies that it will be more suitable as the anode of an inverted solar cell, since the traditional organic solar cell device structure has low work function metals like Ca/Al as the top cathode electrode.[15]

A schematic of our inverted device structure is shown in **Figure 3.1**. Cesium carbonate (Cs_2CO_3) has been shown to reduce the effective work function of ITO from 4.5 eV to 3.4 eV.[117] ITO modified in this way has been utilized as the cathode in efficient inverted organic solar cells,[117-119] with PCE as high as 4.2 % being reported.[119] The approximate energy level diagram is shown in **Figure 3.2**, with values taken from literature.[48, 116, 117]

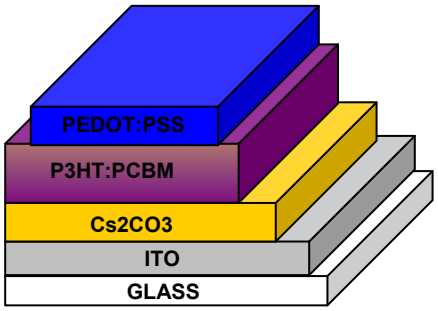

Figure 3.1 Inverted solar cell device schematic.

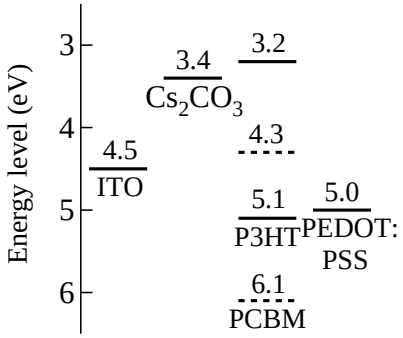

Figure 3.2 Device energy level diagram.

Experimental

Glass substrates with pre-patterned ITO electrodes (Kintec, Hong Kong) were cleaned by sonication in mild detergent, rinsed in de-ionized water, dried in a nitrogen stream,

and treated with a 10-minute UV-ozone exposure. The substrates were then transferred into a nitrogen-filled glovebox where all subsequent processing took place except for the spraying steps, which were done in air. A Cs_2CO_3 solution in 2-methoxyethanol (2 mg/ml) was spin-coated at 5000 rpm on top of the ITO, followed by annealing at 170 °C for 20 minutes.[119] PCBM (Nano-C) was added to a solution of P3HT (American Dye Source) in chlorobenzene (15 mg/ml) at a P3HT:PCBM ratio of 1:0.6 by weight, and this blend was spin-coated at a rate of 1500 rpm on top of Cs_2CO_3 to form the active layer with a thickness of ~150 nm. For comparison, devices with spray-deposited active layer were also fabricated. Substrates were pre-heated on a hotplate at 140 °C for two minutes, and 700 μl of P3HT:PCBM solution was spray deposited using a Badger 200G airbrush (**Figure 3.3**) held at a fixed distance of 17.5 cm above the substrate, at a N_2 spray pressure of 20 PSI. The spray solution was twice as concentrated as the one used for spin-coating, and a film thickness of ~1.2 μm was obtained. Since spray-deposition produced very rough films,[9] it was necessary for the film to be very thick in order to prevent short circuits.

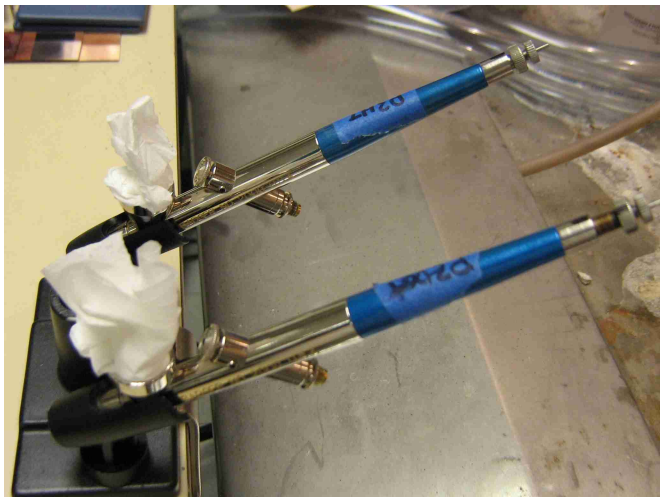

Figure 3.3 Badger air-brushes used for spray-coating.

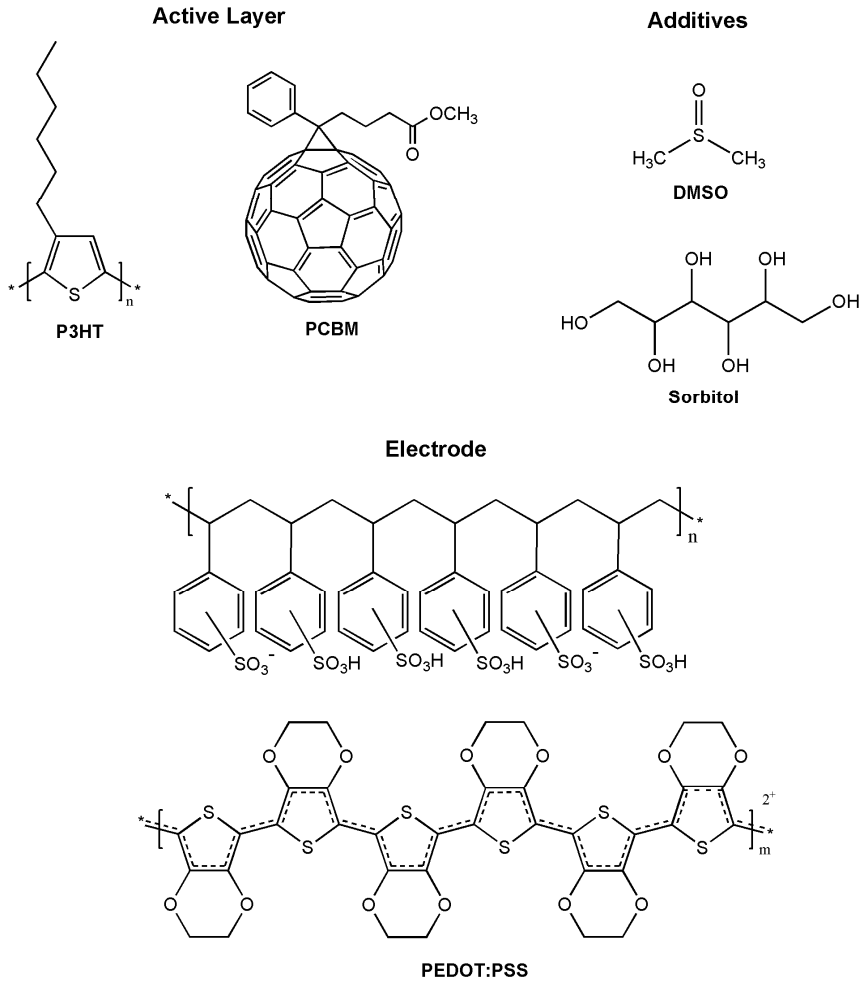

Figure 3.4 Molecular structures of materials used in this work.

The PEDOT:PSS formulation was prepared by blending DMSO (Aldrich) at 5 % volume with Clevios PH 500 (H. C. Starck), to which Sorbitol (Aldrich) was added at a concentration of 2 mg/ml.[115] The molecular structures of all the materials used in this work are shown in **Figure 3.4**. 1600 μl of the formulation was spray-deposited on top of the active layer through a shadow mask to form the top electrode with a thickness of ~2.1 μm. The airbrush was held at a distance of 16 cm from the substrate which was kept at 140 °C on the hotplate. The N_2 spray pressure was 20 PSI, as above. **Figure 3.5(a)** is a photograph of a single film of spray-deposited PEDOT:PSS, while

Figure 3.5(b) shows the completed devices with the patterned PEDOT:PSS electrodes on top of a spray-deposited P3HT:PCBM layer. 6 devices were obtained on each substrate, with an active device area of 3 mm^2.

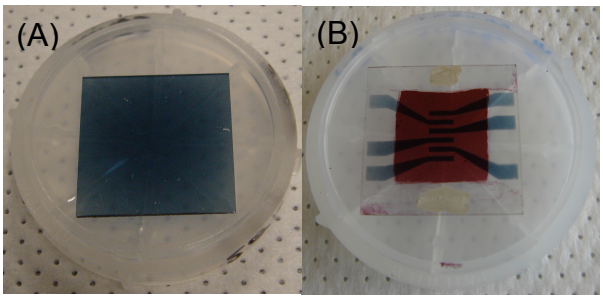

Figure 3.5 Photographs of spray-deposited PEDOT:PSS (a) single-layer film (b) electrodes patterned using a shadow mask.

The samples were annealed at 160 °C for 8 minutes in the glovebox to get rid of residual moisture in the film, as well as to induce favorable phase separation between P3HT and PCBM.[120] The samples were then transferred into a vacuum chamber and pumped down to ~10^{-6} Torr for an hour. This step improved performance significantly, presumably due to the removal of oxygen trapped in the device during the spray-coating step in air. In principle, the spraying could have been performed in a N_2 environment, and this step can then be omitted.

Control P3HT:PCBM cells with the standard device stack comprising of ITO/PEDOT:PSS/P3HT:PCBM/CsF/Al were also fabricated. The ITO substrates were cleaned as above, and then PEDOT:PSS (Clevios AI4083, used as received with no additives) was spin-coated at 6000 rpm followed by an annealing step at 170 °C for 4 minutes. P3HT:PCBM was then deposited in two different ways: (i) spin-coating at 1500 rpm from chlorobenzene solution (same recipe as above) (ii) spray-deposition using the same protocol as above, but with a smaller amount (300 μl) of solution.

CsF/Al were thermally evaporated at high vacuum (~10^{-6} Torr) to form the top electrode. A final thermal annealing step (160 °C for 8 minutes) was performed to optimize film morphology as before.[120]

Current-voltage characteristics of the completed devices were obtained with a Keithley 236 source-measurement-unit, both in the dark as well as under AM 1.5 100 mW/cm^2 illumination from a Solar Light 16S-002 solar simulator (calibrated by a Newport 818P-010-12 thermopile high power detector). Instrument control and data taking were done using a LabView program. Spectral mismatch was not taken into account in the measurements.

Results and Discussion

Current-voltage curves for the devices with PEDOT:PSS top electrode are shown in **Figure 3.6(a)**. The device with the spin-coated active layer achieved an open circuit voltage (V_{OC}) of 0.60 V, a short circuit current (J_{SC}) of 7.03 mA/cm^2, a fill factor (FF) of 0.48, and a respectable power conversion efficiency (PCE) of 2.0 %. The device with the spray-deposited active layer gave a 0.54 V V_{OC}, 2.36 mA/cm^2 J_{SC}, 0.29 FF and a PCE of 0.4 %. Charge collection efficiency is low in the very thick spray-deposited active layer, which explains its poor performance compared to the spin-coated device. The problem does not lie with the spray deposited active layer itself, since the control device with CsF/Al top electrode and spray-deposited active layer achieved a PCE of 2.2 % (**Figure 3.6(b)**), which is comparable to previous reports of spray-deposited cells.[9, 114] The thickness of the active layer in the control cell was ~0.5 μm, significantly thinner than the active layer of the all spray-deposited cell (~1.2 μm). We found that if the sprayed active layer thickness was kept at 0.5 μm and the PEDOT:PSS formulation was sprayed on top, short-circuited devices were the end result. It appears that the PEDOT:PSS penetrated the rough active layer more than Al,

hence the need for thicker active layers. Finally, it is worth mentioning that the control device with spin-coated active layer and evaporated CsF/Al top electrodes gave a PCE of 3.5 % (**Figure 3.6(b)**). Thus, the devices with the spray-deposited layers are still somewhat inferior, and it is likely that the film morphology of the sprayed layers is not as good as the spin-coated layers. The sprayed layers tend to be a lot rougher, for instance.[9] All the above results are summarized in **Table 3.1**.

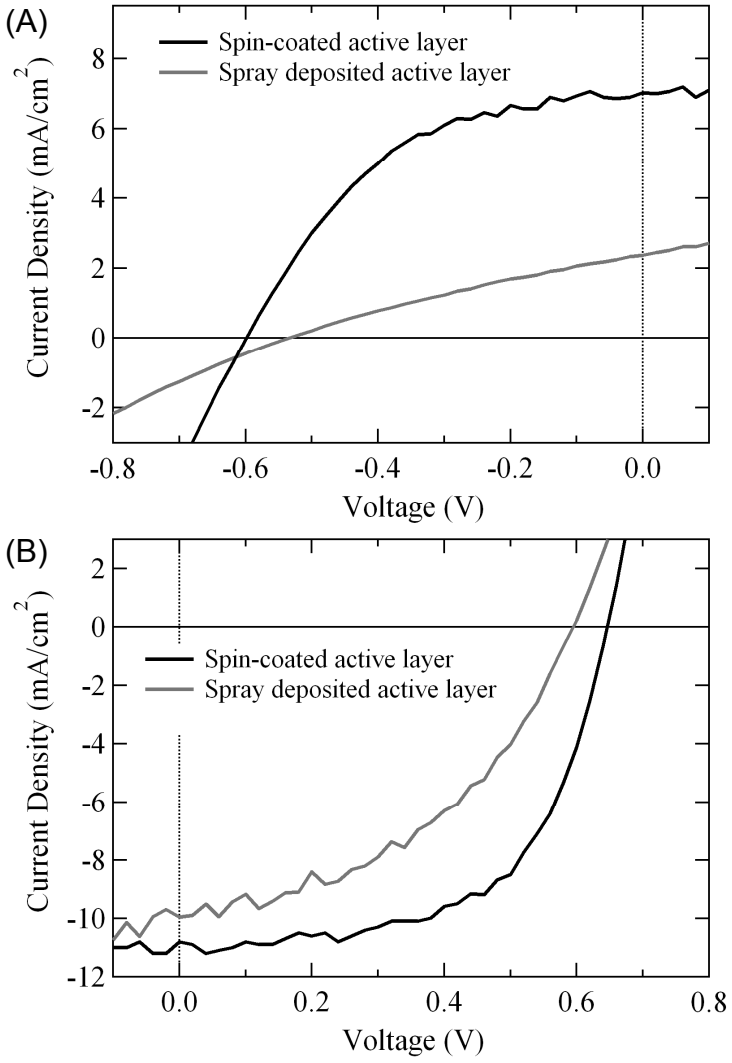

Figure 3.6 Current voltage curves for solar cells under AM 1.5 100 mW/cm^2 illumination with (a) PEDOT:PSS top electrode (b) CsF/Al top electrode.

Table 3.1 Summary of solar cell performance

Active material (P3HT:PCBM)	Top electrode[a]	V_{OC} [V]	J_{SC} [mA/cm^2]	FF	PCE [%]
Spin-coated	PEDOT:PSS	0.60	7.03	0.48	2.0
Spray-deposited	PEDOT:PSS	0.54	2.36	0.29	0.4
Spin-coated	CsF/Al	0.64	10.83	0.61	3.5
Spray-deposited	CsF/Al	0.60	9.95	0.43	2.2

[a] PEDOT:PSS top electrodes are spray-deposited, while CsF/Al top electrodes are thermally evaporated

To get a better idea of the quality of the PEDOT:PSS electrode, the sheet resistivity of single PEDOT:PSS films spray-deposited under similar conditions were measured with a 4-point probe. The sheet resistivity is calculated using the formula for a thin film:

$$R_S = \frac{\pi}{\ln 2}\left(\frac{V}{I}\right) \quad \text{(Equation 3.1)}$$

where I is the current measured by the 4-point probe at the voltage V. A value of R_S = 900 Ω/square was obtained, which is comparable to the value of 500 Ω/square reported by Ahlswede *et al.* for spin-coated layers.[115] Together with the film thickness of ~2.1 μm, this gives a conductivity of ~5 S/cm. The low value indicates that the composition and deposition of the PEDOT:PSS layer were probably not optimized, but the advantage of spray-deposition is that very thick films can be obtained which makes up for the low conductivity. Higher sheet resistances were previously obtained with thinner PEDOT:PSS films (for instance, 2800 Ω/square from a ~0.9 μm thick film). Furthermore, transparency or roughness are not important issues, since the PEDOT:PSS is used as the top contact.

Conclusion

It has been demonstrated that spray-deposited PEDOT:PSS can replace thermally evaporated metal as the top electrode in an inverted P3HT:PCBM solar cell. A device with a spin-coated active layer and spray-deposited PEDOT:PSS electrode achieved a PCE of 2.0 %. Devices with both the active layer and top electrode deposited by spraying are also possible, though the PCE is more modest (0.4 %). With further optimization, an all-spray-deposited organic solar cell may become a reality in the near future, paving the way for low-cost roll-to-roll manufacturing.

CHAPTER 4

HIGH VOLTAGE POLYMER SOLAR CELLS PATTERNED BY PHOTOLITHOGRAPHY

Abstract

An acid-sensitive semiperfluoroalkyl resorcinarene has recently been demonstrated as an effective photoresist for the photolithographic patterning of organic semiconductor materials. In this work, this novel photoresist is used to pattern polymer solar cells fabricated from a blend of P3HT and PCBM, so as to obtain high open circuit voltages (V_{OC}). An array of 300 solar cells in series, with a period of 50 μm, achieved a V_{OC} of 90 volts and a power conversion efficiency (PCE) of 0.3 %.

Introduction

Interest in high-voltage solar cells is motivated by applications in microelectromechanical systems (MEMS),[121, 122] which typically require driving voltages of tens to hundreds of volts. Such solar cells provide a self-contained power supply that allows for autonomous MEMS applications. These solar cells were fabricated from amorphous silicon, and achieved voltages above 100 volts by connecting miniaturized cells in series.[121, 122]

Recently, a high-voltage polymer solar cell fabricated from a blend of P3HT and PCBM has been demonstrated by Niggemann *et al*.[123] The P3HT:PCBM system represent one of the most promising material sets for organic solar cells, achieving efficiencies of around 5 %.[30-33] The advantage of using P3HT:PCBM solar cells is that in addition to possible applications in MEMs, they can be easily integrated into organic electronic applications to provide on-board power for organic thin film

transistors (OTFTs), which typically require operating voltages of tens of volts.[124]

To achieve high-voltage in a small area, the individual solar cells in the array need to be small (on the order of microns), hence patterning methods with high resolution are needed. Photolithography is an attractive technique, since it is well-established in the semiconductor industry and it can easily achieve sub-micron feature size. However, it is challenging to pattern organic electronic materials, as many of the processing steps in photolithography involve the use of solvents that can damage the organic layers. Niggemann *et al.* got around this problem by photolithographically patterning the electrodes first before spin-coating the active layer on top.[123] With sub-micron spacing between the electrodes, they achieved a 880-volt solar cell with a total electrode distance of just 17.4 mm.[123] However, their device architecture requires the active material to be sandwiched in a planar configuration between the electrodes (**Figure 4.1(a)**), and a rather low power conversion efficiency of 0.008 % was reported. The planar configuration is bad for charge collection since carriers have to travel a long distance to get to the electrodes. In Niggemann's cell, for instance, the spacing between the electrodes is about 500 nm[123] as compared to 100-200 nm for the average spin-coated active layer thickness,[17] and photolithography places limitations to making the feature sizes even smaller. Lewis *et al*. demonstrated another approach that utilized shadow masks to pattern top aluminum electrodes in series.[125] In this way, they were able to fabricate devices in the standard configuration, that is the active layer (P3HT:PCBM) being sandwiched vertically between the anode and cathode electrodes (**Figure 4.1(b)**). Their active layer thickness was 200 nm, and the array of 18 P3HT:PCBM cells achieved a voltage of 7.8 volts and a power conversion efficiency of 0.06 %.[125] However, it is difficult to achieve small features with shadow masking, and mask alignment is also a challenge.

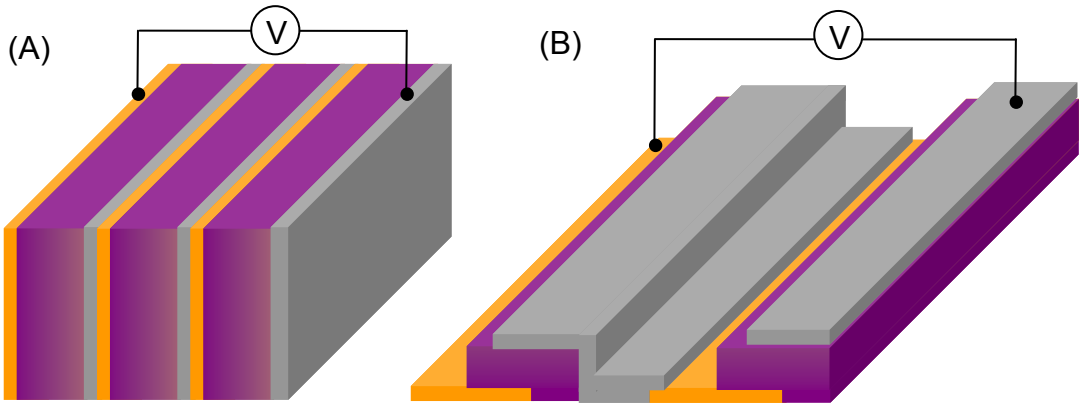

Figure 4.1 High-voltage solar cell array architectures: (a) planar configuration with the active layer sandwiched horizontally between electrodes (b) standard solar cells linked in series with the active layer sandwiched vertically between electrodes.

In this work a technique is demonstrated that can be used to directly pattern the organic active layer by photolithography in order to achieve high solar cell voltages. Previously, the Ober group at Cornell has shown that an acid-sensitive semiperfluoroalkyl resorcinarene is an effective photoresist for the photolithographic patterning of organic semiconductor materials.[126, 127] The resorcinarene is soluble in hydrofluoroethers (HFEs), which were found to be completely benign to non-fluorinated organic electronic materials.[126, 127] This is because materials with high fluorine content such as the resorcinarene and hydrofluoroethers are "fluorous" in nature,[128] and possess the unique property of being immiscible with both polar and organic (non-fluorinated) materials.[128] This is clearly illustrated by **Figure 4.2**, which shows a vial containing three immiscible photoluminescence solution layers: the top layer is poly(9,9-dioctylfluorene-*alt*-benzothiadiazole) (F8BT) dissolved in hexane, the middle layer is tris-(2,2'-bipyridyl)ruthenium (II) hexafluorophosphate ($[Ru(bpy)_3]^{2+}(PF_6^-)_2$) dissolved in water, and the bottom layer is a fluorinated light-emitting polymer (R_F-F8[129]) dissolved in hydrofluoroether. Since hydrophobic organic materials are already immiscible with polar materials, fluorous materials

provide a third "orthogonal" direction (**Figure 4.2**) in terms of solvent immiscibility and opens up new opportunities for materials processing. For instance, fluorinated light-emitting polymers have been reported and are shown to be robust against standard organic solvents.[129, 130]

Figure 4.2 Vial with three immiscible solution layers: F8BT in hexane, $[Ru(bpy)_3]^{2+}(PF_6^-)_2$ in water, and a fluorinated polymer in hydrofluoroether (image courtesy of Dr. Alexander Zakhidov).

The resorcinarene photoresist can thus be spin-coated from hydrofluoroether solution directly on top of the organic active layer. There will be no damage to the organic layer due to the orthogonal nature of the fluorous and organic materials (**Figure 4.2**). An array of 300 P3HT:PCBM solar cells was patterned in this way and connected in series, achieving an open circuit voltage (V_{OC}) of almost 90 volts. With this technique, it is possible to achieve high resolution using photolithography, and also incorporate the standard device architecture that has been optimized for polymer solar cells (**Figure 4.1(b)**).

Experimental

A schematic of the device fabrication process is shown in **Figure 4.3**. Glass substrates with unpatterned 15 Ω/ square indium tin oxide (ITO) (Kintec, Hong Kong) were cleaned by sonication in mild detergent, rinsed in de-ionized water, dried in a nitrogen stream and treated with a 10-min UV-ozone exposure. The ITO was then patterned

with standard photolithography. Shipley 1813 photoresist was spin-coated onto the ITO, which was then selectively exposed using a HTG System III-HR Contact Aligner before being developed with AZ 300 MIF developer. The patterned photoresist was used as a mask for the wet etching of ITO by hydrochloric acid, which yielded an array of 300 ITO electrodes with a width of 40 μm and a 10 μm gap between electrodes (hence a 50 μm period). Residual photoresist was removed with acetone and isopropanol (IPA).

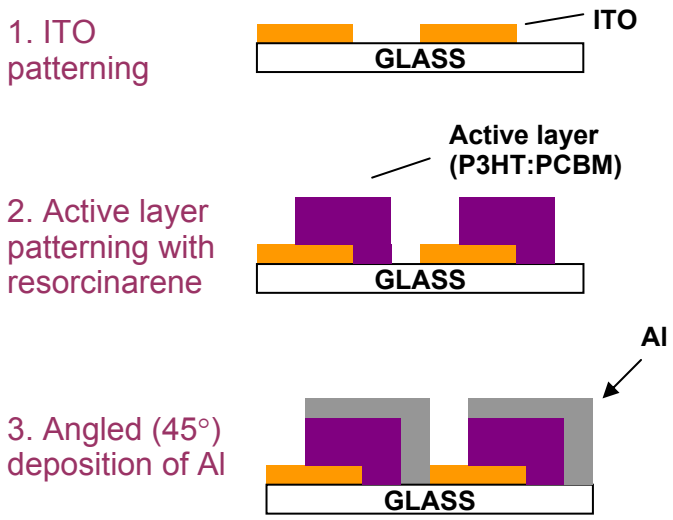

Figure 4.3 Schematic of the device patterning process.

The ITO array was cleaned once again by the same process as described above. PEDOT:PSS (Clevios PH 500) was then spin-coated on top at 6000 rpm, and then baked on the hot-plate at 170 °C for 4 minutes. P3HT (American Dye Source) was dissolved in 1,2-dichlorobenzene at a concentration of 17 mg/ml, to which PCBM (Nano-C) was added at a concentration of 10 mg/ml (for a total of 27 mg/ml). The P3HT:PCBM blend was spin-coated at 600 rpm on top of the PEDOT:PSS to give a film about 200 nm thick.

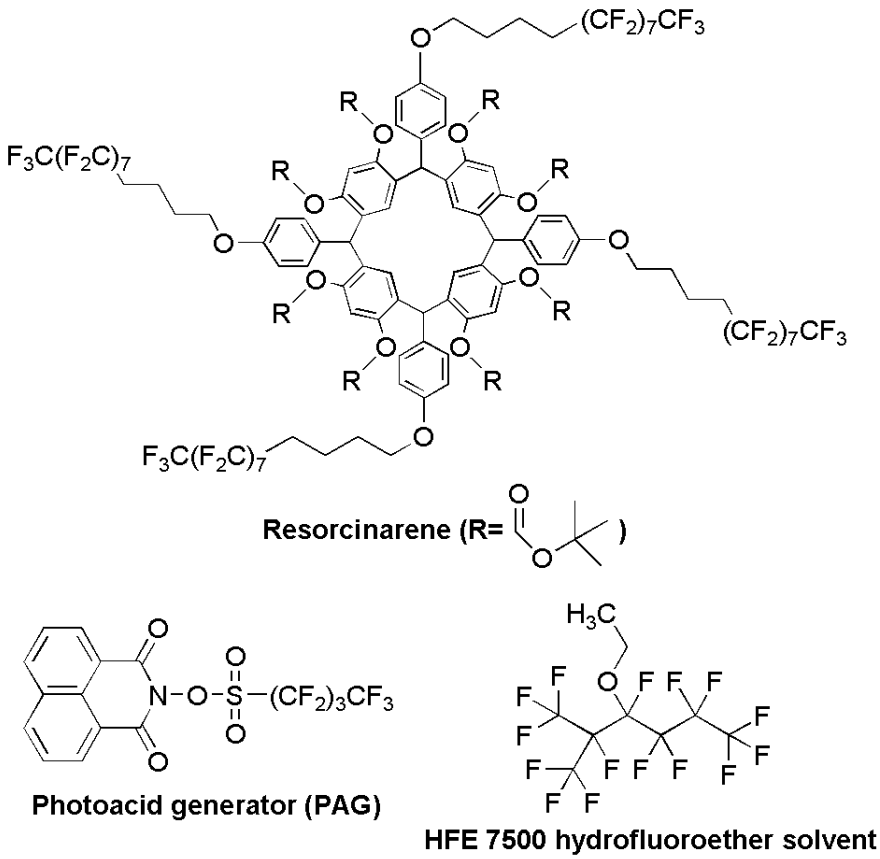

Figure 4.4 Materials for fluorinated resorcinarene photoresist.

The molecular structures of the materials used for the photoresist are shown in **Figure 4.4**. The resorcinarene and photoacid generator (PAG) were synthesized by Dr. Jin-Kyun Lee from the Ober group at Cornell. A mixture of the resorcinarene and a small amount of PAG (20:1 by weight) was dissolved in a 5:2 solvent mixture of HFE 7500 hydrofluoroether solvent (3M) and propylene glycol methyl ether acetate (PGMEA) at a concentration of 20 % by weight. The purpose of PGMEA was to improve the solubility of the resorcinarene. PGMEA was found to have only a small effect on the performance of P3HT transistors,[126, 127] and had been utilized in the photolithographic patterning of P3HT.[131] This formulation was spin-coated on top of the P3HT:PCBM layer at 1000 rpm to form a photoresist about 1 μm thick.

The photoresist was patterned by selective exposure with a GCA Autostep 200 DSW i-line Wafer Stepper, baked at 70 °C for a minute, and then developed using HFE 7200 (3M) solvent. The patterned photoresist was then used as a mask for the dry etching of the P3HT:PCBM and PEDOT:PSS layers by oxygen plasma with a Oxford PlasmaLab 80+ RIE System. The residual photoresist was stripped by dipping the films into HFE 7200 with 10 % IPA. The addition of a small amount of IPA allows the HFE 7200 to dissolve the previously insoluble parts of the photoresist. The patterned active layer was designed to have a 5 μm offset with respect to the ITO, so that the effective width of the active region was 35 μm (**Figure 4.5**). Since the array had a period of 50 μm, this implied that the active region was 70 % of the total cell area. An optical microscopy image of the patterned ITO electrodes and active layers is shown in **Figure 4.6**.

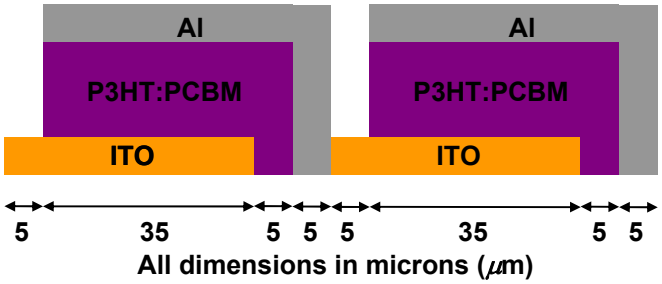

Figure 4.5 Dimensions of the solar cell array.

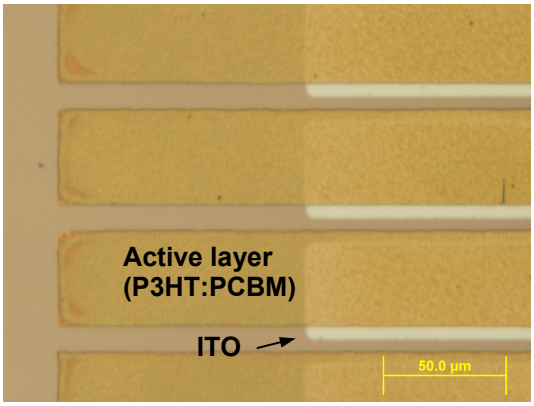

Figure 4.6 Optical microscopy image of patterned ITO and active layers.

Finally, 4 Å of CsF and 300 Å of Al were deposited through a shadow mask by thermal evaporation under high vacuum (~10^{-6} torr) to create top electrodes with a width of 3 mm. The substrate was tilted at an angle of 45° with respect to the incoming stream of Al atoms (as shown in **Figure 4.3**) so that the Al will not come into contact with the bottom ITO as a result of the shadowing effect by the P3HT:PCBM active layer thus avoiding a short circuit. However, the Al electrode will be in contact with the ITO electrode of the adjacent cell, hence forming a series connection. The final configuration is an array of 300 solar cells in series, with a total length of 15 mm and width of 3 mm, which gives a total cell area of 45 mm^2. A plan view of the completed device is shown in **Figure 4.7**.

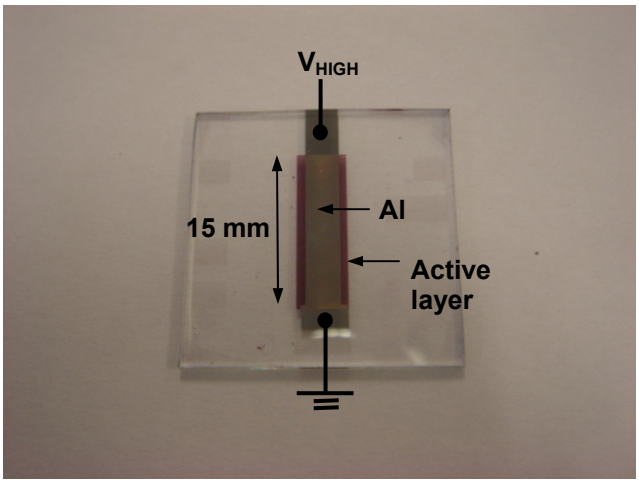

Figure 4.7 Photograph showing plan view of finished device.

For solar cell characterization, current-voltage (I-V) curves were obtained with a Keithley 236 source-measurement-unit (SMU) under AM 1.5 100 mW/cm^2 illumination from a Solar Light 16S-002 solar simulator. The light output power was calibrated using a Newport 818P-010-12 thermopile high power detector, which has a flat response over a broad spectral range. A LabView program was used for instrument control and data acquisition.

Results and Discussion

Various solar cell parameters, such as the open circuit voltage (V_{OC}), short circuit current (J_{SC}), fill factor (FF) and power conversion efficiency (PCE) were calculated from the I-V curves. The device was annealed at 160 °C on a hotplate for 80 minutes, and was tested several times during the course of the annealing process. Solar cell characteristics as a function of annealing time are tabulated in **Table 4.1**.

Table 4.1 Solar cell performance as a function of annealing time.

Annealing Time [min]	V_{OC} [V]	J_{SC} [mA/cm^2]	FF	PCE [%]
0	0.36	0.001	0.26	0.0001
8	65.4	0.016	0.32	0.35
16	77.4	0.017	0.34	0.44
32	84.2	0.016	0.30	0.41
48	86.0	0.016	0.26	0.35
64	89.0	0.016	0.24	0.34
80	89.6	0.014	0.24	0.31

The cell had a negligible V_{OC} before thermal annealing, which is likely to be a result of imperfect Al shadowing by the active layer, creating microscopic shorts across the devices. A brief thermal annealing (8 minutes) caused the V_{OC} to increase dramatically from 0.36 volts to 65.4 volts. Thermal annealing had been shown to lead to a restructuring of the organic layers,[29] which will help eliminate microscopic shorts.[111] The highest PCE of 0.44 % was achieved after 16 minutes of annealing, which is significantly better than previous reported values for high-voltage polymer cells.[123, 125] Further annealing decreased the PCE to 0.31 %, but V_{OC} increased steadily to reach 89.6 volts after 80 minutes. This increase in V_{OC} with thermal annealing is reproducible and had been observed for cells with different thicknesses of the Al cathode. Evaporating a thick layer of Al will worsen the problem of

microscopic shorts and lead to a lower final V_{OC}, while reducing the thickness will increase series resistance. The thickness reported here (300 Å) was found to be optimum.

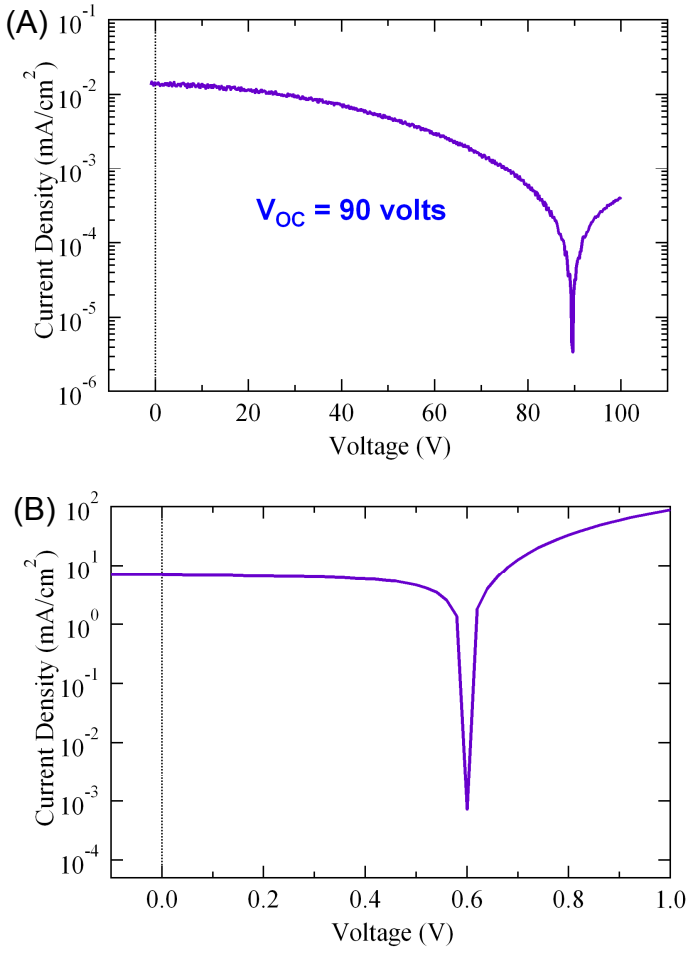

Figure 4.8 Current voltage solar cell curves of (a) high-voltage solar cell array (b) single solar cell as control.

The final current-voltage curve of the solar cell array under AM 1.5 100 mW/cm^2 illumination is shown in **Figure 4.8(a)**. The average voltage per cell is 0.3 volts, while the current density for a single cell in the array is 4.2 mA/cm^2 (assuming that each cell contributes the same current). The poor fill factor of 0.3 is likely due to

the high series resistance R_S, which is estimated to be 10^5 Ω/cm^2. This is perhaps to be expected, since there are 300 ITO-organic and 300 organic-metal junctions. In order to make a comparison, a single stand-alone 3 mm^2 P3HT:PCBM cell was fabricated under essentially the same conditions as the solar cell array but without the photolithographic patterning steps. The current-voltage curve of this cell is shown in **Figure 4.8(b).** It achieved a V_{OC} of 0.60 volts, J_{SC} of 7.0 mA/cm^2, FF of 0.59 and a PCE of 2.48 %, with a series resistance $R_S \sim 3$ Ω/cm^2. Thus, both the voltage and current values of a single cell in the solar cell array are at least half that of the stand-alone control cell, which indicates that the array device architecture does not suffer from a huge performance drop. Even with the low fill factor taken into account, the PCE is still a fairly respectable 0.3 %, and compares favorably with previous reports of high-voltage organic solar cells.[123, 125] This result also indicates that the P3HT:PCBM layer can undergo oxygen plasma treatment while it is protected by the fluorinated photoresist, thus the P3HT:PCBM system appears to be fairly robust.

Conclusion

A high-voltage polymer solar cell array was successfully patterned using photolithography. The array produced an open circuit voltage approaching 90 volts, with a power conversion efficiency of 0.3 % under AM 1.5 100 mW/cm^2 illumination. The V_{OC} and J_{SC} of a single cell in the 300-cell array are shown to be at least half that of a single stand-alone control cell fabricated under similar conditions. This indicates that photolithographic patterning via perfluorinated resocinarene photoresist is a viable technique for the fabrication of high-voltage polymer solar cells.

CHAPTER 5

ELECTRON DEFICIENT PENTACENES AS ACCEPTORS FOR ORGANIC SOLAR CELLS

Abstract

A series of electron deficient pentacenes have been synthesized, and characterized for their effectiveness as acceptors in polymer bulk-heterojunction solar cells using P3HT as the donor material. All of the materials reported here were effective acceptors, including 6,13-bis(triisopropylsilylethynyl) (TIPS) pentacene, a known high mobility p-channel organic semiconductor. Variations in the position and nature of the electron-withdrawing group on the pentacene core allowed tuning of device open-circuit voltage (V_{OC}), while photocurrent was strongly correlated with acceptor crystal packing motif. Materials with 2D π-stacking interactions were found to perform poorly in comparison to materials with 1D π-stacking interactions. Tuning the trialkylsilylethynyl substitution on the most promising candidates surveyed led to a number of derivatives with power conversion efficiencies (PCE) greater than 1 %, and the best pentacene acceptor gave reproducible performance in excess of 1.2 %.

Introduction

The majority of research in the field of organic solar cells has centered on the development of new donor polymers,[35, 41-46, 132] and on improvements in processing conditions to yield optimum morphologies for charge transport.[26, 29, 34, 36] C_{60} and C_{70} based fullerene derivatives have remained the de-facto standard acceptor in these systems,[35, 41-46, 132] and numerous design rules have been developed to yield improved polymer devices based on these acceptors.[38] PCBM (and $PC_{71}BM$) remains the most

commonly used n-type material since the conception of bulk-heterojunction cells (see **Table 1.1**), recently yielding conversion efficiencies approaching 8 %.[41]

Due to the impressive performance of fullerene-based acceptors, efforts to discover new acceptors for polymer bulk-heterojunction cells have to-date been quite limited.[133] The success of PCBM as a champion acceptor for organic solar cells is due to its ability to accept electrons from semiconducting polymers at ultrafast ($\sim 10^{-12}$ s) time scales,[19] and the nano-scale interpenetrating network that it forms with these polymers.[29] However, fullerenes suffer from several disadvantages such as poor light absorption in the visible spectrum,[134] hence they do not contribute significantly to the photocurrent of the solar cell. They are also known to produce reactive singlet oxygen under photo-excitation,[134] which can lead to device degradation. Furthermore, the synthesis of fullerenes typically involves high-temperature steps,[135, 136] hence fullerene production can be rather energy-intensive. In addition, freshly prepared fullerenes exist as a mixture of several products, and their purification can be challenging.[137]

Besides PCBM and other fullerene derivatives, efficient organic solar cells have been fabricated predominantly from polymeric acceptors, with best reported efficiencies around 1.8 %.[138-140] Polymeric acceptors have the advantages of good absorption in the visible and a higher LUMO energy level than PCBM, giving rise to a higher open-circuit voltage (V_{OC}).[138-140] The polydispersity of polymers, however, increases fabrication complexity since performance has been shown to be correlated to molecular weight.[141] Furthermore, electron transport in some polymer acceptors is trap-limited,[142, 143] which reduces fill factor and lowers efficiency.

The limitations of fullerene and polymeric acceptors make it desirable to explore non-fullerene small-molecule acceptors. Such acceptors, however, have performed rather poorly and are somewhat inferior to polymers. Acceptors based on

chromophores such as perylene diimide,[144] vinazene,[145] and diketopyrrolopyrrole[146, 147] derivatives yielded bulk-heterojunction solar cells with power conversion efficiencies of 0.55 %, 0.75 % and 1.0 % respectively. Recently, Brunetti *et al.*[148] demonstrated an acceptor based on the 9,9'-bifluorenylidene back-bone which achieved a PCE of 1.7 % in a solar cell with P3HT as the donor, which is the best performance for non-fullerene small-molecule acceptors so far.

The ease with which pentacene-based small-molecule acceptors can be synthetically tuned to improve charge transfer, charge transport and film morphology makes these compounds ideal candidates for a systematic study of their structure-property relationships as bulk-heterojunction photovoltaic acceptors.[149] Adding a new class of high-performance acceptors to the suite of materials currently used for solar cell fabrication will further understanding of the transport and phase separation properties of acceptor systems in polymer bulk-heterojunction solar cells, and could yield molecular design insights for the improvement of organic photovoltaic acceptors, fullerene-based or otherwise. Thus a key aspect for such small molecule systems is their compatibility with currently optimized deposition techniques – these new acceptors must be studied essentially as drop-in replacements for PCBM, without excessive departure from the traditional processing techniques or device configuration.

This work is a survey of soluble pentacene derivatives with electron-withdrawing groups on the pentacene core. The impact of these groups on the open-circuit voltage (V_{OC}) of P3HT / pentacene bulk-heterojunction solar cells and the optimization of top candidates are reported. While transistor studies have shown that the addition of numerous electron-withdrawing groups is required to yield good n-type performance in pentacene-based semiconductors,[150] initial investigation of cyanopentacenes as organic photovoltaic acceptors showed that this high degree of substitution results in low V_{OC} in solar cells; the best performance was obtained from

derivatives substituted with a single electron-withdrawing group. Inspired by this result, a series of pentacene derivatives substituted with a single electron-withdrawing group were synthesized and studied. Chloro, nitro, trifluoromethyl, perfluoroethyl and carboxymethyl derivatives were prepared. Recent reports of the positional sensitivity of electronic characteristics in pentacene derivatives[151] inspired the synthesis of derivatives containing the electron-withdrawing group at both the 1- and 2-position on the acene ring. Since initial investigations were focused on optimizing V_{OC}, only the triisopropylsilyl derivatives were originally prepared. Once materials with the best V_{OC} were determined, the grain size and transport properties of the acceptors were then optimized by alterations in the trialkylsilyl group. Several of the resulting materials yield photovoltaic cells with power conversion efficiency (PCE) greater than 1.0 %, and the best performing derivatives show PCE > 1.2 %.

Experimental

Most of the pentacene derivatives reported in this work were synthesized by Ying Shu from the Anthony group at the University of Kentucky, with contributions from Dr. Zhong Li and Balaji Purushothaman. Only the general synthetic schemes will be reported here; further details can be found in the published literature.[99, 100]

The synthesis of trialkylsilylethynyl-substituted cyanopentacenes (**Figure 5.1**) began by the condensation of 4,5-diiodobenzene-1,2-dicarbaldehyde[152] with either 1,4-cyclohexanedione, or 1,4-dihydroxyanthracene to yield tetraiodo or diiodo pentacenequinone. Ethynylithium solutions were prepared by treatment of the alkyne with n-butyl lithium, followed by addition of the quinone. After the quinone was fully dissolved, the reaction was quenched with saturated ammonium chloride solution, and the crude diol was isolated via silica chromatography. The diol was then deoxygenated and the resulting trialkylsilylethynyl iodopentacenes

were recrystallized from hexanes. They were then treated with KCN in the presence of a palladium catalyst and CuI to yield the desired cyanopentacenes. The reaction products are shown in **Figure 5.2**. Compound **1** was obtained as a by-product of the synthesis of compound **4**.

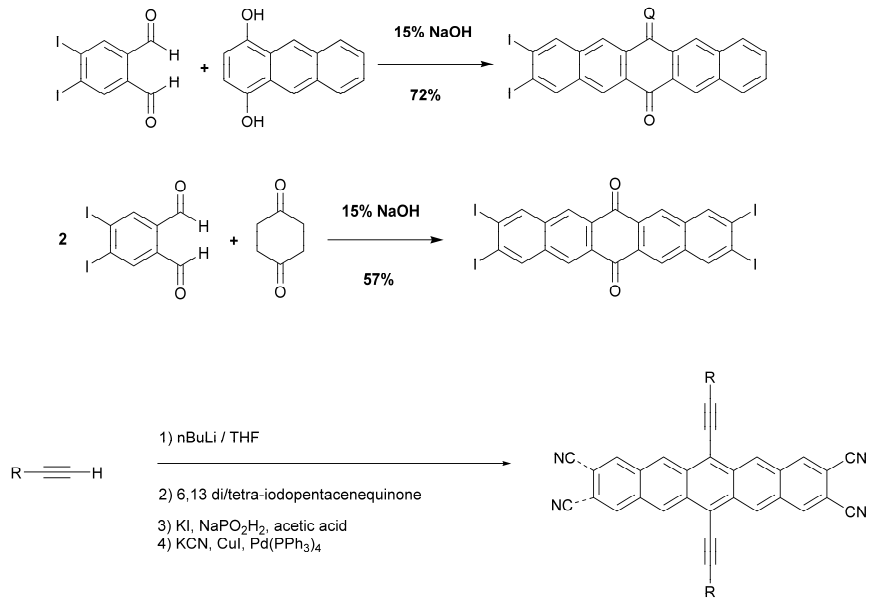

Figure 5.1 General scheme for the synthesis of cyanopentacenes.

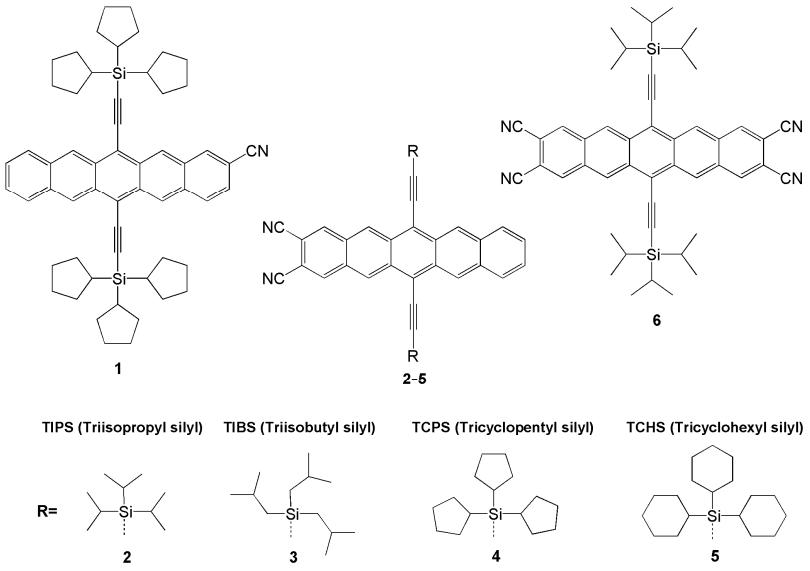

Figure 5.2 Molecular structures of the cyanopentacenes.

The synthesis of the mono-substituted triisopropylsilyl pentacene targets is straightforward, generally arising from the addition of a lithium acetylide to the corresponding pentacenequinone, followed by deoxygenation with stannous chloride. Most of the necessary quinones were prepared either by aldol condensation between a substituted phthalaldehyde and 1,4-dihydroxyanthracene, or Cava reaction between an a,a,a'-tribromo o-xylene and 1,4-anthraquinone (**Figure 5.3**). The carboxymethyl derivative could not be prepared in this fashion, due to the higher reactivity of the acene substituent. In this case, the corresponding iodopentacene was first synthesized, followed by Pd-mediated coupling of the desired functional group onto the pentacene core (similar to the cyanopentacene synthesis). The synthetic products are shown in **Figure 5.4**. The un-substituted 6,13-bis(triisopropylsilylethynyl) (TIPS) pentacene (compound **14**) is also tested for comparison.

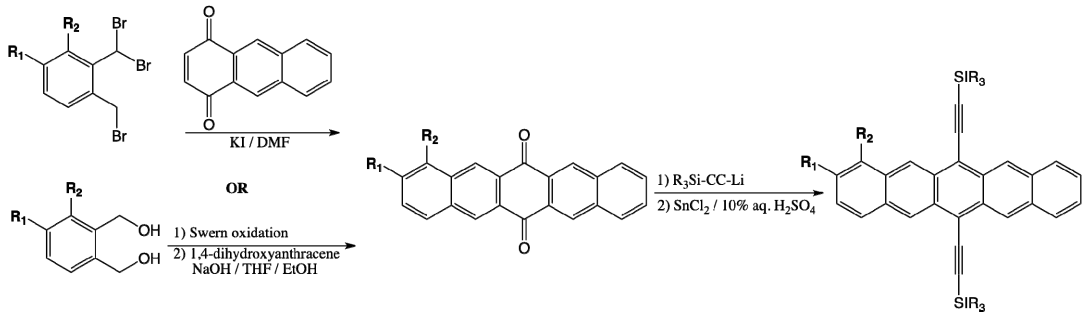

Figure 5.3 General synthetic approach to electron-deficient mono-substituted pentacenes (for $\mathbf{R_1}$ or $\mathbf{R_2}$ = CF_3, Cl, CF_2CF_3, or NO_2 and $\mathbf{R_3}$ = triisopropyl).

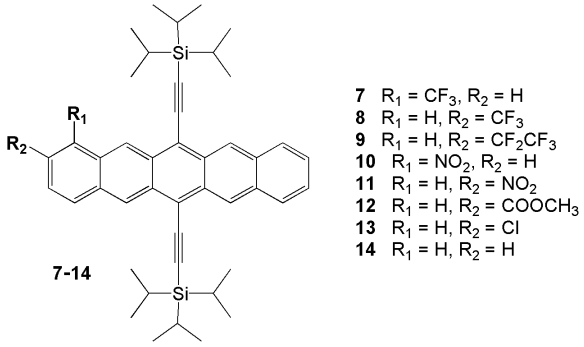

Figure 5.4 Molecular structures of the mono-substituted pentacenes.

In order to estimate the HOMO and LUMO energies of these new materials, the compounds were subjected to solution electrochemical analysis by differential pulse voltammetry. This was performed with a BAS CV-50W voltammetric analyzer at room temperature with a platinum button working electrode, a platinum wire counter electrode and a silver wire pseudo-reference electrode, in a nitrogen-purged 0.1M Bu_4NPF_6 solution in dichloromethane, using ferrocene/ferrocenium (Fc/Fc^+) as an internal standard at a scan rate of 20 mV/s. The HOMO and LUMO levels are then calculated based on their values relative to Fc/Fc^+ (4.8 eV), and are tabulated in **Table 5.1**.

Table 5.1 HOMO and LUMO energy levels calculated from electrochemical data.

Compound	HOMO [eV]	LUMO [eV]	E_G [eV]
1	5.31	3.50	1.81
2	5.44	3.63	1.81
3	5.44	3.64	1.80
4	5.47	3.64	1.83
5	5.45	3.63	1.82
6	5.75	3.91	1.84
7	5.28	3.41	1.88
8	5.29	3.45	1.84
9	5.32	3.42	1.90
10	5.34	3.52	1.82
11	5.34	3.55	1.79
12	5.26	3.49	1.77
13	5.17	3.33	1.84
14	5.16	3.35	1.82
PCBM	6.10	3.70	2.40
P3HT	5.16	~3.2	~1.9

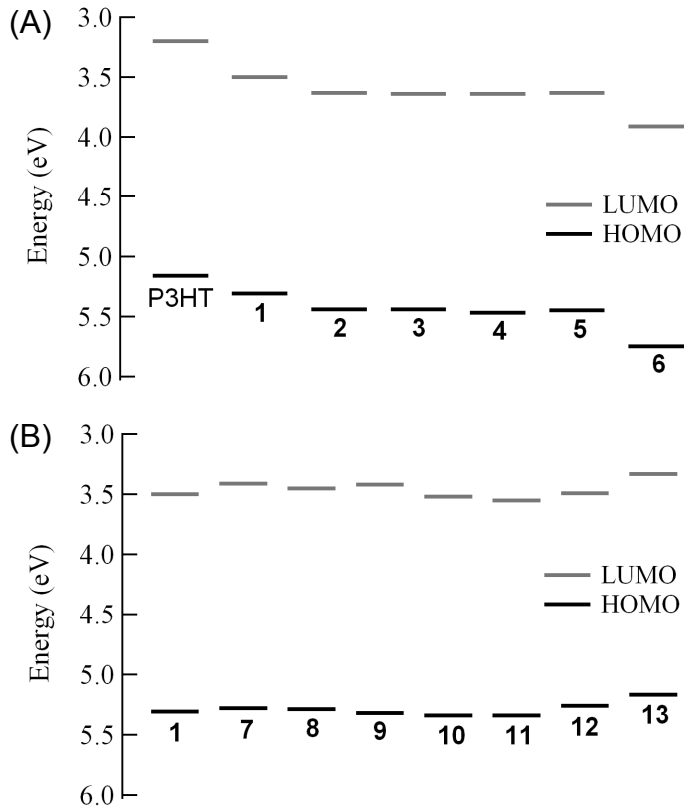

Figure 5.5 Plot of HOMO and LUMO energy levels of (a) cyanopentacenes (b) mono-substituted pentacenes.

The HOMO and LUMO energy levels are plotted in **Figure 5.5** for easy comparison. A closer look at the cyanopentacenes (compounds **1-6; Figure 5.5(a)**) shows many interesting trends. For instance, no significant differences in energy levels were observed between any of the dicyano-substituted pentacenes (compounds **2-5**), indicating that energy levels are not altered by the various trialkylsilylethynyl (TIPS, TIBS, TCPS, TCHS respectively for compounds **2-5,** see **Figure 5.2**) substitutions. On the other hand, the sequential addition of nitrile groups to the pentacene core (one nitrile group for compound **1**, two groups for compounds **2-5**, and four groups for compound **6**) progressively depressed both the LUMO and HOMO of the material. Neither the number of nitrile groups on the

acene core nor changes in the trialkylsilyl group yield significant changes in the HOMO-LUMO gap of the pentacene. More importantly, all the pentacenes form type II semiconductor heterojunctions with P3HT, indicating their viability as acceptors.

A comparison of the mono-substituted pentacenes (compounds **1, 7-13**; **Figure 5.5(b)**) shows slight variations in energy levels. As expected, the strongly electron-withdrawing nitro substituent (compounds **10** and **11**) gave rise to the lowest lying LUMO level, followed by nitrile (compound **1**) and carboxymethyl (compound **12**) substituents. Only small differences exist in the LUMO energies between pentacenes substituted on the 1-position versus those substituted on the 2-position with the same functional group (compounds **7** and **8**, and compounds **10** and **11**).

Several of the pentacenes yielded crystals of sufficient quality for at least cursory structural analysis by single-crystal X-ray diffraction, performed by Dr. Sean Parkin at the University of Kentucky. Two of the most common crystal packing motifs for acenes used as organic semiconductors are the edge to face "herringbone" arrangement, and the face to face π-stacking arrangement.[153] Trialkylsilylethynyl substitution on acenes generally yields 1-D and 2-D π-stacked arrays.[154, 155] Among these pentacene derivatives, a common motif was a 1-D "slipped-stack" (**Figure 5.6 (b)**) arrangement adopted by compounds **6**, **8**, and **9**. The resulting pairwise-stacked acenes are insulated from adjacent stacks by the substituents of those stacks. Another common motif is the 1-D "sandwich-herringbone" (**Figure 5.6 (c)**) structure adopted by compounds **1, 4**, and **5**. In this structure, two adjacent pentacene molecules π-stacked closely together in a "sandwich", and these sandwiches then stack edge to face in a "herringbone" arrangement. Compounds **2, 3**, and **11** adopted a 2-D "brickwork" (**Figure 5.6(a)**) packing similar to that of TIPS pentacene (compound **14**).[156] Compounds **7**, **10, 12**

and **13** formed crystals that were of poor quality or were too small for analysis by single crystal x-ray diffraction.

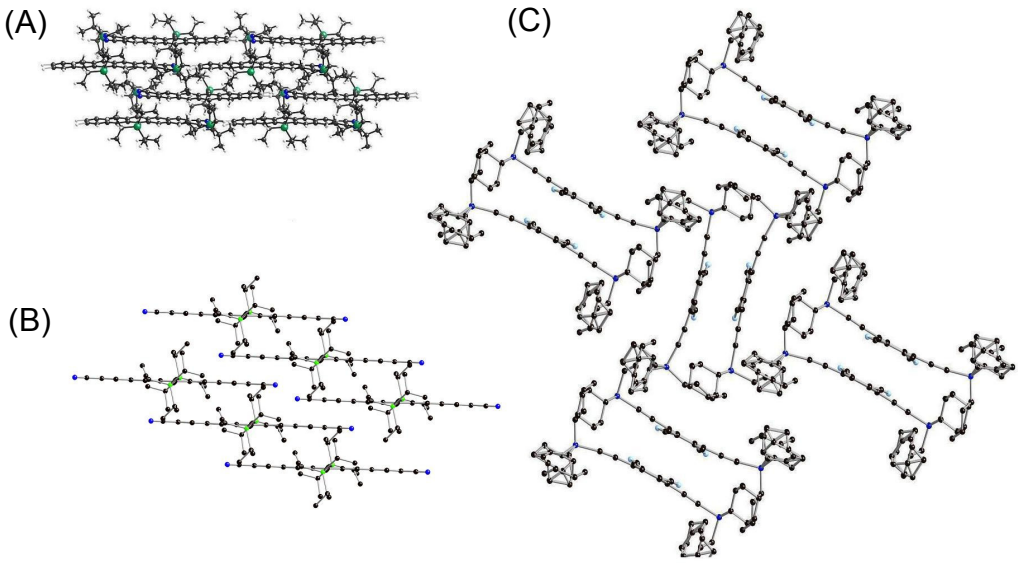

Figure 5.6 Crystal packing motifs of the pentacenes: (a) 2-D "brickwork" (b) 1-D "slipped-stack" (c) 1-D "sandwich-herringbone".

Solar cells were fabricated on pre-patterned ITO coated glass substrates, which were cleaned by sonication in a mild detergent, rinsed in de-ionized water, dried in a nitrogen stream, and treated with a 10-minute UV-ozone exposure. PEDOT:PSS was filtered through a 0.45 μm PVDF syringe filter, and then deposited by spin-coating at 6000 rpm for 60 seconds. The PEDOT:PSS layer was baked on a hot-plate at 170 °C for 4 minutes to remove residual solvent. The samples were then transferred into a nitrogen-filled glovebox, in which all subsequent processing steps were carried out. P3HT and pentacene acceptor were dissolved in toluene or a toluene/dichlorobenzene solvent mixture at a 1:1 ratio to give a total concentration of 20 mg/ml. The semiconductors were applied by spin-coating on top of the PEDOT:PSS layer at 1000 rpm for 60 seconds. Finally, 4 Å of CsF and 400 Å of Al were thermally evaporated

under high vacuum (~10^{-6} Torr) to form the cathode for the devices. A shadow mask was used in the evaporation to define a device active area of 3 mm^2. A schematic of the device stack is shown in **Figure 5.7**.

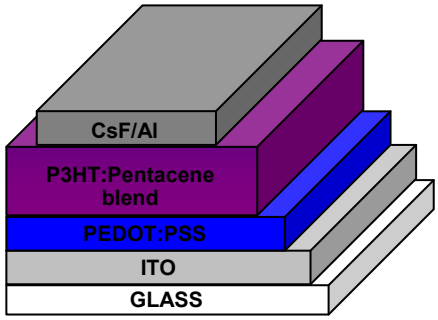

Figure 5.7 Schematic of the solar cell device stack.

Solar cell current-voltage (I-V) curves were obtained with a Keithley 236 source-measurement-unit (SMU) under AM 1.5 100 mW/cm^2 illumination from a Solar Light 16S-002 solar simulator. Light output power was calibrated using a Newport 818P-010-12 thermopile high power detector, which has a flat response over a broad spectral range. Spectral mismatch was not taken into account in these measurements. In general, 4-5 devices were tested per acceptor, and values reported here are averaged over these devices.

Film morphology was investigated using tapping mode atomic force microscopy (AFM) as well as optical microscopy. AFM images were taken with a Digital Instruments Dimension 3100 Atomic Force Microscope, with a scan area of 5 μm by 5 μm. Optical microscopy was done using an Olympus MX50 optical microscope equipped with a high-resolution digital camera. In order to study the spectral response of the solar cells, external quantum efficiency (EQE) spectra were measured for the best performing cells. This was done using a Newport 1000 W xenon lamp coupled to an Oriel Cornerstone 260 ¼ m monochromator as the light source, a

Keithley 236 SMU to measure short circuit current, and a Newport 918D-UV3-OD3 low power detector to monitor the light intensity. The EQE data was compared to UV-Vis absorption spectra obtained using a Shimadzu UV-3101PC UV/Vis/Near-IR Spectrophotometer.

Results and Discussion

Initial studies of solar cell performance were done with the cyanopentacenes to investigate the effects of number of electron-withdrawing groups as well as the trialkylsilylethynyl solubilizing group. All solar cells were fabricated with a 1:1 blend of P3HT : cyanopentacene spin-coated from pure toluene. The results are summarized in **Table 5.2**.

Table 5.2 Solar cell performance of P3HT : cyanopentacene cells.

Acceptor	Crystal packing	V_{OC} [V]	J_{SC} [mA/cm^2]	FF	PCE [%]
1	1-D "sandwich-herringbone"	0.84	2.45	0.36	0.74
2	2-D "brickwork"	0.58	0.44	0.38	0.10
3	2-D "brickwork"	0.50	0.67	0.37	0.12
4	1-D "sandwich-herringbone"	0.54	1.93	0.41	0.43
5	1-D "sandwich-herringbone"	0.60	1.16	0.38	0.26
6	1-D "slipped-stack"	0.44	0.36	0.40	0.06

The first observation was that acceptors that pack in a 1-D "sandwich-herringbone" motif (compounds **1**, **4**, and **5**) greatly out-performed the others. A comparison of compounds **2 - 5** shows that crystal packing is greatly influenced by the trialkylsilylethynyl solubilizing group. TIPS and TIBS (compounds **2** and **3**) gave rise to 2-D "brickwork" packing, while 1-D "sandwich-herringbone" was obtained

from TCPS and TCHS (compounds **4** and **5**). Optical microscopy was used to probe film morphology of these pentacene derivatives. **Figure 5.8(a)** shows a film spin-casted from a 1:1 blend of P3HT and compound **2**, showing the formation of large (~10-20 μm) crystals. In fact, the films appeared cloudy after spin-coating, due to light scattering from these crystals. Since it is desirable to have donor-acceptor domains of ~10 nm in size for efficient exciton dissociation to occur,[29] the large scale phase separation observed here is the likely cause of the low J_{SC} and PCE of these cells. Strong inter-molecular interactions due to 2-D π-stacking may be the reason for the formation of such large crystals. In contrast, a film spin-coated from a blend of P3HT and compound **4** does not exhibit large crystal formation (**Figure 5.8(b)**), probably due to weaker π-stacking interactions in the solid state. Therefore, such materials may produce a better film morphology for exciton dissociation. This general observation was noted over all of the 1-D and 2-D π-stacking materials examined in this study. Hence, similar to a previously reported result with 1-D π-stacking anthradithiophene-based donors,[157] organic solar cells show the opposite performance trend as compared to organic thin film transistors (OTFTs), for which 2-D π-stacking materials were found to give the highest transistor mobilities.[149]

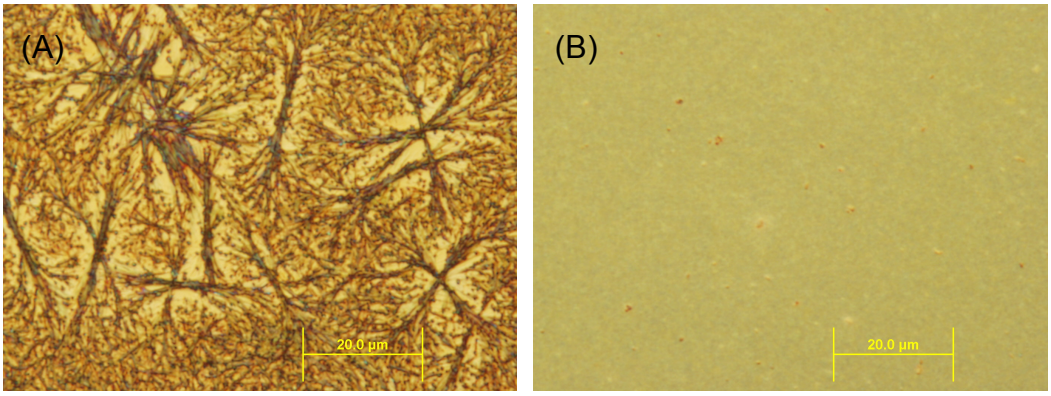

Figure 5.8 Optical microscopy images of films from (a) blend of P3HT and compound **2** (b) blend of P3HT and compound **4**.

The HOMO / LUMO energy levels of the cyanopentacenes can explain the differences in the V_{OC}. By comparing the energy levels in **Figure 5.5(a)** and the V_{OC} values in **Table 5.2**, it is clear that the V_{OC} trend is consistent with the design rules published by Scharber *et al*.,[38] which stipulate that a larger difference between the donor HOMO and the acceptor LUMO energy levels will lead to higher V_{OC} (Equation 1.3). It is thus not surprising that the highest V_{OC} of 0.84 V was obtained with compound **1** which has the highest lying LUMO at 3.50 eV. The ability to tune HOMO / LUMO energy levels of the cyanopentacenes is thus a great advantage of this family of acceptors, since it allows control of the V_{OC}. The V_{OC} value of 0.84 V also compares favorably with the V_{OC} of ~ 0.60 V for P3HT:PCBM based solar cells (**Figure 4.8(b)**).

Further device optimization was performed on compound **1**, the most promising of the cyanopentacenes. The high tendency for pentacene to crystallize and create large donor/acceptor domains suggests that suppression of pentacene crystallization during film formation can lead to improved performance. It has been shown that the addition of alkanedithiols to a solution of PCPDTBT and PCBM prior to spin-coating dramatically improved the performance of the PCPDTBT:PCBM cell.[34, 36] Alkanedithiol additives have a higher boiling point than the host solvent,[36] and subsequent work showed that the improved device performance is due to the selective dissolution of one of the blend components during the spin-casting process thus giving rise to a more optimum film morphology.[36] This inspired the idea to experiment with solvent mixtures to improve the cell performance of devices containing the pentacene acceptors. 1,2-dichlorobenzene (DCB) seems to have the appropriate combination of solvating power and high boiling point to serve as an additive for our new acceptors, and its ability to "solvent anneal" both P3HT and acene-based materials.[30, 157]

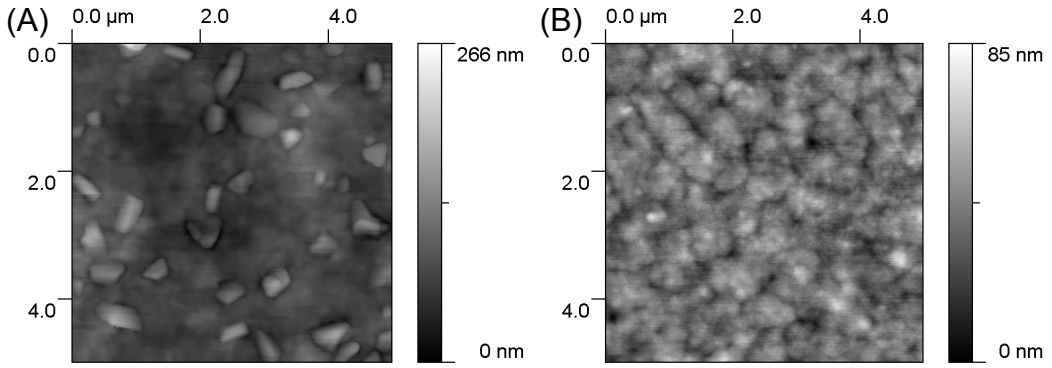

Figure 5.9 AFM images of films from blends of P3HT and compound **1** spin-casted from (a) pure toluene (b) toluene and DCB solvent mixture.

A series of comparative studies showed that a blend of P3HT and compound **1** (1:1 ratio by weight) spin-casted from a toluene/DCB solvent mixture at a 10:3 ratio by volume yielded the highest performing devices. No thermal annealing was performed on the finished devices, since this was typically found to degrade device performance. Clear morphological changes were observed by AFM as the proportion of DCB was increased (**Figure 5.9**), suggesting suppression of large crystal formation in one of the semiconductor components and a more uniform grain size. From toluene-casted films, large, coarse crystalline-looking features can be seen (**Figure 5.9(a)**), yielding an rms roughness of 22.0 nm. The film casted from a toluene/DCB mixture (**Figure 5.9(b)**) possesses finer features with a significantly lower film rms roughness (9.1 nm), suggesting more intimate contact between the donor and acceptor phases. Under these conditions, the device performance of compound **1** was improved to yield a V_{OC} of 0.84 V, J_{SC} of 3.56 mA/cm^2, FF of 0.42, and a PCE of 1.27 %. This is a significant increase in efficiency compared to the device spin-casted from pure toluene that gave just 0.74 %. Current-voltage (I-V) curves under 100 mW/cm^2 AM 1.5 illumination are plotted in **Figure 5.10** to illustrate this performance enhancement.

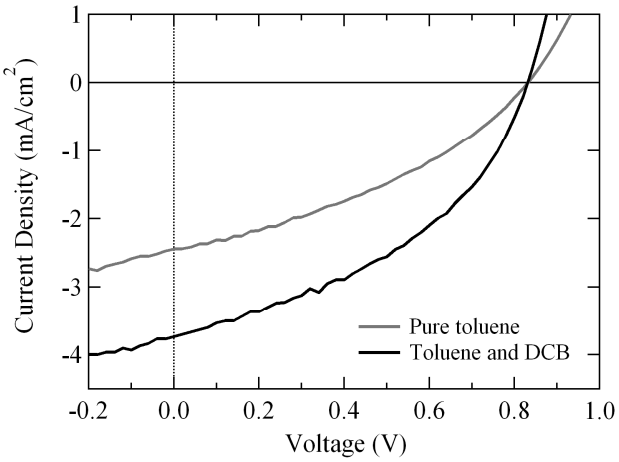

Figure 5.10 Comparison of current-voltage (I-V) curves of solar cells from a blend of P3HT and compound **1** spin-casted from pure toluene versus a toluene/DCB mixture.

Table 5.3 Solar cell performance of the mono-substituted pentacene acceptors processed with the optimized toluene/DCB mixture.

Acceptor	Crystal packing	V_{OC} [V]	J_{SC} [mA/cm^2]	FF	PCE [%]
1	1-D "sandwich-herringbone"	0.84	3.56	0.42	1.27
7	N/A	0.59	0.54	0.32	0.10
8	1-D "slipped-stack"	0.70	1.86	0.32	0.41
9	1-D "slipped-stack"	0.67	2.07	0.33	0.46
10	N/A	0.56	0.27	0.32	0.05
11	2-D "brickwork"	0.64	0.49	0.28	0.09
12	N/A	0.86	1.05	0.39	0.35
13	N/A	0.70	0.94	0.37	0.24
14	2-D "brickwork"	0.79	0.24	0.39	0.08

The success of the mono-substituted cyanopentacene inspired the synthesis of other pentacene derivatives with a single electron-withdrawing group (**Figure 5.4**). These mono-substituted pentacenes were then studied using the optimized fabrication

procedure described above, and their device performances are shown in **Table 5.3**. As before, almost all devices show higher V_{OC} than a typical P3HT:PCBM cell (V_{OC} ~ 0.6 V), which is due to the higher lying LUMO levels of the pentacene-based acceptors. It is noteworthy that even the un-substituted TIPS pentacene (compound **14**), a known high-mobility p-type semiconductor in OTFTs,[158] can function as an n-type acceptor to P3HT thus suggesting that these materials are ambipolar in nature. In general, the materials whose π-stacking motif approaches 1-D π-stacking exhibit higher J_{SC} and hence higher PCE, consistent with previous observations for the cyanopentacenes. A significant impact of the substitution pattern on the V_{OC} of the solar cells is observed. Derivatives substituted on the 1-position of the acene (compounds **7** and **10**) showed demonstrably lower V_{OC} than derivatives containing the same electron-withdrawing group at the 2-position (compounds **8** and **11**). The magnitude of this difference (in all cases > 0.05 V) is significantly greater than would be estimated from the differences in LUMO energies (on the order of 0.0 – 0.04 eV). Contributing to this phenomenon may be the very different crystallinity of the 1-substituted vs. the 2-substituted derivatives – as mentioned previously, none of the 1-substituted derivatives yielded crystals suitable for crystallographic analysis.

The nitro (NO_2) and perfluoroethyl (CF_2CF_3) groups are strongly electron-withdrawing and yielded unacceptably low V_{OC}, while the trifluoromethyl (CF_3), chloro (Cl) and carboxymethyl ($COOCH_3$) derivatives were deemed worthy of further exploration. In the cynanopentacene study, derivatives adopting a 1-D "sandwich-herringbone" crystal packing arrangement (e.g. compound **1**) yielded the highest J_{SC} in blends with P3HT. The silylethyne route to acene functionalization allows facile tuning of crystal packing by simple changes to the silane, and a number of newly synthesized derivatives were screened for this crystal packing motif. While the carboxymethyl derivative could not be altered to yield the desired crystal packing,

both the trifluoromethyl derivative **15** (requiring the TIBS substituent) and the chloro derivative **16** (requiring the TCPS substituent) did yield the desired motif (**Figure 5.11**). It is worth noting that the trifluoromethyl derivative also yielded materials with motifs not screened for OPV performance before; a simple 1-D "slipped-stack" motif (compound **17**, TCPS substituent) and an unusual "cruciform" version of this motif, where alternate pentacene units are rotated by approximately 90° relative to their neighbors in the stack (compound **18**, tri-n-propylsilyl (TNPS) derivative).

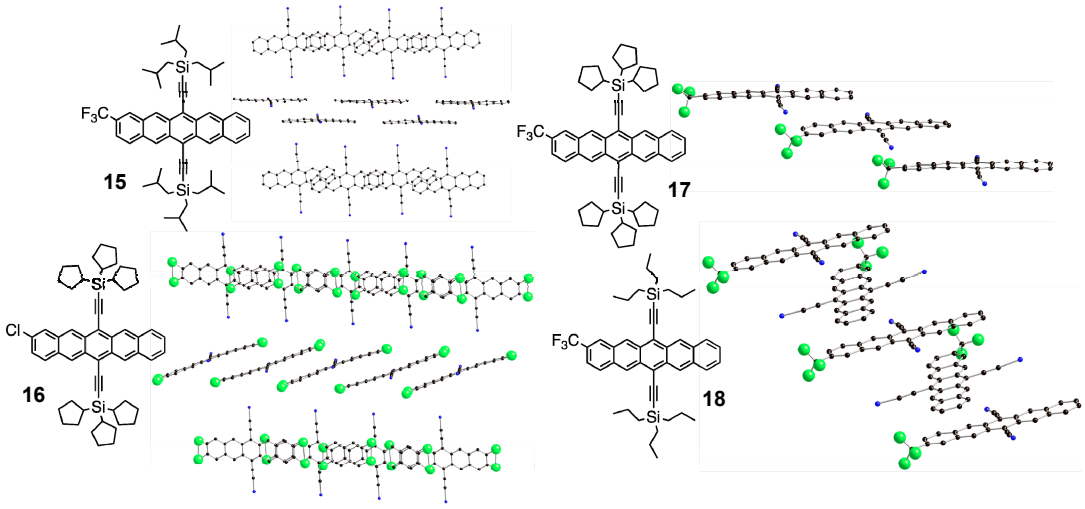

Figure 5.11 Molecular structures and crystal packing of compounds **15**-**18**.

Table 5.4 Solar cell performance of acceptors **15**-**18**.

Acceptor	Crystal packing	V_{OC} [V]	J_{SC} [mA/cm^2]	FF	PCE [%]
15	1-D "sandwich-herringbone"	0.80	3.17	0.50	1.26
16	1-D "sandwich-herringbone"	0.95	2.44	0.43	1.00
17	1-D "slipped-stack"	0.78	3.23	0.33	0.83
18	1-D "slipped-stack"	0.62	1.05	0.27	0.18

Solar cell performances of these compounds are shown in **Table 5.4**. Once again, it is observed that materials adopting a 1-D "sandwich-herringbone" crystal packing arrangement (compounds **1, 15, 16**) yield the highest device currents and fill-factors. The requirement of a strongly one-dimensional packing motif for best performance is further supported by the high performance of compound **17**, which, although not adopting the sandwich herringbone motif, still packs in a 1-D "slipped-stack" arrangement.

As a preliminary study of the stability of these new materials, their operational performance was characterized after exposure to ambient air alongside that of a traditional P3HT / PCBM device fabricated at the same time. The power conversion efficiency (PCE) is plotted over time in **Figure 5.12** as a fraction of the initial PCE before air exposure. The device lifetime of pentacene-based materials was comparable to that of the simultaneously measured PCBM-based device, with the perfluoroethyl (CF_2CF_3) derivative (compound **9**) showing the greatest stability.

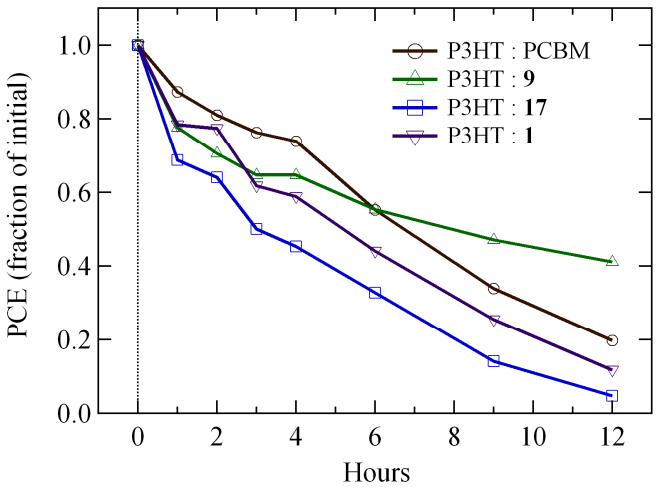

Figure 5.12 Comparison of device lifetimes of pentacene-based vs. PCBM-based solar cells.

To investigate the spectral response of these acceptors, the EQE spectrum of the best acceptor (compound **1)** in a blend with P3HT was acquired (**Figure 5.13(a)**). The peak EQE is above 25% at around 500 nm for this device, corresponding to the peak absorption of P3HT (**Figure 5.14**). The smaller peaks at around 330 nm and 670 nm correspond to the absorption peaks of compound **1** (**Figure 5.14**), showing that it too is contributing to the generation of photocurrent outside the absorption window of P3HT, hence extending the spectral response of the P3HT solar cell. For comparison with PCBM, normalized EQE spectra are plotted in **Figure 5.13(b)**. It clearly shows that the pentacene-based cell has a photo-response that goes further into the red than the PCBM-based cell, hence capturing a larger fraction of the solar spectrum.

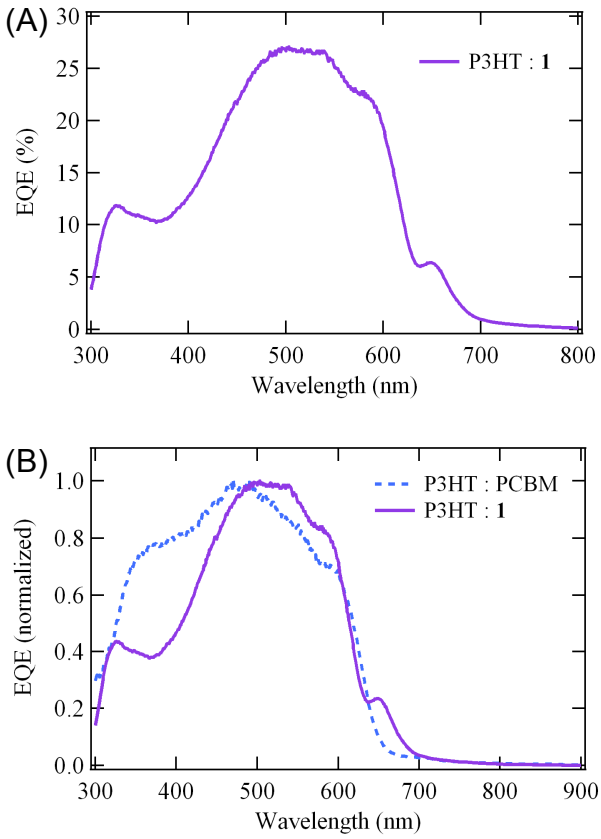

Figure 5.13 (a) EQE spectrum of a cell from a blend of P3HT and compound **1** (b) normalized EQE spectra comparison between P3HT : PCBM and P3HT : **1**.

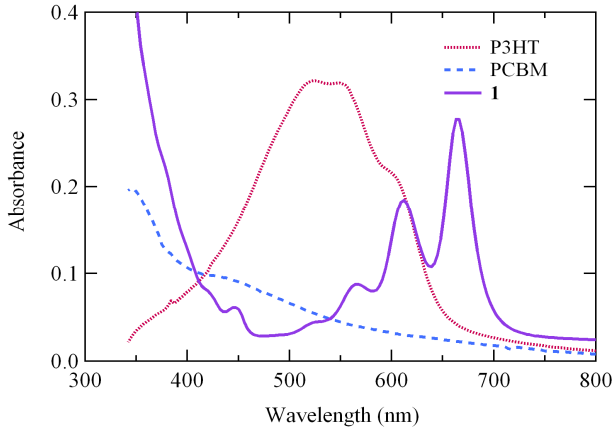

Figure 5.14 UV-Visible absorption spectra of P3HT, PCBM and compound **1**.

Conclusion

A wide variety of silylethyne-substituted pentacene derivatives have successfully served as effective acceptors in P3HT-based bulk-heterojunction solar cells. An improved fabrication procedure was used that exploits solvent mixtures to yield better film morphology. The nature, position and number of electron-withdrawing groups substituted onto the pentacene core were all found to impact the device V_{OC}. The electron-deficient pentacene acceptors led to devices with voltages higher than typically observed with PCBM acceptor. After determining the substituents yielding the best voltage, optimization of the acceptor crystal packing by changing the alkyl groups on the silyl substituent led to improvements in device J_{SC}, yielding three new acceptors all with power conversion efficiency > 1.0 %. The best derivatives, cyano (CN) substituted compound **1** and trifluoromethyl (CF_3) substituted compound **15**, had PCE > 1.2%. The wide array of pentacene derivatives that yielded efficient solar cells, along with the ease with which new derivatives can be prepared, make these pentacenes a versatile platform for the development of structure-property relationships for organic photovoltaic acceptors.

CHAPTER 6

ACENE ACCEPTORS FOR IMPROVED RESPONSE TO THE SOLAR SPECTRUM

Abstract

Electron-deficient pentacenes were shown to be efficient acceptors for polymer solar cells. In this work, two more acene families, namely hexacenes and anthradithiophenes, are investigated as solar cell acceptors. The strategy of attaching electron withdrawing substituents to the acene backbone once again proved successful in converting the previously p-type acenes into acceptors. The hexacenes are shown to extend the spectral response of P3HT-based solar cells to about 800 nm, which is further into the infra-red than what the pentacene acceptors are capable of. Anthradithiophenes, on the other hand, possess a high-lying LUMO, giving rise to V_{OC} approaching 1.1 volts and PCE of 0.8 % when used as acceptors to P3HT. They also show light absorption up to about 600 nm, and can potentially complement the absorption spectra of emerging low band-gap polymers.

Introduction

In the previous chapter, detailed reasons were given for the need to explore alternative acceptors to fullerenes for organic solar cells, and will not be repeated here. Electron-deficient pentacenes were shown to be fairly successful as acceptors, achieving efficiencies in excess of 1.2 %. Being of lower band-gap than P3HT, they extended the spectral response of P3HT-based solar cells to about 700 nm (**Figure 5.14**).

In order to further extend the spectral response, it makes sense to explore acceptors with even lower band-gaps. Since electrons in organic semiconductors can

be modeled as particles in a box (see Chapter 1), extending the orbital delocalization by going to a higher acene like hexacene is the obvious step to reduce the band-gap. The band-gap of hexacene is 1.6 eV,[159] as compared to 1.9 eV for pentacene.[21] While electronic devices based on pentacene and the smaller acenes like anthracene and tetrecene have been widely studied,[149] no device studies based on hexacene has been reported, which is likely due to its poor stability.[159] Recently, Payne *et al.* has shown that attachment of trialkylsilylethnyl groups to the hexacene core not only imparts solubility to the molecule but also makes it stable enough to be studied in solution.[159]

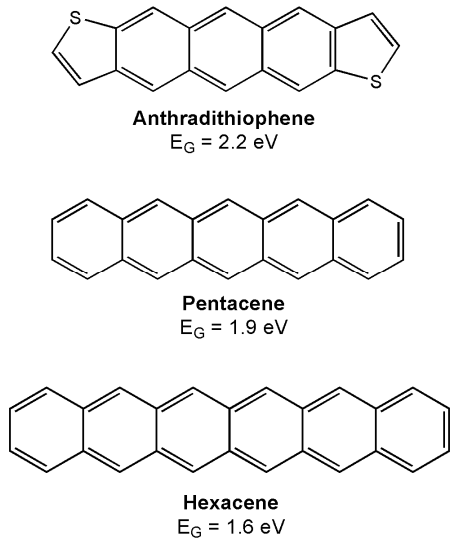

Figure 6.1 Molecular structures and band-gaps of anthradithiophene, pentacene, and hexacene.

In comparison, anthradithiophene (ADT) is a lot more stable and has been investigated extensively for applications in organic thin film transistors[160, 161] (OTFTs) as well as in solar cells.[157] An OTFT based on a spin-coated film of a soluble derivative, 2,8-difluoro-5,11-bis(triethylsilylethynyl) anthradithiophene (diF-TESADT), achieved a carrier mobility of 1.5 cm^2/Vs,[160] while a transistor based on a

single-crystal of the same material gave a mobility as high as 6 cm^2/Vs.[161] The rather large 2.2 eV band-gap of ADT[157] implies limited absorption of the solar spectrum when used in solar cells, but also means that larger V_{OC} is possible (see Equation 1.3). A solar cell based on the ADT derivative 2,8-diethyl-5,11-bis(triethylsilylethynyl) anthradithiophene (ethyl-TES-ADT) as the donor and PCBM as the acceptor achieved a V_{OC} of 0.84 V and a PCE of 1.0 %.[157]

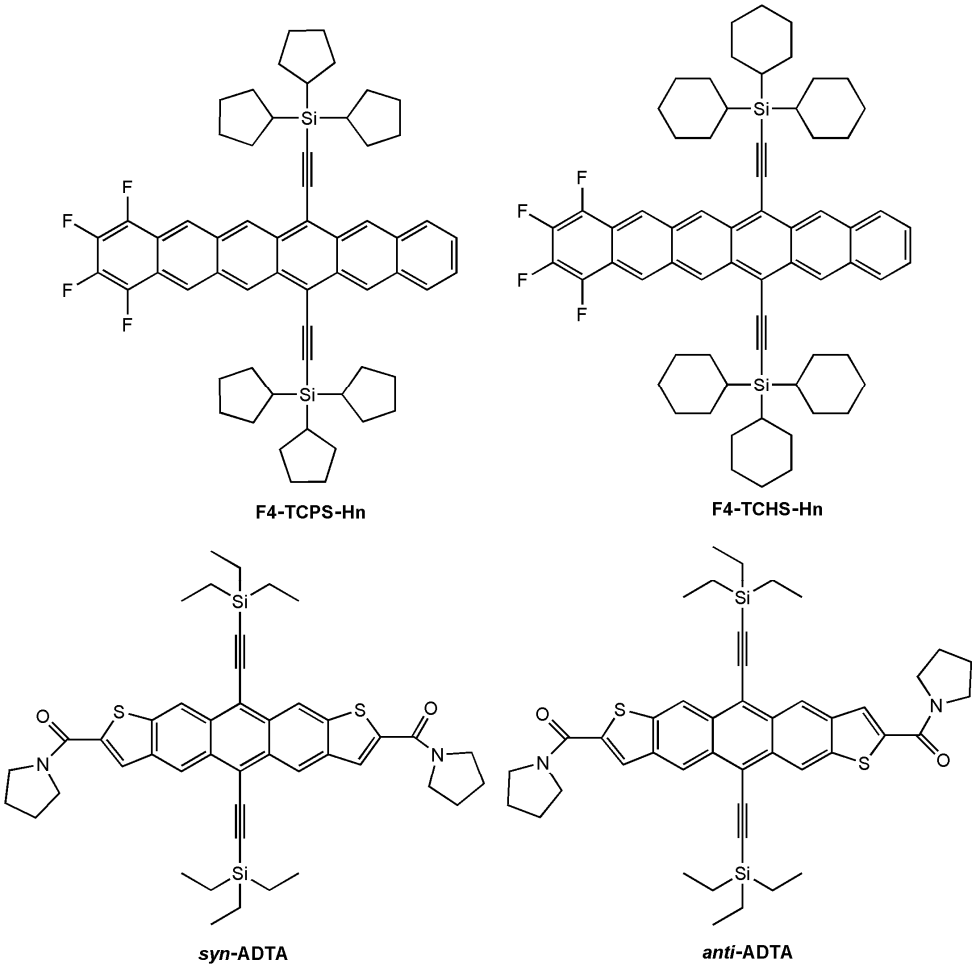

Figure 6.2 Molecular structures of hexacene and ADT acceptors investigated in this work.

In this work, two hexacene and two ADT derivatives are investigated as acceptors to P3HT, as shown in **Figure 6.2**. Fluorination of the backbone of an

organic semiconductor, CuPc, led to a dramatic increase in stability.[162] The partially fluorinated hexacenes, tetrafluoro-7,14-tricyclopentylsilylethynyl-hexacene (**F4-TCPS-Hn**) and tetrafluoro-7,14-tricyclohexylsilylethynyl-hexacene (**F4-TCHS-Hn**), are thus expected to exhibit similar improved stability. Meanwhile, the ADT acceptors are functionalized with a triethylsilylethynyl (TES) solubilizing group and an amide electron-withdrawing (pyrrolidine) group. ADTs are usually prepared and studied as inseparable mixtures of the *syn* and *anti* regioisomers. Therefore, the precursors of amide functionalized ADTs (**ADTA**s) in this study, including ADT quinone, dibromide, dicarboxylic acid and diacid chloride, were only accessible as mixtures. The as-synthesized amide (***mix*-ADTA**) was also a mixture showing no sign of isomer separation on silica thin film chromatography. However, it was noticed that in certain solvents, such as toluene and chlorobenzene, ***syn*-** and ***anti*-ADTA**s crystallized independently out of the isomer mixture to form distinct crystals. Thus, gram-scale isomerically-pure **ADTA**s can be easily obtained using a simple, scalable fractional crystallization process.

Experimental

Hexacene and isomerically-pure ADTA acceptors were synthesized by Balaji Purushothaman and Dr. Zhong Li respectively from the Anthony group at University of Kentucky. They also performed the electrochemical studies, while Dr. Sean Parkin from the University of Kentucky did the single crystal x-ray diffraction to determine crystal packing.

HOMO / LUMO energy levels of the acceptors were obtained by electrochemical analysis, performed on a BASi Epsilon potentiostat. The experiments were done under a stream of nitrogen in a 0.1 M solution of tetra-*n*butylammonium hexafluorophosphate as a supporting electrolyte in anhydrous *o*-dichlorobenzene. The

experiments were carried out using platinum electrodes at a scan rate of 100 mV/s against Ag wire as a pseudoreference electrode at room temperature. Ferrocene was used as a reference oxidation potential. Calculated HOMO / LUMO energy levels are shown in **Figure 6.3**. Similarly to the pentacene acceptors, a change in the solubilizing group from TCPS to TCHS has little effect on the HOMO and LUMO levels of the hexacenes. The two isomers of the ADTA also have virtually identical energy levels.

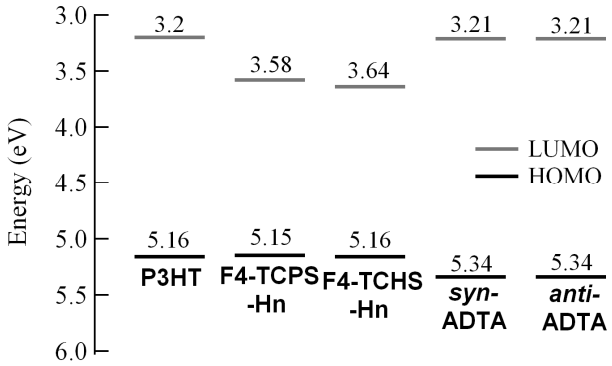

Figure 6.3 HOMO and LUMO energy levels calculated from electrochemical data.

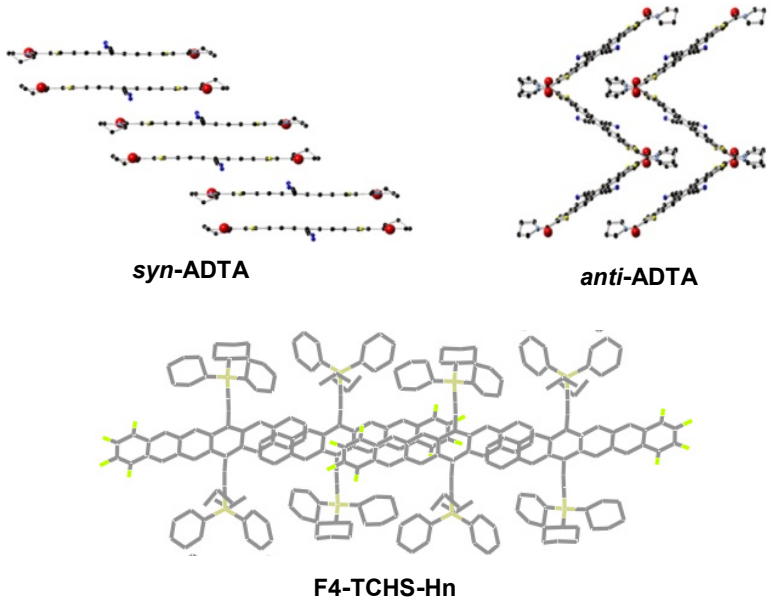

Figure 6.4 Crystal packing of the hexacenes and ADTAs.

On the other hand, there are significant differences in the crystal packing (**Figure 6.4**). **F4-TCHS-Hn** exhibits a 1-D π-stacking arrangement, while **F4-TCPS-Hn** does not yield crystals of sufficient quality for single-crystal x-ray diffraction analysis. In the case of ***syn*-ADTA**, there are two asymmetric units per unit cell, which contains two ADTA molecules and two toluene molecules. The two ADTA molecules are related by an inversion center with strong π-π interaction (~ 3.4 Å) and opposing dipole moments, resulting in a strong 1-D π-π stacking motif. However, ***anti*-ADTA** forms twin-crystals which do not contain any solvent molecules. A herringbone packing motif was observed, with no π-π interactions between molecules within stacks because of the complete facial offset of adjacent ADT core. This suggests that charge transport and hence device performance will be poor for ***anti*-ADTA.**

Solar cells were fabricated on pre-patterned ITO coated glass substrates, which were cleaned by sonication in a mild detergent, rinsed in de-ionized water, dried in a nitrogen stream, and treated with a 10-minute UV-ozone exposure. PEDOT:PSS was filtered through a 0.45 μm PVDF syringe filter, and then deposited by spin-coating at 6000 rpm for 60 seconds. The PEDOT:PSS layer was baked on a hot-plate at 170 °C for 4 minutes to remove residual solvent. The samples were then transferred into a nitrogen-filled glovebox, in which all subsequent processing steps were carried out. For hexacene cells, P3HT and hexacene were dissolved in toluene at a ratio of 1:1 by weight to give a total concentration of 20 mg/ml. For ADTA cells, P3HT and ADTA were dissolved in toluene at a weight ratio of 1:0.6 to give a total concentration of 16 mg/ml. The solutions were stirred thoroughly before being spin-coated on top of the PEDOT:PSS layer at 1000 rpm for 60 seconds. Finally, 4 Å of CsF and 400 Å of Al were thermally evaporated under high vacuum (~10^{-6} Torr) to form the cathode for the devices. A shadow mask was used in the evaporation to define a device active area of 3 mm^2.

Solar cell current-voltage (I-V) curves were obtained with a Keithley 236 source-measurement-unit (SMU) under AM 1.5 100 mW/cm^2 illumination from a Solar Light 16S-002 solar simulator. Light output power was calibrated using a Newport 818P-010-12 thermopile high power detector, which has a flat response over a broad spectral range. Spectral mismatch was not taken into account in these measurements. In general, 4-5 devices were tested per acceptor, and values reported here are averaged over these devices. In order to study the spectral response of the solar cells, external quantum efficiency (EQE) spectra were measured for the best performing cells. This was done using a Newport 1000 W xenon lamp coupled to an Oriel Cornerstone 260 ¼ m monochromator as the light source, a Keithley 236 SMU to measure short circuit current, and a Newport 918D-UV3-OD3 low power detector to monitor the light intensity. The EQE data was compared to UV-Vis absorption spectra of thin films of the acceptors (**Figure 6.5**), obtained using a Shimadzu UV-3101PC UV/Vis/Near-IR Spectrophotometer.

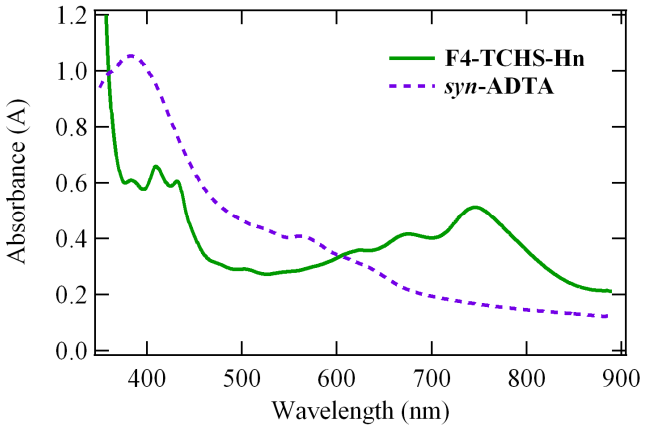

Figure 6.5 UV-Vis absorption spectra of thin films of the hexacene and ADTA acceptors.

Results and Discussion

UV-Vis absorption spectra of thin films of the acceptors are shown in **Figure 6.5**. As to be expected from the low hexacene band-gap (1.6 eV), the hexacene acceptor exhibits significant absorption up to around 800 nm. The higher band-gap (2.1 eV) of ADTA means that it does not absorb much beyond 600 nm. However, it can potentially be used as an acceptor to the emerging high-performance low band-gap polymers which typically have poor absorption in the 400-500 nm wavelength range.[35, 41] The absorption of the ADTA will therefore complement nicely the absorption spectra of these low band-gap polymers.

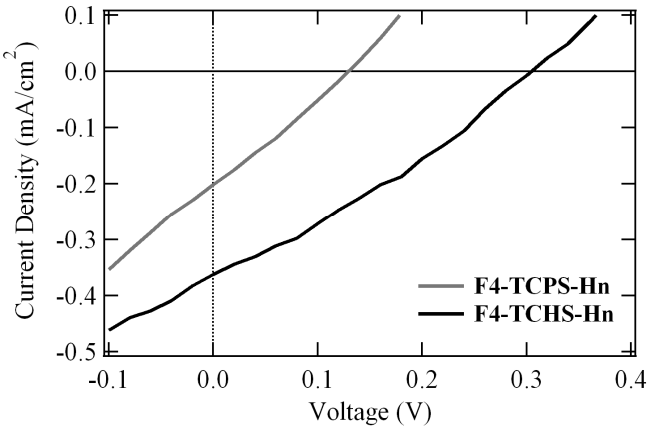

Figure 6.6 Current voltage curves of P3HT : hexacene blend cells under AM 1.5 100 mW/cm^2 illumination.

Table 6.1 Solar cell performance of hexacene acceptors.

Acceptor	V_{OC} [V]	J_{SC} [mA/cm^2]	FF	PCE [%]
F4-TCPS-Hn	0.11	0.20	0.28	0.006
F4-TCHS-Hn	0.30	0.33	0.30	0.030

The current-voltage curves of P3HT : hexacene blend cells are plotted in **Figure 6.6**, while their performance is summarized in **Table 6.1**. It is noteworthy that

these are the first devices that have been fabricated from hexacene. The devices show minimal degradation (less than 5 %) in efficiency after light exposure for 5 minutes, thus validating that the fluorination approach to improving stability. The better performance of the TCHS derivative is probably due to superior crystal packing.

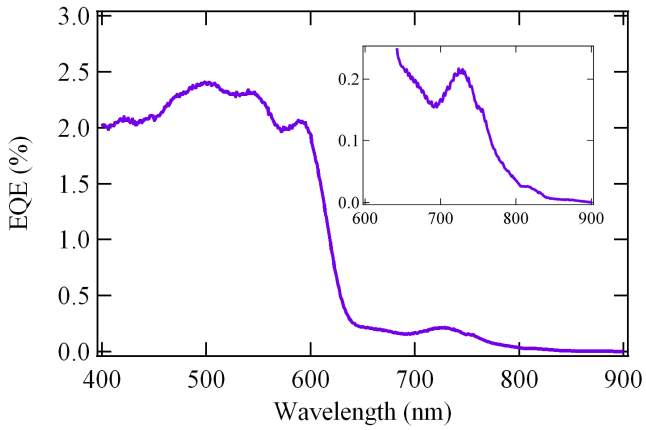

Figure 6.7 EQE of P3HT : **F4-TCHS-Hn** blend cells. Inset shows a close-up of the plot near the absorption edge of the hexacene.

A plot of the external quantum efficiency (EQE) of the best hexacene cell is shown in **Figure 6.7**. While the peak EQE at 500 nm corresponds to P3HT absorption (**Figure 5.14**), there is clearly photocurrent up to about 800 nm which corresponds to the absorption edge of the hexacene (**Figure 6.5**). Thus, even though the efficiency is not spectacular, the hexacene definitely contributes to the photocurrent and is effective at extending the spectral response of P3HT cells even further into the infra-red than pentacene acceptors (**Figure 5.13**). Further improvements in crystal packing and / or material stability may lead to better performance.

Solar cell performance of the P3HT : ADTA blend cells are summarized in **Table 6.2**. In most literature work, ADT derivatives were studied as syn/anti mixtures due to the great challenge in the preparation of isomerically pure materials. Although excellent device properties were still achieved,[161] the impact of isomeric impurity on

materials properties remains unclear. From **Table 6.2**, it is clear that solar cells based on ***syn*-, *mix*-** and ***anti*-ADTAs** demonstrated performance differences based on isomer and isomer purity. The performance expected from the crystal structures was mirrored by the devices; compared to the barely functioning devices based on ***anti*-** isomer, ***syn*-ADTA** yielded much better cell efficiency up to 0.8 %. Furthermore, ***mix*-ADTA**, the as-synthesized isomer mixture, yielded device performance intermediate between the two pure isomers. Most likely, when this statistical mixture was used without purification, ***anti*-ADTA** behaved as an essentially inactive impurity, forming poorly-functioning crystalline domains that simply degraded the cell performance set by ***syn*-ADTA**. Finally, device performance is enhanced after a brief (120 °C for 1 minute) post-fabrication thermal annealing, which is a processing advantage for the ADTA acceptors as compared to pentacenes or hexacenes which suffer performance degradation with thermal treatment.

Table 6.2 Solar cell performance of ADTA acceptors.

Acceptor	V_{OC} [V]	J_{SC} [mA/cm^2]	FF	PCE [%]
As fabricated				
***syn*-ADTA**	0.88	1.31	0.31	0.36
***mix*-ADTA**	0.59	0.72	0.29	0.13
***anti*-ADTA**	0.06	0.30	0.25	0.004
After brief thermal annealing (120 °C for 1 minute)				
***syn*-ADTA**	1.05	1.93	0.39	0.80
***mix*-ADTA**	0.59	0.55	0.28	0.09
***anti*-ADTA**	0.10	0.30	0.26	0.008

The V_{OC} of the best device based on ***syn*-ADTA** (1.05 V) is one of the highest reported for P3HT-based solar cells. This is to be expected due to the high-lying LUMO (3.21 eV) of ADTA (**Figure 6.3**). In fact, the measured LUMO of ADTA is

almost the same as that of P3HT. The P3HT LUMO value indicated here is just an estimate based on optical data and not actually calculated from electrochemistry, hence the LUMO offset between P3HT and ADTA may be greater than indicated. Nevertheless, it is a concern since it was assumed that a minimum LUMO offset of 0.3 eV is necessary for efficient electron transfer.[38] However, a recent report demonstrated an efficient (1.7 % PCE) solar cell with a LUMO offset of just 0.1 eV,[163] thus the minimum required offset may be smaller than previously believed.

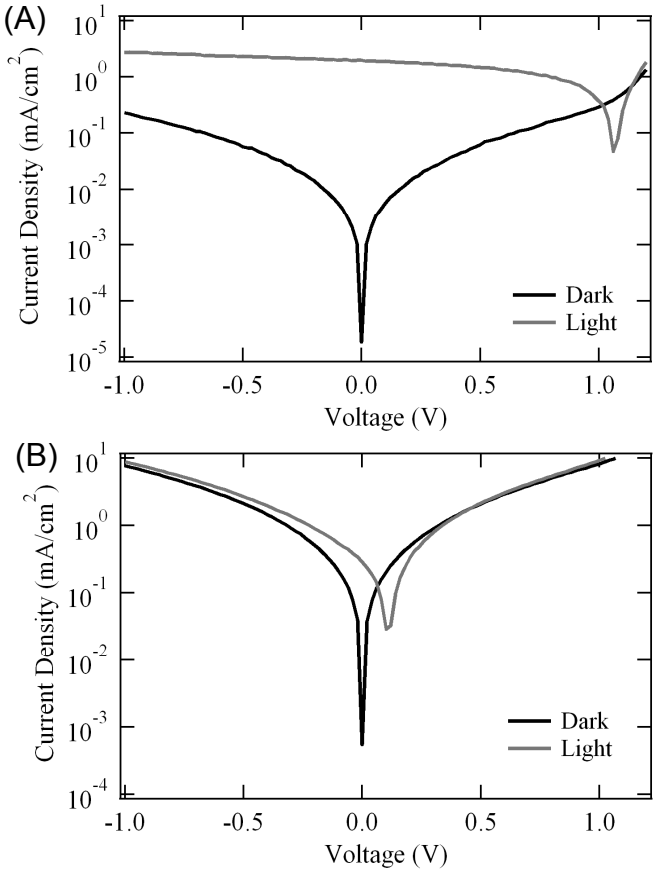

Figure 6.8 Current-voltage curves in the dark and light (AM 1.5 100 mW/cm^2) of solar cells from a blend of P3HT and (a) ***syn*-ADTA** (b) ***anti*-ADTA**.

It is also worth noting that there is huge contrast in the V_{OC} of these test cells. The identical LUMO energies of the two isomers makes this difference unusual, since

V_{OC} is typically estimated based on the energy offset between the HOMO of donor and the LUMO of acceptor (Equation 1.3). However, other factors also contribute to V_{OC}, as demonstrated by a more sophisticated equation derived by Kippelen and co-workers:[164]

$$V_{OC} \approx n\frac{kT}{e}\ln\left\{1+\frac{J_{SC}}{J_0}\right\} \quad \text{(Equation 6.1)}$$

where n is the diode ideality factor, k is Boltzmann's constant, T is temperature, e is the charge of an electron, J_{SC} is the short circuit current, and J_0 is the dark current at large reverse bias. From Equation 6.1, it is clear that a larger dark current leads to smaller V_{OC}. Current voltage curves of the P3HT : ADTA cells are plotted in **Figure 6.8**, both in the dark and under AM 1.5 100 mW/cm^2 illumination. It is clear that the dark current for ***anti*-ADTA** is about an order of magnitude larger than that for ***syn*-ADTA**, thus resulting in a much smaller V_{OC} for the former. The larger dark current for ***anti*-ADTA** is likely due to poor film quality resulting in leakage current through the pin-holes in the film.

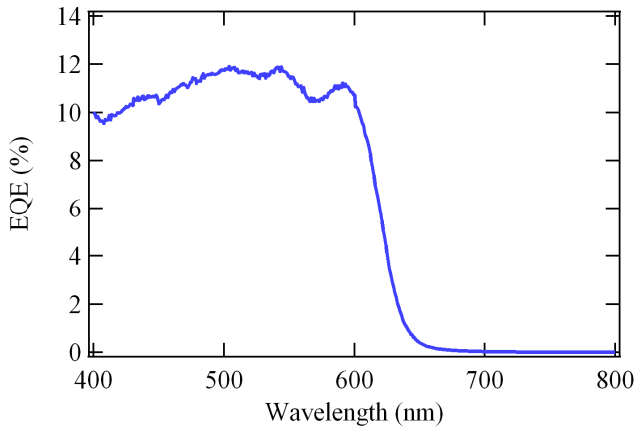

Figure 6.9 EQE spectrum of P3HT : ***syn*-ADTA** solar cell.

The EQE of the best P3HT : ***syn*-ADTA** solar cell is plotted in **Figure 6.9**. The peak value is around 12 % at wavelengths of 500 nm and 550 nm. Since the absorption spectra of P3HT and ADTA (**Figures 5.14** and **6.5**) are somewhat similar, it is difficult to determine for certain if the ADTA is contributing to the photocurrent. However, the 0.2 eV HOMO offset (**Figure 6.3**) means that hole transfer from the ADTA to P3HT is energetically favorable, thus ADTA is expected to contribute significantly.

Conclusion

The first device based on hexacene is demonstrated, exploiting the improvement in stability from partial fluorination of the hexacene core. EQE of solar cells from a blend of P3HT and hexacene acceptor show photocurrent at 800 nm, way beyond the absorption edge of P3HT and proved that the hexacenes are effective at extending the spectral response of P3HT cells. In addition, it has been successfully demonstrated that the introduction of amide groups has converted p-type anthradithiophenes into electron-deficient materials that can be used as novel acceptors in polymer solar cells. Furthermore, it produced differential self-assembly of the ***syn-*** and ***anti-*** isomers that allowed for the first time the separation and property evaluation of isomerically pure ADTs. This class of amide functionalized ADT acceptors features high V_{OC} approaching 1.1 volts in P3HT based solar cell with PCE of 0.8 %.

CHAPTER 7

COPPER OXIDE NANOCRYSTALS FOR LIGHT-HARVESTING APPLICATIONS

Abstract

Earth abundant, non-toxic and low band-gap materials like copper (I) oxide (Cu_2O) and copper (II) oxide (CuO) are attractive candidates for application in solar cells. In this work, a synthesis of CuO and Cu_2O nanocrystals (NCs) by a facile alcothermal route is reported. The nanocrystals are dispersible in common solvents, thus enabling the processing of these materials by solution. A CuO nanocrystal solar cell achieved a power conversion efficiency of 0.04 %, indicating the potential of these materials for light-harvesting applications.

Introduction

As reviewed in Chapter 1, impressive results have been achieved with nanocrystal (NC) solar cells in recent years.[11] Efficient solar cells have been reported based on CdSe, CdTe, PbS, PbSe, $CuInSe_2$ and CuZnSnSSe NCs, with PCEs as high as 7.2 % (see **Table 1.3**).

The above-mentioned materials may be good test-beds for studies of NCs as photovoltaic materials, but not of them may be feasible candidates for wide-spread deployment due to toxicity and availability. Cd and Pb are toxic heavy metals, while In and Te are among the least abundant elements in the Earth's crust.[165] It is thus desirable to explore other alternative solar cell materials. Copper and iron based semiconductors have emerged as attractive materials from an analysis by Wadia *et al.* based on abundance and cost.[166] For instance, Wu *et al.*[167] recently reported a Cu_2S

NC based solar cell with a promising PCE of 1.6 %. Copper (I) oxide (Cu_2O) and copper (II) oxide (CuO) are also attractive candidates for light-harvesting applications due to their band gap energies of 1.4 eV (indirect) for CuO[168] and 2.0 eV (direct) for Cu_2O[169] that are quite close to the ideal band-gap for a single junction photovoltaic cell estimated from detailed balance.[170] Cu_2O has been investigated as a solar cell material for several decades,[171] with recent reports of PCE up to 2.0 %.[172-174] CuO has been employed in photo-electrochemical cells[175, 176] and as a cathode for dye-sensitized solar cells.[177] The use of CuO as the active layer in solid state solar cells has, to the best of my knowledge, not yet been investigated and is the focus of this work.

Copper oxide NC syntheses via various routes have been reported in the literature.[178-193] Relatively few of these reports, however, discuss the dispersibility of their copper oxide NCs in common solvents,[190-193] which is of importance for solution-based processing of thin films. In particular, Yuhas *et al.*[192] and Hung *et al.*[193] reported solar cells based on films spin-coated from Cu_2O NC solutions, with PCE from 0.05 % to 0.14 %. In this work, the synthesis of colloidal CuO and Cu_2O NCs by a facile alcothermal method is reported. The NCs are characterized by transmission electron microscopy (TEM), X-ray diffraction (XRD), Fourier transform infrared spectroscopy (FTIR) and UV-visible absorption spectroscopy. Finally, as a proof of concept, a bi-layer solar cell based on CuO and phenyl-C_{61}-butyric acid methyl ester (PCBM) is demonstrated.

Experimental

For the synthesis of CuO NCs, 0.29 g of copper (II) acetate (Sigma Aldrich) was added to 30 ml of reagent alcohol (Sigma Aldrich) under vigorous stirring. 1 ml of de-ionized (DI) water was added, and the mixture was heated to 75 °C. In a separate

container, 1.3 ml of 25 % tetramethylammonium hydroxide (TMAH) in methanol (Sigma Aldrich) was added to 10 ml of reagent alcohol. After 15 minutes of stirring, when the copper acetate has fully dissolved, the TMAH solution was gradually added over 5 minutes in regular intervals. The reaction was allowed to proceed at 75 °C for 60 minutes, and the resultant product was collected by precipitation with hexane and then centrifuging at 3750 rpm for 5 minutes.

For the synthesis of Cu_2O NCs, 0.29 g of copper (II) acetate was added to 30 ml of reagent alcohol under vigorous stirring at 35 °C. In separate containers, 2 identical solutions of 1.3 ml of 25 % TMAH in methanol added to 5 ml of reagent alcohol were prepared, while in a third container 0.30 g glucose (Sigma Aldrich) was dissolved in 1 ml of DI water. After 15 minutes of stirring, when the copper acetate has fully dissolved, the first batch of TMAH solution was gradually added over 5 minutes. The glucose solution was then added, followed by the second batch of TMAH solution (also over 5 minutes). The mixture was heated to 65 °C, after which the reaction was allowed to proceed for 90 minutes, and the resultant product was collected by centrifuging at 3750 rpm for 5 minutes.

In order to characterize the NCs, TEM samples were prepared by drop-casting very dilute NC suspensions in methanol onto carbon grids (Electron Microscopy Sciences), and images were taken using a FEI T12 Spirit TEM. X-ray diffraction was performed on a Bruker General Area Detector Diffraction System (GADDS). A Thermo Scientific Nicolet iS10 FT-IR spectrometer was used to perform FTIR spectroscopy on NC samples that have been washed and centrifuged three times with reagent alcohol to get rid of unreacted precursors. UV-visible absorption spectroscopy was performed using a Shimadzu UV-3101PC UV/Vis/Near-IR Spectrophotometer. All film thickness measurements were done using a Tencor P10 Profilometer.

Solar cells were fabricated on pre-patterned indium tin oxide (ITO) coated glass substrates (Kintec, Hong Kong), which were cleaned by sonication in a mild detergent, rinsed in de-ionized water, dried in a nitrogen stream, and treated with a 10-minute UV-ozone exposure. CuO NCs were dissolved in a solvent mixture of 2:1 chloroform and methanol at a concentration of ~10 mg/ml, and then spin-coated on top of the ITO at 2000 rpm to give a film ~40 nm thick. A cell with a thicker CuO layer (~70 nm) was also fabricated by performing the spin-coating step 3 times. This is possible because the underlying layer is not completely dissolved during the spin-coating of subsequent layers. PCBM solution (20 mg/ml in chloroform) was then spin-coated on top of the CuO at 2000 rpm to give a film ~120 nm thick. Finally, 4 Å of CsF and 400 Å of Al were thermally evaporated under high vacuum (~10^{-6} Torr) to form the cathode for the devices. A shadow mask was used in the evaporation to define a device active area of 3 mm^2. Control PCBM only solar cells (without CuO) were also fabricated. Device current-voltage curves were obtained with a Keithley 236 source-measurement-unit (SMU) in the dark and as well as under AM 1.5 100 mW/cm^2 illumination from a Solar Light 16S-002 solar simulator. Light output power was calibrated using a Newport 818P-010-12 thermopile high power detector, which has a flat response over a broad spectral range. EQE measurements were performed using a Newport 1000 W xenon lamp coupled to an Oriel Cornerstone 260 ¼ m monochromator as the light source, a Keithley 236 SMU to measure short circuit current, and a Newport 918D-UV3-OD3 low power detector to monitor the light intensity.

Results and Discussion

The copper oxide synthesis is modified from a previously reported method for the synthesis of dispersible zinc oxide NCs.[56, 194] Copper (II) acetate, $Cu(OAc)_2$, was

dissolved in reagent alcohol and then reacted with tetramethylammonium hydroxide (TMAH) to form copper (II) hydroxide. CuO was then formed through heating:

$$Cu^{2+} + 2(OH)^{-} \rightarrow Cu(OH)_2 \quad \text{(Equation 7.1)}$$

$$Cu(OH)_2 \rightarrow CuO + H_2O \quad (T = 75\ ^\circ C) \quad \text{(Equation 7.2)}$$

To form Cu_2O (instead of CuO), the copper hydroxide was reacted with glucose as a reducing agent in the following reaction:[183]

$$2Cu(OH)_2 + C_5H_{11}O_5\text{-}CHO \rightarrow$$

$$Cu_2O + C_5H_{11}O_5COOH + 2H_2O \quad (T = 65\ ^\circ C) \quad \text{(Equation 7.3)}$$

It was observed that an excess of TMAH and mild heating (at 65 °C) were necessary conditions to drive the reaction forward.

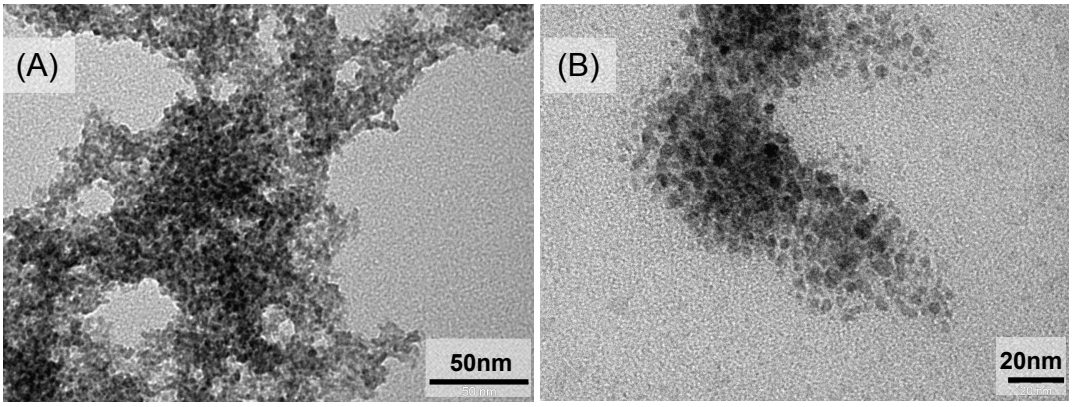

Figure 7.1 TEM images of (a) CuO NCs (b) Cu_2O NCs.

Figure 7.1 shows the TEM images of the CuO and Cu_2O NCs, in which it can be seen that they have a rather large size distribution of around 4-5 nm. The relatively broad size distribution of the colloidal Cu_xO NCs is likely the result of the nucleation and growth dynamics of the reaction. Unlike the 'hot-injection' synthesis,[53] the simplified alcothermal method lacks a single well-defined nucleation event leading to broader NC diameter distributions. X-ray diffractograms (**Figure 7.2)** of the NCs are

consistent with the literature values for CuO (JPCD# 05-0661) and Cu_2O (JPCD# 05-0667). The Cu_2O phase does not show up in the CuO synthesis and vice versa. It was observed that the addition of a small amount of de-ionized (DI) water (3 % by volume) during the CuO synthesis produced NCs with more well-defined and narrower XRD peaks as compared to NCs synthesized without water, suggesting larger particles were formed. In previously reported syntheses of ZnO nanoparticles with zinc acetate in alcohol,[195, 196] it was observed that the role of water was to increase the concentration of Zn^{2+} ions in the solution, since zinc acetate is more soluble in water than alcohol.[195, 196] Thus, it seems reasonable to arrive at the same conclusion for the CuO synthesis, that is the water promotes the forward reaction due to a higher concentration of Cu^{2+} ions in the solution.

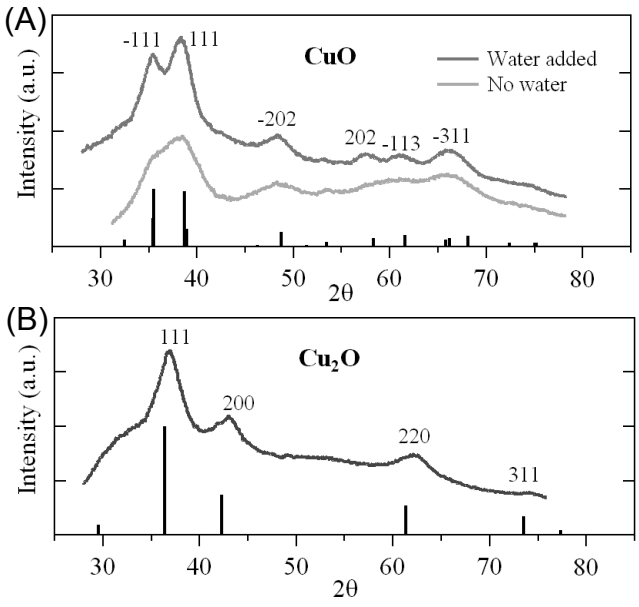

Figure 7.2 X-ray diffractograms of (a) CuO NCs, with comparison between 2 syntheses: one with water added and the other without any water. (b) Cu_2O NCs. The black lines represent literature values for CuO (JPCD# 05-0661) and Cu_2O (JPCD# 05-0667).

In order to get an estimate of the NC size, the XRD peaks are fitted to the Scherrer equation:[197]

$$t = \frac{K\lambda}{B\cos\theta_B} \qquad \text{(Equation 7.4)}$$

where t is the NC size, K is a shape factor usually taken to be 0.9, λ is the X-ray wavelength, B is the full-width (in radians) at half maximum of the peak intensity, and θ_B is the Bragg angle. The fits gave a CuO NC size of (5.1 ± 0.8) nm and a Cu_2O NC size of (4.6 ± 0.4) nm, which are consistent with the TEM images.

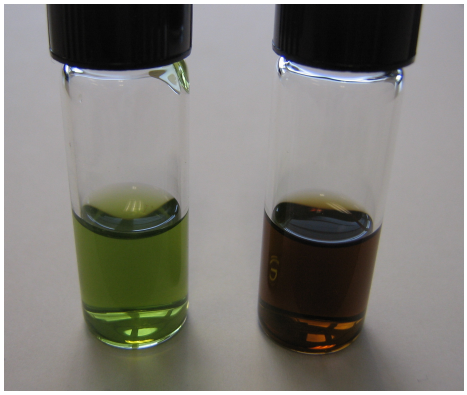

Figure 7.3 Photograph of vials of Cu_2O NC solution in water (left) and CuO NC solution in a solvent mixture of 2:1 ratio of chloroform and methanol (right).

The Cu_2O NCs are water dispersible and only slightly dispersible in organic solvents, while CuO NCs disperse well in a 2:1 solvent mixture of chloroform and methanol (**Figure 7.3**). To understand the dispersibility behavior, the NC surface chemistry was investigated using infrared spectrosocopy. FTIR spectra of the NCs were taken and shown in **Figure 7.4**. Both NCs show clear OH, CH, and CH_3 peaks. The peaks at 1560 cm^{-1} for CuO and 1600 cm^{-1} for Cu_2O are rather difficult to assign since both the water H-O-H scissoring vibration and the carboxylate anion asymmetrical stretching fall within this range,[198] but both should be represented since they are both present in the reaction. The data thus suggests that acetate (accounting for both the carboxylate and CH peaks), hydroxide and water molecules from the

synthesis are adsorbed onto the NC surfaces. The presence of both polar and organic groups explains why the CuO NCs disperse well in the chloroform and methanol mixture. On the other hand, the FTIR data for Cu_2O indicate that the polar OH (symmetrical stretching) and H-O-H (scissoring) peaks are much stronger than the organic CH and CH_3 peaks, which is consistent with the observed dispersibility of Cu_2O NCs in water.

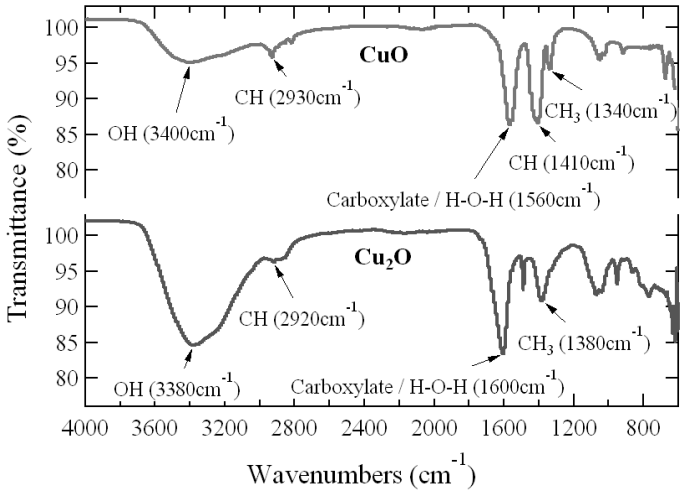

Figure 7.4 FTIR spectra of CuO (top) and Cu_2O (bottom) NCs.

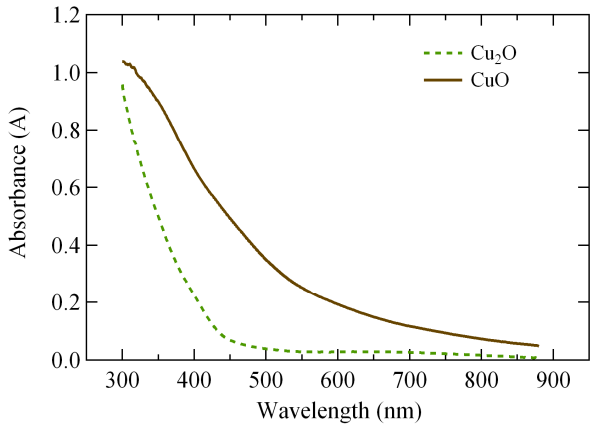

Figure 7.5 UV-Visible absorption spectra of CuO and Cu_2O NCs in solution.

Figure 7.5 shows the UV-Visible absorption spectra of the Cu_2O and CuO NCs in solution, clearly indicating the better absorption of CuO at the higher visible and IR wavelengths. The absorption spectrum of an 80 nm thick CuO film spin-coated

from solution (**Figure 7.6**) was used to calculate the absorption coefficient α of the CuO according to the formula:

$$\alpha = \frac{1}{\log_{10} e}\frac{A}{t} = 2.302\frac{A}{t} \qquad \text{(Equation 7.5)}$$

where A is the film absorbance and t is the film thickness. The absorption coefficient is plotted in **Figure 7.7**. The data indicates that CuO has a high α (defined as being greater than 10^4 cm^{-1}) for wavelengths up to ~800 nm. This compares favorably to the absorption of crystalline Si which has a high α only up to ~500 nm,[96] underlining the potential of this material for light harvesting applications.

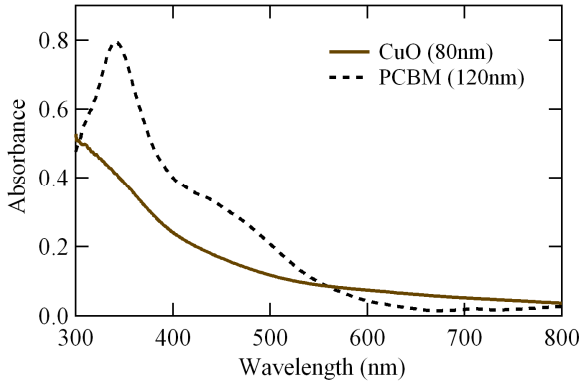

Figure 7.6 UV-Visible absorption spectra for spin-casted CuO and PCBM films.

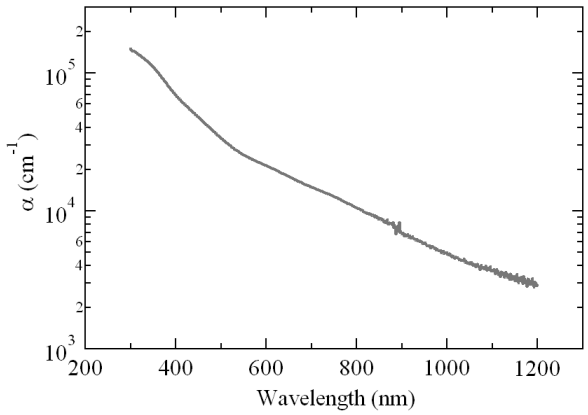

Figure 7.7 Absorption coefficient α of CuO calculated based on a spin-coated CuO NC film.

Tauc plots are generated from the absorption data to determine the direct and indirect band-gaps, which are based on the relationship:[199]

$$(\alpha E)^{\gamma} \propto (E - E_G) \qquad \text{(Equation 7.6)}$$

where α is the absorption coefficient, E is the photon energy, E_G is the material band-gap, and γ = ½ or 2 for indirect and direct band-gap respectively. Tauc plots for CuO are shown in **Figure 7.8(a)**, which indicate a direct band-gap at 3.07 eV and an indirect band-gap at 1.40 eV. The latter value is similar to the literature value for the indirect bulk band-gap.[168] While there have been reports of quantum confinement observed in CuO nanostructures,[182, 184] the authors did not perform an indirect band-gap fit to their data, hence it is difficult to make meaningful comparisons. Due to the difficulty in obtaining good quality thin films from a water-based solution, Tauc plots for Cu_2O (**Figure 7.8(b)**) are generated directly from the solution absorption data. The fit indicates a direct band-gap at 2.91 eV, which is much larger than the reported bulk value of 2.0 eV[169] but is consistent with that reported for Cu_2O nanostructures,[186, 193] suggesting that quantum confinement effects may be present.

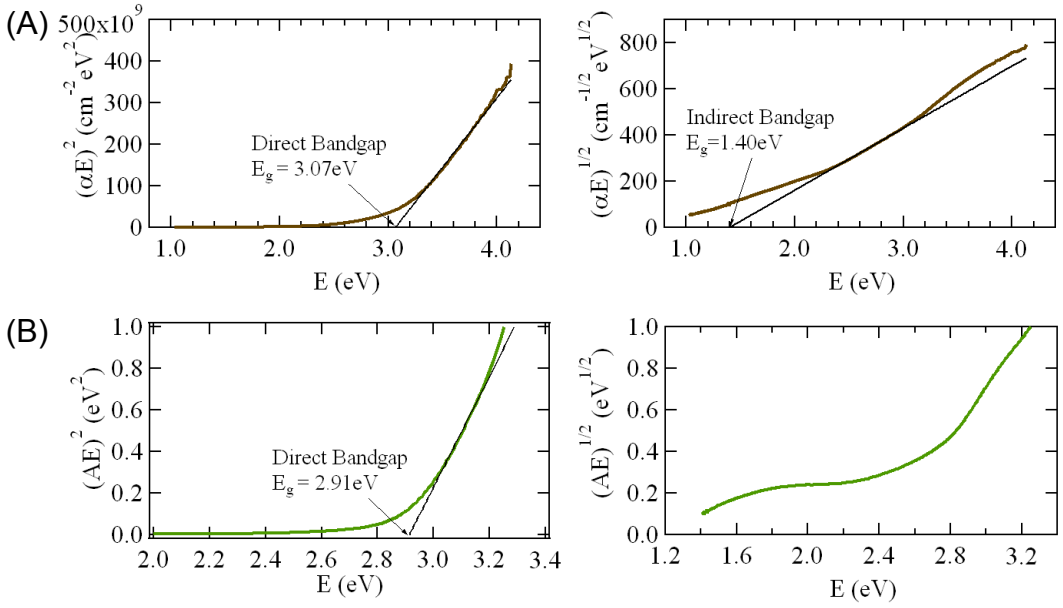

Figure 7.8 Tauc plot direct and indirect band-gap fits for (a) CuO (b) Cu_2O.

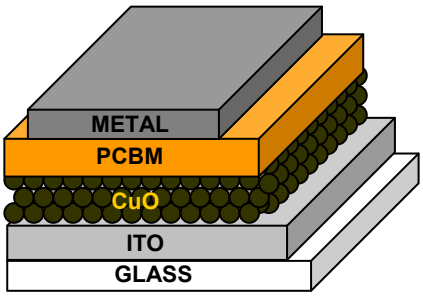

Figure 7.9 Schematic of the CuO / PCBM bilayer solar cell.

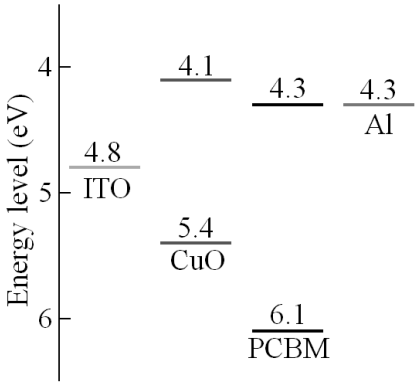

Figure 7.10 Device energy level diagram.

As a proof of concept of the light-harvesting applications of the copper oxide NCs, a bilayer solar cell comprising of CuO and PCBM was fabricated. A single layer of CuO is unsuitable as the active layer, since the NC film contains cracks and pinholes and will result in a short-circuited device. This is similar to what has been reported about PbSe NC films, which require multiple iterations of NC deposition and cross-linking to fill up the cracks.[81, 95] PCBM is chosen since it is the acceptor of choice in solution-processable polymer solar cells (see Chapter 1 and **Table 1.1**), and its good film forming property allows it to cover up cracks in the CuO film. The literature value energy levels of the conduction and valence bands of CuO[168] and the lowest unoccupied molecular orbital (LUMO) and highest occupied molecular orbital

(HOMO) of PCBM[48] are such that CuO and PCBM form a type II semiconductor heterojunction, hence they are suitable as a donor and acceptor pair. **Figure 7.9** shows a schematic of the device stack with indium tin oxide (ITO) forming the anode and CsF/Al as the cathode, while the literature values for the semiconductor energy levels are plotted in **Figure 7.10**.[48, 168, 200] Assignment of bulk CuO energy levels is supported by the small difference in NC optical band-gap relative to literature (bulk) values.[168]

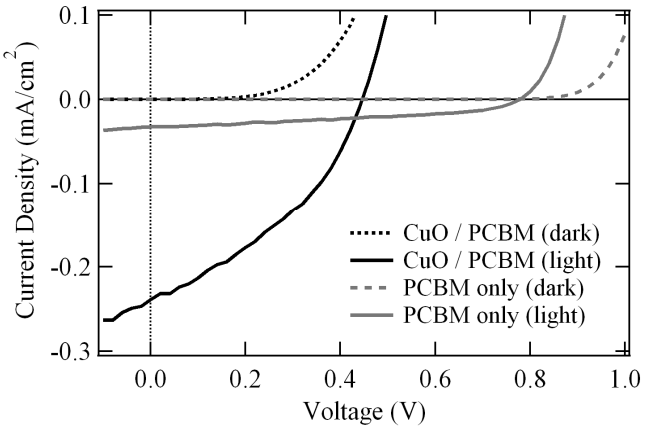

Figure 7.11 Current-voltage curves in the dark and light (AM 1.5 100 mW/cm^2) of a CuO (40 nm) / PCBM bilayer cell and the control PCBM only cell.

Figure 7.11 shows the device current density voltage (J-V) curves both in the dark and light (under AM 1.5 100 mW/cm^2 illumination) of the bilayer cell with a ~40 nm thick CuO layer. It achieved a V_{OC} of 0.44 V, J_{SC} of 0.24 mA/cm^2, fill factor (FF) of 0.38 and a power conversion efficiency (PCE) of 0.040 %. As a control, a PCBM only cell (without CuO) was fabricated and tested (also shown in **Figure 7.11**). It shows a much lower J_{SC} of 0.03 mA/cm^2 and PCE of 0.011 %, although it gave a higher V_{OC} of 0.78 V and slightly higher FF of 0.41. Meanwhile, a bi-layer cell with a thicker CuO (~70 nm) layer is characterized by poorer J_{SC} (0.15 mA cm^{-2}), FF (0.35), and PCE (0.024 %) compared to the cell with thinner CuO (refer to **Table 7.1** for a

summary of device results**)**. These results suggest that efficient charge collection is only taking place in the thin CuO layer near the interface, and additional CuO layer thickness does not contribute to the photocurrent while possibly adding to series resistance and recombination as indicated by the poorer FF. A route to improving device performance may be to use semiconductor nanowires (such as n-type ZnO) as the acceptor material, and the CuO NCs are then infiltrated into the gaps of the NWs. Such a device architecture has the advantage of separating the light absorption and charge collection pathways, so that both processes can be efficient.[201]

Table 7.1 Summary of solar cell device results.

Active material	V_{OC} [V]	J_{SC} [mA/cm^2]	FF	PCE [%]
CuO (40 nm) / PCBM	0.44	0.24	0.38	0.040
CuO (70 nm) / PCBM	0.46	0.15	0.35	0.024
PCBM	0.78	0.03	0.41	0.011

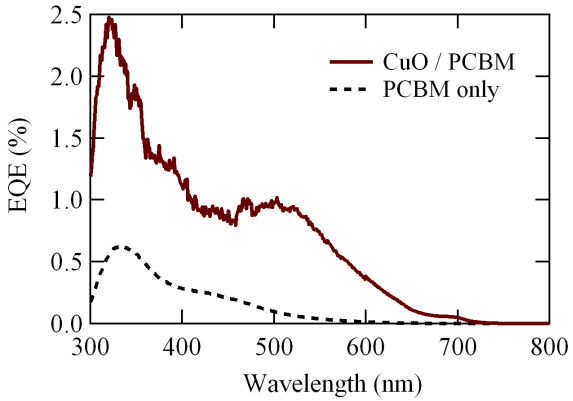

Figure 7.12 Comparison of EQE spectra of CuO (40 nm) / PCBM bilayer cell and PCBM-only cell.

External quantum efficiency (EQE) spectra of the devices were also taken and plotted in **Figure 7.12**. Not surprisingly, the shape of the EQE of the PCBM only cell follows that of the PCBM absorption. It is clear that the bilayer cell shows a superior

EQE to the PCBM only cell, and the improved EQE at higher wavelengths beyond 500 nm can be attributed to the contribution from the CuO by taking into account the absorption spectra of both materials (**Figure 7.6**).

Conclusion

A synthesis of CuO and Cu_2O NCs by a facile alcothermal route is reported. The CuO NCs are dispersible in a chloroform / methanol mixture while the Cu_2O NCs are water dispersible, thus enabling the processing of these materials by solution. A bilayer CuO and PCBM solar cell achieved a power conversion efficiency of 0.04 %, indicating the potential of these materials for light-harvesting applications.

REFERENCES

[1] N. S. Lewis, D. G. Nocera, *Proc. Natl. Acad. Sci. U. S. A.,* **2006***, 103*, 15729.

[2] J. Sheffield, S. Obenschain, D. Conover, R. Bajura, D. Greene, M. Brown, E. Boes, K. McCarthy, D. Christian, S. Dean, G. Kulcinski, P. L. Denholm, *J. Fusion Energy,* **2004***, 23*, 63.

[3] R. K. Pachauri, A. Reisinger, *Climate Change 2007: Synthesis Report*, Intergovernmental Panel on Climate Change, Geneva, Switzerland **2007**.

[4] N. S. Lewis, *MRS Bull,* **2007***, 32*, 808.

[5] D. Ginley, M. A. Green, R. Collins, *MRS Bull,* **2008***, 33*, 355.

[6] C. J. Brabec, J. R. Durrant, *MRS Bull,* **2008***, 33*, 670.

[7] S. E. Shaheen, R. Radspinner, N. Peyghambarian, G. E. Jabbour, *Appl. Phys. Lett.,* **2001***, 79*, 2996.

[8] C. N. Hoth, S. A. Choulis, P. Schilinsky, C. J. Brabec, *Adv Mater,* **2007***, 19*, 3973.

[9] D. Vak, S. Kim, J. Jo, S. Oh, S. Na, J. Kim, D. Kim, *Appl. Phys. Lett.,* **2007***, 91*, 081102.

[10] Y. F. Lim, S. Lee, D. J. Herman, M. T. Lloyd, J. E. Anthony, G. G. Malliaras, *Appl. Phys. Lett.,* **2008***, 93*, 193301.

[11] J. Tang, E. H. Sargent, *Adv. Mater.,* **2010***, 22*, 12.

[12] G. Malliaras, R. Friend, *Phys Today,* **2005***, 58*, 53.

[13] R. Hoffmann, C. Janiak, C. Kollmar, *Macromolecules,* **1991***, 24*, 3725.

[14] D. J. Griffiths, *Introduction to Quantum Mechanics*, Prentice Hall, Inc., Upper Saddle River, New Jersey, USA **1995**.

[15] C. W. Tang, *Appl. Phys. Lett.,* **1986***, 48*, 183.

[16] G. A. Chamberlain, *Solar Cells,* **1983***, 8*, 47.

[17] G. Dennler, N. S. Sariciftci, *Proc IEEE,* **2005***, 93*, 1429.

[18] P. Peumans, A. Yakimov, S. R. Forrest, *J. Appl. Phys.,* **2003***, 93*, 3693.

[19] N. S. Sariciftci, L. Smilowitz, A. J. Heeger, F. Wudl, *Science,* **1992***, 258*, 1474.

[20] J. Xue, S. Uchida, B. P. Rand, S. R. Forrest, *Appl. Phys. Lett.,* **2004***, 84*, 3013.

[21] S. Yoo, B. Domercq, B. Kippelen, *Appl. Phys. Lett.,* **2004***, 85*, 5427.

[22] S. Wang, E. I. Mayo, M. D. Perez, L. Griffe, G. Wei, P. I. Djurovich, S. R. Forrest, M. E. Thompson, *Appl. Phys. Lett.,* **2009***, 94*, 233304.

[23] R. Fitzner, E. Reinold, A. Mishra, E. Mena-Osteritz, H. Ziehlke, C. Korner, K. Leo, M. Riede, M. Weil, O. Tsaryova, A. Weiß, C. Uhrich, M. Pfeiffer, P. Bauerle, *Adv. Funct. Mater.,* **2011***, 21*, 10.1002/adfm.201001639.

[24] J. C. Hummelen, B. W. Knight, F. LePeq, F. Wudl, J. Yao, C. L. Wilkins, *J. Org. Chem.,* **1995***, 60*, 532.

[25] G. Yu, J. Gao, J. C. Hummelen, F. Wudl, A. J. Heeger, *Science,* **1995***, 270*, 1789.

[26] S. E. Shaheen, C. J. Brabec, N. S. Sariciftci, F. Padinger, T. Fromherz, J. C. Hummelen, *Appl. Phys. Lett.,* **2001***, 78*, 841.

[27] F. Padinger, R. S. Rittberger, N. S. Sariciftci, *Adv. Funct. Mater.,* **2003***, 13*, 85.

[28] H. Sirringhaus, P. J. Brown, R. H. Friend, M. M. Nielsen, K. Bechgaard, B. M. W. Langeveld-Voss, A. J. H. Spiering, R. A. J. Janssen, E. W. Meijer, P. Herwig, D. M. de Leeuw, *Nature,* **1999***, 401*, 685.

[29] X. Yang, J. Loos, S. C. Veenstra, W. J. H. Verhees, M. M. Wienk, J. M. Kroon, M. A. J. Michels, R. A. J. Janssen, *Nano Lett.,* **2005***, 5*, 579.

[30] G. Li, V. Shrotriya, J. Huang, Y. Yao, T. Moriarty, K. Emery, Y. Yang, *Nat. Mater.,* **2005***, 4*, 864.

[31] M. Reyes-Reyes, K. Kim, J. Dewald, R. López-Sandoval, A. Avadhanula, S. Curran, D. L. Carroll, *Org. Lett.,* **2005***, 7*, 5749.

[32] W. Ma, C. Yang, X. Gong, K. Lee, A. J. Heeger, *Adv. Funct. Mater.,* **2005***, 15*, 1617.

[33] Y. Kim, S. Cook, S. M. Tuladhar, S. A. Choulis, J. Nelson, J. R. Durrant, D. D. C. Bradley, M. Giles, I. McCulloch, C. Ha, M. Ree, *Nat. Mater.,* **2006***, 5*, 197.

[34] J. Peet, J. Y. Kim, N. E. Coates, W. L. Ma, D. Moses, A. J. Heeger, G. C. Bazan, *Nat. Mater.,* **2007***, 6*, 497.

[35] D. Mühlbacher, M. Scharber, M. Morana, Z. Zhu, D. Waller, R. Gaudiana, C. Brabec, *Adv. Mater.,* **2006***, 18*, 2884.

[36] J. K. Lee, W. L. Ma, C. J. Brabec, J. Yuen, J. S. Moon, J. Y. Kim, K. Lee, G. C. Bazan, A. J. Heeger, *J. Am. Chem. Soc.,* **2008***, 130*, 3619.

[37] Solar Spectral Irradiance: Air Mass 1.5, http://rredc.nrel.gov/solar/spectra/am1.5/, (accessed Feb 17, 2011).

[38] M. C. Scharber, D. Muhlbacher, M. Koppe, P. Denk, C. Waldauf, A. J. Heeger, C. J. Brabec, *Adv. Mater.,* **2006***, 18*, 789.

[39] M. F. Lo, T. W. Ng, T. Z. Liu, V. A. L. Roy, S. L. Lai, M. K. Fung, C. S. Lee, S. T. Lee, *Appl. Phys. Lett.,* **2010***, 96*, 113303.

[40] H. A. M. van Mullekom, J. A. J. M. Vekemans, E. E. Havinga, E. W. Meijer, *Materials Science and Engineering: R: Reports,* **2001***, 32*, 1.

[41] Y. Liang, Z. Xu, J. Xia, S. Tsai, Y. Wu, G. Li, C. Ray, L. Yu, *Adv. Mater.,* **2010***, 22*, E135.

[42] R. Qin, W. Li, C. Li, C. Du, C. Veit, H. Schleiermacher, M. Andersson, Z. Bo, Z. Liu, O. Ingana¨s, U. Wuerfel, F. Zhang, *J. Am. Chem. Soc.,* **2009***, 131*, 14612.

[43] E. Wang, L. Wang, L. Lan, C. Luo, W. Zhuang, J. Peng, Y. Cao, *Appl. Phys. Lett.,* **2008***, 92*, 033307.

[44] Y. Zou, A. Najari, P. Berrouard, S. Beaupre, B. Reda Aich, Y. Tao, M. Leclerc, *J. Am. Chem. Soc.,* **2010***, 132*, 5330.

[45] S. H. Park, A. Roy, S. Beaupré, S. Cho, N. Coates, J. S. Moon, D. Moses, M. Leclerc, K. Lee, A. J. Heeger, *Nat. Photonics,* **2009***, 3*, 297.

[46] H. Chen, J. Hou, S. Zhang, Y. Liang, G. Yang, Y. Yang, L. Yu, Y. Wu, G. Li, *Nat. Photonics,* **2009***, 3*, 649.

[47] J. D. Kotlarski, P. W. M. Blom, *Appl. Phys. Lett.,* **2011***, 98*, 053301.

[48] J. Y. Kim, K. Lee, N. E. Coates, D. Moses, T. Q. Nguyen, M. Dante, A. J. Heeger, *Science,* **2007***, 317*, 222.

[49] S. Sista, M. Park, Z. Hong, Y. Wu, J. Hou, W. L. Kwan, G. Li, Y. Yang, *Adv. Mater.,* **2009***, 22*, 380.

[50] R. Rossetti, S. Nakahara, L. E. Brus, *J. Chem. Phys.,* **1983***, 79*, 1086.

[51] L. E. Brus, *J. Chem. Phys.,* **1984***, 80*, 4403.

[52] M. L. Steigerwald, A. P. Alivisatos, J. M. Gibson, T. D. Harris, R. Kortan, A. J. Muller, A. M. Thayer, T. M. Duncan, D. C. Douglass, L. E. Brus, *J. Am. Chem. Soc.,* **1988***, 110*, 3046.

[53] C. B. Murray, D. J. Norris, M. G. Bawendi, *J. Am. Chem. Soc.,* **1993***, 115*, 8706.

[54] S. G. Kwon, T. Hyeon, *Acc. Chem. Res.,* **2008***, 41*, 1696.

[55] F. W. Wise, *Acc. Chem. Res.,* **2000***, 33*, 773.

[56] J. J. Choi, Y. F. Lim, M. B. Santiago-Berrios, M. Oh, B. R. Hyun, L. Sun, A. C. Bartnik, A. Goedhart, G. G. Malliaras, H. D. Abruna, F. W. Wise, T. Hanrath, *Nano Lett.,* **2009***, 9*, 3749.

[57] T. Trindade, P. O'Brien, N. L. Pickett, *Chem. Mater.,* **2001***, 13*, 3843.

[58] M. C. Beard, K. P. Knutsen, P. Yu, J. M. Luther, Q. Song, W. K. Metzger, R. J. Ellingson, A. J. Nozik, *Nano Lett.,* **2007***, 7*, 2506.

[59] A. A. Guzelian, J. E. B. Katari, A. V. Kadavanich, U. Banin, K. Hamad, E. Juban, A. P. Alivisatos, R. H. Wolters, C. C. Arnold, J. R. Heath, *J. Phys. Chem.,* **1996***, 100*, 7212.

[60] X. Zhong, Y. Feng, W. Knoll, M. Han, *J. Am. Chem. Soc.,* **2003***, 125*, 13559.

[61] S. K. Haram, B. M. Quinn, A. J. Bard, *J. Am. Chem. Soc.,* **2001***, 123*, 8860.

[62] L. Li, J. Hu, W. Yang, A. P. Alivisatos, *Nano Lett.,* **2001***, 1*, 349.

[63] K. Akamatsu, T. Tsuruoka, H. Nawafune, *J. Am. Chem. Soc.,* **2005***, 127*, 1634.

[64] R. Kho, C. L. Torres-Martinez, R. K. Mehra, *J. Colloid Interface Sci.,* **2000***, 227*, 561.

[65] R. Schaller, V. Klimov, *Phys. Rev. Lett.,* **2004***, 92*, 186601.

[66] R. J. Ellingson, M. C. Beard, J. C. Johnson, P. Yu, O. I. Micic, A. J. Nozik, A. Shabaev, A. L. Efros, *Nano Lett.,* **2005***, 5*, 865.

[67] R. D. Schaller, M. A. Petruska, V. I. Klimov, *Appl. Phys. Lett.,* **2005***, 87*, 253102.

[68] R. D. Schaller, M. Sykora, J. M. Pietryga, V. I. Klimov, *Nano Lett.,* **2006***, 6*, 424.

[69] V. I. Klimov, *Appl. Phys. Lett.,* **2006***, 89*, 123118.

[70] G. Nair, M. Bawendi, *Phys. Rev. B,* **2007***, 76*, 081304(R).

[71] M. T. Trinh, A. J. Houtepen, J. M. Schins, T. Hanrath, J. Piris, W. Knulst, A. P. L. M. Goossens, L. D. A. Siebbeles, *Nano Lett.,* **2008***, 8*, 1713.

[72] M. Ji, S. Park, S. T. Connor, T. Mokari, Y. Cui, K. J. Gaffney, *Nano Lett.,* **2009***, 9*, 1217.

[73] V. Sukhovatkin, S. Hinds, L. Brzozowski, E. H. Sargent, *Science,* **2009***, 324*, 1542.

[74] J. B. Sambur, T. Novet, B. A. Parkinson, *Science,* **2010***, 330*, 63.

[75] W. U. Huynh, J. J. Dittmer, A. P. Alivisatos, *Science,* **2002***, 295*, 2425.

[76] B. Sun, N. C. Greenham, *Phys. Chem. Chem. Phys.,* **2006***, 8*, 3557.

[77] S. Dayal, N. Kopidakis, D. C. Olson, D. S. Ginley, G. Rumbles, *Nano Lett.,* **2010***, 10*, 239.

[78] Y. Kang, N. G. Park, D. Kim, *Appl. Phys. Lett.,* **2005***, 86*, 113101.

[79] Z. Tan, T. Zhu, M. Thein, S. Gao, A. Cheng, F. Zhang, C. Zhang, H. Su, J. Wang, R. Henderson, J. Hahm, Y. Yang, J. Xu, *Appl. Phys. Lett.,* **2009***, 95*, 063510.

[80] K. M. Noone, E. Strein, N. C. Anderson, P. T. Wu, S. A. Jenekhe, D. S. Ginger, *Nano Lett.,* **2010***, 10*, 2635.

[81] J. M. Luther, M. Law, M. C. Beard, Q. Song, M. O. Reese, R. J. Ellingson, A. J. Nozik, *Nano Lett.,* **2008***, 8*, 3488.

[82] J. Tang, X. Wang, L. Brzozowski, D. A. R. Barkhouse, R. Debnath, L. Levina, E. H. Sargent, *Adv. Mater.,* **2010***, 22*, 1398.

[83] R. Debnath, J. Tang, D. A. R. Barkhouse, X. Wang, A. G. Pattantyus-Abraham, L. Brzozowski, L. Levina, E. H. Sargent, *J. Am. Chem. Soc.,* **2010***, 132*, 5952.

[84] W. Ma, J. M. Luther, H. Zheng, Y. Wu, P. Alivisatos, *Nano Lett.,* **2009***, 9*, 1699.

[85] I. Gur, N. A. Fromer, M. L. Geier, A. P. Alivisatos, *Science,* **2005***, 310*, 462.

[86] Q. Guo, S. J. Kim, M. Kar, W. N. Shafarman, R. W. Birkmire, E. A. Stach, R. Agrawal, H. W. Hillhouse, *Nano Lett.,* **2008***, 8*, 2982.

[87] Q. Guo, G. M. Ford, W. C. Yang, B. C. Walker, E. A. Stach, H. W. Hillhouse, R. Agrawal, *J. Am. Chem. Soc.,* **2010***, 132*, 17384.

[88] A. Stavrinadis, J. M. Smith, C. A. Cattley, A. G. Cook, P. S. Grant, A. A. R. Watt, *Nanotechnology,* **2010***, 21*, 185202.

[89] B. Sun, A. T. Findikoglu, M. Sykora, D. J. Werder, V. I. Klimov, *Nano Lett.,* **2009***, 9*, 1235.

[90] S. W. Tsang, H. Fu, J. Ouyang, Y. Zhang, K. Yu, J. Lu, Y. Tao, *Appl. Phys. Lett.,* **2010***, 96*, 243104.

[91] J. M. Luther, J. Gao, M. T. Lloyd, O. E. Semonin, M. C. Beard, A. J. Nozik, *Adv. Mater.,* **2010***, 22*, 3704.

[92] T. Ju, R. L. Graham, G. Zhai, Y. W. Rodriguez, A. J. Breeze, L. Yang, G. B. Alers, S. A. Carter, *Appl. Phys. Lett.,* **2010***, 97*, 043106.

[93] R. Debnath, M. T. Greiner, I. J. Kramer, A. Fischer, J. Tang, D. A. R. Barkhouse, X. Wang, L. Levina, Z. H. Lu, E. H. Sargent, *Appl. Phys. Lett.,* **2010***, 97*, 023109.

[94] A. G. Pattantyus-Abraham, I. J. Kramer, A. R. Barkhouse, X. Wang, G. Konstantatos, R. Debnath, L. Levina, I. Raabe, M. K. Nazeeruddin, M. Gratzel, E. H. Sargent, *ACS Nano,* **2010***, 4*, 3374.

[95] J. M. Luther, M. Law, Q. Song, C. L. Perkins, M. C. Beard, A. J. Nozik, *ACS Nano,* **2008***, 2*, 271.

[96] J. Nelson, *The Physics of Solar Cells*, Imperial College Press, London, UK **2003**.

[97] M. T. Lloyd, Y. F. Lim, G. G. Malliaras, *Appl. Phys. Lett.,* **2008***, 92*, 143308.

[98] Y. F. Lim, J. K. Lee, A. A. Zakhidov, J. A. DeFranco, H. H. Fong, P. G. Taylor, C. K. Ober, G. G. Malliaras, *J. Mater. Chem.,* **2009***, 19*, 5394.

[99] Y. F. Lim, Y. Shu, S. R. Parkin, J. E. Anthony, G. G. Malliaras, *J. Mater. Chem.,* **2009***, 19*, 3049.

[100] Y. Shu, Y. F. Lim, Z. Li, B. H. Purushothaman R., J. E. Kim, S. R. Parkin, G. G. Malliaras, J. E. Anthony, *Chem. Sci.,* **2011***, 2*, 363.

[101] E. Peeters, P. A. van Hal, J. Knol, C. J. Brabec, N. S. Sariciftci, J. C. Hummelen, R. A. J. Janssen, *J. Phys. Chem. B,* **2000***, 104*, 10174.

[102] P. A. van Hal, R. A. J. Janssen, G. Lanzani, G. Cerullo, M. Zavelani-Rossi, S. De Silvestri, *Chem. Phys. Lett.,* **2001***, 345*, 33.

[103] P. A. van Hal, R. A. J. Janssen, G. Lanzani, G. Cerullo, M. Zavelani-Rossi, S. De Silvestri, *Phys. Rev. B,* **2001***, 64*, 075206.

[104] P. A. van Hal, S. C. J. Meskers, R. A. J. Janssen, *Appl. Phys. A,* **2004***, 79*, 41.

[105] Y. X. Liu, M. A. Summers, S. R. Scully, M. D. McGehee, *J. Appl. Phys.,* **2006***, 99*, 093521.

[106] Y. Liu, M. A. Summers, C. Edder, J. M. J. Frechet, M. D. McGehee, *Adv. Mater.,* **2005***, 17*, 2960.

[107] R. S. Deshpande, V. Bulovic, S. R. Forrest, *Appl. Phys. Lett.,* **1999***, 75*, 888.

[108] D. F. O'Brien, M. A. Baldo, M. E. Thompson, S. R. Forrest, *Appl. Phys. Lett.,* **1999***, 74*, 442.

[109] P. Peumans, S. R. Forrest, *Appl. Phys. Lett.,* **2001***, 79*, 126.

[110] S. Coe, W. K. Woo, M. Bawendi, V. Bulovic, *Nature,* **2002***, 420*, 800.

[111] A. C. Mayer, M. T. Lloyd, D. J. Herman, T. G. Kasen, G. G. Malliaras, *Appl. Phys. Lett.,* **2004***, 85*, 6272.

[112] D. C. Coffey, A. J. Ferguson, N. Kopidakis, G. Rumbles, *ACS Nano,* **2010***, 4*, 5437.

[113] P. Schilinsky, C. Waldauf, C. J. Brabec, *Adv. Funct. Mater.,* **2006***, 16*, 1669.

[114] R. Green, A. Morfa, A. J. Ferguson, N. Kopidakis, G. Rumbles, S. E. Shaheen, *Appl. Phys. Lett.,* **2008***, 92*, 033301.

[115] E. Ahlswede, W. Muhleisen, M. W. b. M. Wahi, J. Hanisch, M. Powalla, *Appl. Phys. Lett.,* **2008***, 92*, 143307.

[116] K. Fehse, K. Walzer, K. Leo, W. Lovenich, A. Elschner, *Adv. Mater.,* **2007***, 19*, 441.

[117] J. Huang, G. Li, Y. Yang, *Adv. Mater.,* **2008***, 20*, 415.

[118] G. Li, C. W. Chu, V. Shrotriya, Y. Yang, *Appl. Phys. Lett.,* **2006***, 88*, 253503.

[119] H. H. Liao, L. M. Chen, Z. Xu, G. Li, Y. Yang, *Appl. Phys. Lett.,* **2008***, 92*, 173303.

[120] K. Kim, J. Liu, M. A. G. Namboothiry, D. L. Carroll, *Appl. Phys. Lett.,* **2007***, 90*, 163511.

[121] J. B. Lee, Z. Chen, M. G. Allen, *J. Microelectromechanical Syst.,* **1995***, 4*, 102.

[122] T. Sakakibara, H. Izua, T. Shibata, H. Tarui, K. Shibata, S. Kiyama, N. Kawahara, *Sensors and Actuators A,* **2002***, 95*, 208.

[123] M. Niggemann, W. Graf, A. Gombert, *Adv. Mater.,* **2008***, 20*, 4055.

[124] C. D. Dimitrakopoulos, P. R. L. Malenfant, *Adv. Mater.,* **2002***, 14*, 99.

[125] J. Lewis, J. Zhang, X. Jiang, *J. Renewable Sustainable Energy,* **2009***, 1*, 013101.

[126] J. K. Lee, M. Chatzichristidi, A. A. Zakhidov, P. G. Taylor, J. A. DeFranco, H. S. Hwang, H. H. Fong, A. B. Holmes, G. G. Malliaras, C. K. Ober, *J. Am. Chem. Soc.,* **2008***, 130*, 11564.

[127] A. A. Zakhidov, J. K. Lee, H. H. Fong, J. A. DeFranco, M. Chatzichristidi, P. G. Taylor, C. K. Ober, G. G. Malliaras, *Adv. Mater.,* **2008***, 20*, 3481.

[128] I. T. Horvath, J. Rabai, *Science,* **1994***, 266*, 72.

[129] J. K. Lee, H. H. Fong, A. A. Zakhidov, G. E. McCluskey, P. G. Taylor, M. Santiago-Berrios, H. D. Abruna, A. B. Holmes, G. G. Malliaras, C. K. Ober, *Macromolecules,* **2010***, 43*, 1195.

[130] H. H. Fong, J. K. Lee, Y. F. Lim, A. A. Zakhidov, W. W. H. Wong, A. B. Holmes, C. K. Ober, G. G. Malliaras, *Adv. Mater.,* **2011***, 23*, 735.

[131] J. Huang, R. Xia, Y. Kim, X. Wang, J. Dane, O. Hofmann, A. Mosley, A. J. de Mello, J. C. de Mello, D. D. C. Bradley, *J. Mater. Chem.,* **2007***, 17*, 1043.

[132] Y. Liang, D. Feng, Y. Wu, S. Tsai, G. Li, C. Ray, L. Yu, *J. Am. Chem. Soc.,* **2009***, 131*, 7792.

[133] J. J. Dittmer, E. A. Marseglia, R. H. Friend, *Adv Mater,* **2000***, 12*, 1270.

[134] R. Koeppe, N. S. Sariciftci, *Photochem. Photobiol. Sci.,* **2006***, 5*, 1122.

[135] W. Kratschmer, L. D. Lamb, K. Fostiropoulos, D. R. Huffman, *Nature,* **1990***, 347*, 354.

[136] L. T. Scott, M. M. Boorum, B. J. McMahon, S. Hagen, J. Mack, J. Blank, H. Wegner, A. de Meijere, *Science,* **2002***, 295*, 1500.

[137] Y. Liu, Y. W. Yang, Y. Chen, *Chem. Comm.,* **2005**, 4208.

[138] T. Kietzke, H. H. Horhold, D. Neher, *Chem. Mater.,* **2005***, 17*, 6532.

[139] C. R. McNeill, A. Abrusci, J. Zaumseil, R. Wilson, M. J. McKiernan, J. H. Burroughes, J. J. M. Halls, N. C. Greenham, R. H. Friend, *Appl. Phys. Lett.,* **2007***, 90*, 193506.

[140] S. C. Veenstra, J. Loos, J. M. Kroon, *Prog. Photovolt: Res. Appl.,* **2007***, 15*, 727.

[141] A. M. Ballantyne, L. Chen, J. Dane, T. Hammant, F. M. Braun, M. Heeney, W. Duffy, I. McCulloch, D. D. C. Bradley, J. Nelson, *Adv. Funct. Mater.,* **2008***, 18*, 2373.

[142] M. M. Mandoc, B. de Boer, P. W. M. Blom, *Phys. Rev. B,* **2006***, 73*, 155205.

[143] M. M. Mandoc, F. B. Kooistra, J. C. Hummelen, B. de Boer, P. W. M. Blom, *Appl. Phys. Lett.,* **2007***, 91*, 263505.

[144] S. Rajaram, P. B. Armstrong, B. J. Kim, J. M. J. Frechet, *Chem. Mater.,* **2009***, 21*, 1775.

[145] Z. E. Ooi, T. L. Tam, R. Y. C. Shin, Z. K. Chen, T. Kietzke, A. Sellinger, M. Baumgarten, K. Mullen, J. C. deMello, *J. Mater. Chem.,* **2008***, 18*, 4619.

[146] Y. Zhou, J. Pei, Q. Dong, X. Sun, Y. Liu, W. Tian, *J. Phys. Chem. C,* **2009***, 113*, 7882.

[147] P. Sonar, G. M. Ng, T. T. Lin, A. Dodabalapur, Z. K. Chen, *J. Mater. Chem.,* **2010***, 20*, 3626.

[148] F. G. Brunetti, X. Gong, M. Tong, A. J. Heeger, F. Wudl, *Angew. Chem. Int. Ed.,* **2010***, 49*, 532.

[149] J. E. Anthony, *Angew. Chem. Int. Ed.,* **2008***, 47*, 452.

[150] Y. Sakamoto, T. Suzuki, M. Kobayashi, Y. Gao, Y. Fukai, Y. Inoue, F. Sato, S. Tokito, *J. Am. Chem. Soc.,* **2004***, 126*, 8138.

[151] B. Milián Medina, J. E. Anthony, J. Gierschner, *ChemPhysChem,* **2008***, 9*, 1519.

[152] J. Jiang, B. R. Kaafarani, D. C. Neckers, *J. Org. Chem.,* **2006***, 71*, 2155.

[153] M. Y. Kuo, H. Y. Chen, I. Chao, *Chem-Eur. J.,* **2007***, 13*, 4750.

[154] J. E. Anthony, D. L. Eaton, S. R. Parkin, *Org. Lett.,* **2002***, 4*, 15.

[155] J. Chen, S. Subramanian, S. R. Parkin, M. Siegler, K. Gallup, C. Haughn, D. C. Martin, J. E. Anthony, *J. Mater. Chem.,* **2008***, 18*, 1961.

[156] J. E. Anthony, J. S. Brooks, D. L. Eaton, S. R. Parkin, *J. Am. Chem. Soc.,* **2001***, 123*, 9482.

[157] M. T. Lloyd, A. C. Mayer, S. Subramanian, D. A. Mourey, D. J. Herman, A. V. Bapat, J. E. Anthony, G. G. Malliaras, *J. Am. Chem. Soc.,* **2007***, 129*, 9144.

[158] S. K. Park, T. N. Jackson, J. E. Anthony, D. A. Mourey, *Appl. Phys. Lett.,* **2007***, 91*, 063514.

[159] M. M. Payne, S. R. Parkin, J. E. Anthony, *J. Am. Chem. Soc.,* **2005***, 127*, 8028.

[160] S. K. Park, D. A. Mourey, S. Subramanian, J. E. Anthony, T. N. Jackson, *Appl. Phys. Lett.,* **2008***, 93*, 043301.

[161] O. D. Jurchescu, S. Subramanian, R. J. Kline, S. D. Hudson, J. E. Anthony, T. N. Jackson, D. J. Gundlach, *Chem. Mater.,* **2008***, 20*, 6733.

[162] Z. Bao, A. J. Lovinger, J. Brown, *J. Am. Chem. Soc.,* **1998***, 120*, 207.

[163] X. Gong, M. Tong, F. G. Brunetti, J. Seo, Y. Sun, D. Moses, F. Wudl, A. J. Heeger, *Adv. Mater.,* **2011**, 10.1002/adma.201003768.

[164] W. J. Potscavage, S. Yoo, B. Kippelen, *Appl. Phys. Lett.,* **2008***, 93*, 193308.

[165] P. H. Stauffer and J. W. Hendley. ‚Rare Earth Elements - Critical Resources for High Technology (USGS Fact Sheet 087-02), http://pubs.usgs.gov/fs/2002/fs087-02/, (accessed Mar 14, 2011).

[166] C. Wadia, A. P. Alivisatos, D. M. Kammen, *Environ. Sci. Technol.,* **2009***, 43*, 2072.

[167] Y. Wu, C. Wadia, W. Ma, B. Sadtler, A. P. Alivisatos, *Nano Lett.,* **2008***, 8*, 2551.

[168] F. P. Koffyberg, F. A. Benko, *J. Appl. Phys.,* **1982***, 53*, 1173.

[169] G. Nagasubramanian, A. S. Gioda, A. J. Bard, *J. Electrochem. Soc.,* **1981***, 128*, 2158.

[170] W. Shockley, H. J. Queisser, *J. Appl. Phys.,* **1961***, 32*, 510.

[171] B. P. Rai, *Solar Cells,* **1988***, 25*, 265.

[172] T. Minami, H. Tanaka, T. Shimakawa, T. Miyata, H. Sato, *Jpn. J. Appl. Phys.,* **2004***, 43*, L917.

[173] T. Minami, T. Miyata, K. Ihara, Y. Minamino, S. Tuskada, *Thin Solid Films,* **2006***, 494*, 47.

[174] A. Mittiga, E. Salza, F. Sarto, M. Tucci, R. Vasanthi, *Appl. Phys. Lett.,* **2006***, 88*, 163502.

[175] K. H. Yoon, W. J. Choi, D. H. Kang, *Thin Solid Films,* **2000***, 372*, 250.

[176] Y. S. Chaudhary, A. Agrawal, R. Shrivastav, V. R. Satsangi, S. Dass, *Int J. Hydrogen Energy,* **2004***, 29*, 131.

[177] S. Anandan, X. Wen, S. Yang, *Mater. Chem. Phys.,* **2005***, 93*, 35.

[178] C. H. Kuo, M. H. Huang, *Nano Today,* **2010***, 5*, 106.

[179] M. Cao, C. Hu, Y. Wang, Y. Guo, C. Cuo, E. Wang, *Chem. Commun.,* **2003**, 1884.

[180] W. Wang, Z. Liu, Y. Liu, C. Xu, C. Zheng, G. Wang, *Appl. Phys. A,* **2003***, 76*, 417.

[181] Y. Chang, H. C. Zeng, *Cryst. Growth Des.,* **2004***, 4*, 397.

[182] J. Zhu, H. Chen, H. Liu, X. Yang, L. Lu, X. Wang, *Mater. Sci. Eng. , A,* **2004***, 384*, 172.

[183] Y. Yu, F. P. Du, J. C. Yu, Y. Y. Zhuang, P. K. Wong, *J. Solid State Chem.,* **2004***, 177*, 4640.

[184] H. Fan, L. Yang, W. Hua, X. Wu, Z. Wu, S. Xie, B. Zou, *Nanotechnology,* **2004***, 15*, 37.

[185] C. Lu, L. Qi, J. Yang, X. Wang, D. Zhang, J. Xie, J. Ma, *Adv. Mater.,* **2005***, 17*, 2562.

[186] P. He, X. Shen, H. Gao, *J. Colloid Interface Sci.,* **2005***, 284*, 510.

[187] J. Zhang, J. Liu, Q. Peng, X. Wang, Y. Li, *Chem. Mater.,* **2006***, 18*, 867.

[188] J. Y. Ho, M. H. Huang, *J. Phys. Chem. C,* **2009***, 113*, 14159.

[189] K. X. Yao, X. M. Yin, T. H. Wang, H. C. Zeng, *J. Am. Chem. Soc.,* **2010***, 132*, 6131.

[190] M. Yin, C. K. Wu, Y. Lou, C. Burda, J. T. Koberstein, Y. Zhu, S. O'Brien, *J. Am. Chem. Soc.,* **2005***, 127*, 9506.

[191] T. Kida, T. Oka, M. Nagano, *J. Am. Ceram. Soc.,* **2007***, 90*, 107.

[192] B. D. Yuhas, P. Yang, *J. Am. Chem. Soc.,* **2009***, 131*, 3756.

[193] L. Hung, C. K. Tsung, W. Huang, P. Yang, *Adv. Mater.,* **2010***, 22*, 1910.

[194] W. J. E. Beek, M. M. Wienk, M. Kemerink, X. Yang, R. A. J. Janssen, *J. Phys. Chem. B,* **2005***, 109*, 9505.

[195] E. A. Meulenkamp, *J. Phys. Chem. B,* **1998***, 102*, 5566.

[196] M. S. Tokumoto, S. H. Pulcinelli, C. V. Santilli, V. Briois, *J. Phys. Chem. B,* **2003***, 107*, 568.

[197] B. D. Cullity, S. R. Stock, *Elements of X-Ray Diffraction*, 3rd edn., Prentice Hall, Upper Saddle River, NJ, USA **2001**.

[198] R. M. Silverstein, F. X. Webster, *Spectrometric Identification of Organic Compounds*, John Wiley & Sons Inc., New York, NY, USA **1998**.

[199] O. Stenzel, *The Physics of Thin Film Optical Spectra*, Springer-Verlag, Berlin, Germany **2005**.

[200] K. Sugiyama, H. Ishii, Y. Ouchi, *J. Appl. Phys.,* **2000***, 87*, 295.

[201] K. S. Leschkies, A. G. Jacobs, D. J. Norris, E. S. Aydil, *Appl. Phys. Lett.,* **2009***, 95*, 193103.